الجمهورية الجزائرية الديمقراطية الشعبية
République Algérienne Démocratique et Populaire
وزارة التعليم العالي و البحث العلمي
Ministère de l'enseignement supérieur et de la recherche scientifique

Université Mohamed Khider – Biskra

Faculté des Sciences et de la technologie

Département :Genie Electrique

Ref :………………

جامعة محمد خيضر بسكرة
كلية العلوم و التكنولوجيا
قسم: الهندسة الكهربائية
المرجع:..........

Thèse présentée en vue de l'obtention
Du diplôme de

Doctorat LMD en : Génie Electrique

Spécialité (Option) : Machines Electriques

Contrôle d'un moteur à réluctance variable destiné aux énergies renouvelables

Présentée par :

Kassimi Youghourta

Soutenue publiquement le ………………

Devant le jury composé de :

Dr. Saadi Ramzi	**Professeur**	**Président**	**Université de Biskra**
Dr. Arif Ali	**Professeur**	**Rapporteur**	**Université de Biskra**
Dr. Guettaf Abderrazak	**Professeur**	**Co- Rapporteur**	**Université de Biskra**
Dr. Hammoudi Yacine	**Professeur**	**Examinateur**	**Université de Biskra**
Dr. Zellouma Laid	**Professeur**	**Examinateur**	**Université de El Oued**

ACKNOWLEDGEMENT

I am sincerely grateful for the opportunity to express my heartfelt appreciation to those who have played significant roles in the completion of this thesis:

Firstly, I extend my deepest gratitude to Mr. **ARIF ALI**, esteemed professor at the University of Biskra and thesis rapporteur. His guidance, trust, and unwavering interest have been invaluable throughout this journey.

I am equally thankful to Mr. **GUETTAF ABDERRAZAK**, professor at the University of Biskra, who served as the co-rapporteur for this thesis. His direction and continuous support have been instrumental in its realization.

Special thanks are also due to Mr **BEHRI MBAREK**, professor at the University of Biskra and president of the scientific committee of the Department of Electrical Engineering. I am grateful for his guidance and the confidence he placed in me throughout this endeavor.

I am deeply honored to acknowledge Mr **SAADI RAMZI**, lecturer at the University of Biskra, for graciously chairing the jury during my defense.

My sincere appreciation goes to Mr. **HAMMOUDI YACINE**, Professor at the University of Biskra, for his willingness to examine this work.

Furthermore, I express my gratitude to Mr. **ZELLOUMA LAID**, Professor at the University of El Oued, for agreeing to participate in the examination jury.

Lastly, I would like to extend my thanks to all individuals, whether directly or indirectly involved, who contributed to the development and completion of this work. Your support has been invaluable, and I am truly grateful for it.

DEDICATE

Dedicated to the unwavering love and support of my Father and my mother,

To the cherished bond with my sisters, my brothers, and my Loved ones,

To the mentors and teachers who have enriched my life with their wisdom,

And to the dear friends with whom I have created lasting memories.

KASSIMI YOUGHOURTA

Notations and symboles

s, r	Stator and rotor indices, respectively
N_r	Number of rotor poles
N_s	Number of stator poles
θ_O	Switching angle [°]
θ_{off}	Switching angle [°]
θ_e	Electric angle [°]
θ_m	Mechanical angle [°]
R	Resistance [Ω]
i	Instantaneous current [A]
V_s	Source voltage [V]
I	Current per phase [A]
ψ	Flux [Wb]
ω	Angular velocity [rd/s]
L	inductance [H]
α_p	Conduction period (not polar)
μ	Magnetic permeability
f	Frequency [Hz]
p	Power [w]
Ω	Rotor rotation pulsation [rd/s]

Notations and symboles

C_e	Electromagnetic torque [Nm]
C_r	Mechanical torque [Nm]
B	Magnetic induction [T]
W	Energy
$\overline{W}$	Co-energy
δ	Angle of movement [°]
F	Coefficient of viscous friction [Nm.s/rd]
J	Drive moment of inertia [$Kg.m^2$]
L_s	Stator phase inductance
L_r	Rotor phase inductance
L_m	Mutual inductance between the stator and rotor
SRM	Switched reluctance motor
CCC	Current control
DTC	Direct Torque Control
DEC	Direct Energy Control
DFC	Direct Force Control
DEFC	Direct Energy and Force Control
MPPT	maximum power point tracking
P&O	Perturb and Observe
EV	Electrical Vehicle
PV	Photovoltaic
I_{sc}	Short-circuit current (current when the terminals are shorted)
V_{oc}	Open-circuit voltage (voltage when no current is flowing)

Notations and symboles

I_{mpp}	Current at the maximum power point
V_{mpp}	Voltage at the maximum power point
P_{mpp}	Maximum power point output
DC/DC	Converter DC

✓ Other specific notations can be defined in the chapters

Summary

Chapter I: Comprehensive Overview of Proposed System Components.

Chapter II: Modeling the Switched Reluctance Motor and Photovoltaic System: An Analytical Approach.

Chapter III: Advanced Control and Simulation Strategies for Switched Reluctance Motors: Comparative Analysis and Validation of a Novel Methodology.

Chapter IV: Integrated Control and Simulation of a Switched Reluctance Motor Empowered by Photovoltaic (PV) Array for Electric Vehicle Applications.

Chapter V: Experimental Evaluation of Hysteresis Control in 6/8 Switched Reluctance Motors.

General Introduction

In the ongoing discourse surrounding contemporary technological advancements, there has been a discernible and heightened emphasis on prioritizing innovations that concurrently mitigate environmental impact and fortify energy efficiency. Within the expansive realm of research and development, a particularly salient domain capturing attention is the strategic amalgamation of Switched Reluctance Motors (SRMs) and Photovoltaic (PV) arrays. This integration emerges as a compelling and progressive solution within the overarching purview of sustainable energy systems. The bedrock of this paradigm lies in its interdisciplinary nature, meticulously crafted to synergize the strengths of disparate yet complementary fields. At its core, the integration seeks to not only fine-tune the motor control mechanisms inherent in SRMs but also to seamlessly incorporate the potent energy generated from photovoltaic sources. This amalgamation, strategically designed and executed, represents a symbiotic relationship between precision engineering and renewable energy utilization. The ensuing introduction, as a precursor to a comprehensive exploration, aspires to delineate with precision the fundamental components and the overarching objectives that define this sophisticated and forward-thinking sustainable system. The switched reluctance motor (SRM) concept traces its roots back to the 19th century when it was initially termed an "electromagnetic motor." Although fundamentally an old concept, SRM has experienced significant evolution, with its applications extending to both rotary and linear stepper motors. The transition from a step mode to a continuous mode, facilitated by power semiconductor control, was a pivotal development introduced by Nasar, French, Koch, and Lawrenson in the 1960s . During this period, the control of SRMs was constrained to semiconductor power thyristor types.

In more recent years, advancements in technology have witnessed the emergence of power transistors, GTOs, IGBTs, and MOSFETs capable of meeting the power requirements for effective SRM control. Notably, this progression has expanded the possibilities for SRM applications and enhanced their overall efficiency.

A distinctive feature of the SRM configuration is the elimination of permanent magnets, brushes, and commutators. The stator, comprised of steel sheets forming salient poles, hosts a series of coils connected independently in phase pairs spanning the stator poles. In contrast, the rotor, lacking winding, consists essentially of laminated steel, forming salient poles. This unique characteristic, denoted as "double salience" due to salient poles existing on both the rotor and stator, contributes to the SRM's simplicity and reliability. Furthermore, the absence of permanent magnets distinguishes SRMs from other motors in the industry, such as cage and direct current machines. This distinctive feature, coupled with its simplicity, positions the SRM as a viable and cost-effective option for speed control, presenting a challenge to other existing machines in the industry.

Switched Reluctance Motors (SRMs) have become increasingly prominent in various applications due to their numerous advantages. The inherent efficiency, simplicity, and adaptability of SRMs make them a compelling choice across various industries. The key advantages associated with SRMs include:

- Robustness and Reliability: SRMs are known for their robust and reliable performance, attributed to the absence of brushes and permanent magnets, minimizing wear and tear and contributing to extended operational lifespans.
- Simplicity of Design: The design of SRMs is inherently simpler than other motor types, facilitating straightforward manufacturing and maintenance processes due to fewer components.
- High Power Density: SRMs exhibit remarkable power density, delivering substantial power output relative to their size, which is advantageous in applications where space is a critical consideration.
- Adaptability to Harsh Environments: The robust construction of SRMs makes them well-suited for operation in harsh environments, suitable for a diverse range of industrial applications.
- Cost-Effectiveness: The simplicity of SRM design and the elimination of certain components contribute to cost-effectiveness in both manufacturing and maintenance, making them attractive across various industries.
- Flexibility in Control: SRMs offer a high degree of flexibility in control and operation, allowing for precise and dynamic adjustments in various operating conditions.
- Wide Speed Range: SRMs operate efficiently across a broad speed range, positioning them favourably in applications where speed control is a critical factor.

- High Torque Density: SRMs demonstrate the capability to deliver high torque even at low speeds, proving advantageous in applications that require substantial starting torque or precise torque control.
- Ease of Integration with Power Electronics: SRMs seamlessly integrate with power electronics, enabling effective control and optimizing overall performance and efficiency.
- Environmental Friendliness: The elimination of permanent magnets in SRMs contributes to their environmental friendliness, making them more ecologically sustainable compared to motors using rare-earth magnets.

In summary, the amalgamation of reliability, simplicity, adaptability, and cost-effectiveness positions SRMs as a noteworthy technology in various industrial applications, making them a compelling choice for modern electric motor applications. These advantages have led to their use in electric vehicles, aerospace applications, and industrial drives, among other fields.

The scientific community within the energy sector is actively dedicated to advancing the widespread adoption of clean energy solutions across an array of disciplines, in light of the pressing need to address environmental concerns. Solar energy, among the diverse spectrum of clean alternatives, has emerged as a focal point due to its intrinsic simplicity and ubiquitous availability. Recognized for its vast potential in generating clean and sustainable power, solar energy is increasingly acknowledged as a practical and viable energy source with transformative implications for the energy sector.

The trajectory of the energy sector is on the cusp of significant transformation, contingent upon sustained research and investment in the realm of solar power technology. Solar energy's advantages, including cost-effective fuel, minimal maintenance requirements, and the capability to be deployed in remote, off-grid locations, position it as a transformative force capable of addressing the energy needs of regions traditionally beyond the reach of conventional power sources. Photovoltaic systems, leveraging these attributes, emerge as pivotal players in the domain of alternative energy.

Despite the myriad advantages, solar energy does present challenges, notably its susceptibility to temperature fluctuations, humidity, and dust accumulation, which can impede operational efficiency. In response to these challenges, experts are diligently focused on developing cost-effective and environmentally friendly charging solutions. This effort gains added significance in the wake of the burgeoning popularity of electric vehicles (EVs), where solar energy integration holds the potential to revolutionize sustainable transportation.

The ongoing commitment to overcoming challenges and optimizing the efficiency of solar energy systems underscores the importance of holistic and interdisciplinary approaches. As the energy landscape evolves, advancements in solar power technology will undoubtedly play a pivotal role in shaping a more sustainable and resilient future. The synergy between research, innovation, and practical applications remains integral to harnessing the full potential of solar energy and steering the global energy paradigm towards a cleaner and more sustainable trajectory.

The optimization of Switched Reluctance Motors (SRMs) to unlock their full potential necessitates a meticulous focus on achieving precise control over both torque and speed. Within the field of SRM control, a diverse array of methodologies has been developed, each exhibiting its own unique set of advantages and limitations. Recent advancements in research have delved into the exploration of sophisticated SRM control techniques, elevating the understanding and performance of these motors. Current regulation strategies, for instance, have been a focal point, allowing for more accurate and responsive adjustments to the motor's behavior. Additionally, torque control strategies have been refined to enhance the precision and reliability of torque delivery, catering to diverse industrial applications. Furthermore, the investigation of vibration suppression techniques represents a crucial frontier, as it addresses operational challenges associated with mechanical vibrations, thereby optimizing the overall performance and lifespan of SRMs. The ongoing exploration of these advanced control methodologies underscores the commitment to refining SRM technology, paving the way for its broader integration into various sectors where precision, efficiency, and reliability are paramount. As research in this domain progresses, the potential for further innovations and enhancements in SRM control mechanisms continues to grow, contributing to the evolution of electric motor technologies and their applications across industries.

This investigation critically evaluates the feasibility and operational efficacy of an integrated system comprising a Photovoltaic (PV) system and a Switching Reluctance Motor (SRM), driven by a spectrum of control methodologies, including Direct Energy and Force Control (DEFC), current control, direct torque control, direct energy control, and direct force control. The comprehensive research entails an in-depth analysis of the collective performance of the integrated system, assessing the efficiency of the SRM within this framework. Furthermore, the study meticulously examines the impact of external variables such as radiation and temperature on the motor's functionality, elucidating key insights into the system's robustness under varying environmental conditions.

A pivotal aspect of the integrated system is the utilization of Maximum Power Point Tracking (MPPT) by the PV system. This strategic approach ensures that the PV system operates at its optimal efficiency, dynamically adjusting its operating point to capture the maximum available power from solar radiation. The synergistic interaction between the PV system and the SRM, underpinned by diverse control strategies, contributes to a holistic exploration of the system's capabilities and limitations.

This dissertation is meticulously structured to provide a comprehensive exploration of key aspects related to Switched Reluctance Motors (SRMs) and their integration with photovoltaic systems. The organizational framework is delineated as follows:

- Chapter I: This initial chapter elucidates the fundamental operating principles of the SRM motor, delineates various types of power supply configurations, and delves into the intricacies of the photovoltaic system. A foundational understanding of these components sets the stage for the subsequent discussions.
- Chapter II: The second chapter is dedicated to the magnetic modeling of the switched reluctance motor using the Finite Element Method (FEMM) software. Additionally, the chapter expounds upon the model of the photovoltaic system, providing a comprehensive analysis that forms the basis for subsequent simulation endeavors.
- Chapter III: Building upon the magnetic modeling discussed in Chapter II, the third chapter focuses on the simulation of SRM control. Various control methods are explored using MATLAB/SIMULINK, offering a detailed examination of their effectiveness and implications for SRM operation.
- Chapter IV: This section extends the analysis by addressing the simulation of SRM control within the context of its integration into a photovoltaic system. Furthermore, the chapter explores the application of this integrated system to electric vehicles, presenting a practical application of the theoretical constructs discussed earlier.
- Chapter V: In this chapter, we examine the test experiment of the hysteresis control method for a 6/8 switched reluctance motor (SRM). This control technique functions by continuously monitoring the output current and detecting deviations. When the output

current exceeds predefined threshold levels, a comparator promptly adjusts the control by switching it on or off. This methodology presents notable advantages, including swift transient responses due to the direct control facilitated by the comparator and the elimination of the necessity for phase compensation.

- Conclusion: The dissertation concludes with a comprehensive summary of the key findings, insights, and outcomes from the study, including the experimental validation of the hysteresis control method for a 6/8 switched reluctance motor (SRM). Furthermore, this section delineates potential avenues for future research, providing valuable perspectives for the continuation and expansion of the work.

Introduction

In this introductory chapter, we embark on a journey into a sophisticated system comprising a PV array, boost converter, half-bridge converter, and switched reluctance motor. These elements collectively represent the cutting edge of clean energy and advanced power systems. This chapter lays the foundation by providing an overview of the system's key components, setting the stage for a deeper exploration of their individual roles and synergistic contributions to sustainable energy solutions.

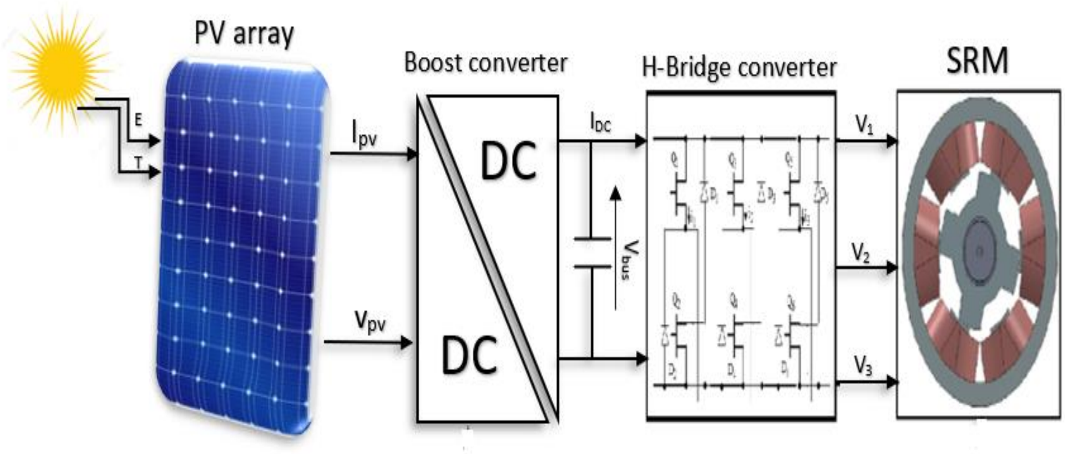

Figure I.1.Components of the Proposed System.

I.1. Switched Reluctance Motor (SRM)

A switched reluctance motor (SRM) is an electric motor that relies on reluctance torque for its operation. It falls under the category of synchronous motors, where the rotor matches the rotational speed of the magnetic field generated by the stator windings. Notably, SRMs are characterized by their straightforward construction, devoid of permanent magnets or brushes[1-4]. The stator consists of winding sets, while the rotor features salient poles that lack magnetization but possess a distinct magnetic permeability compared to the air gap between the stator and rotor[5-7]. Upon energizing the stator windings, a magnetic field arises, causing the rotor poles to align with the stator poles, thus generating reluctance torque that propels rotor rotation.[8-11]

SRMs offer several advantages over alternative motor types:

- Simplicity of Construction: SRMs boast uncomplicated designs without permanent magnets or brushes, rendering them more robust and straightforward compared to their counterparts.
- High Efficiency: These motors exhibit exceptional efficiency, often reaching levels of up to 90%.
- Wide Speed Range: SRMs can seamlessly function across a broad spectrum of speeds, spanning from very low to extremely high rates.
- Fault Tolerance: SRMs display a degree of tolerance to faults like open or shorted windings, enhancing their reliability.

Nonetheless, SRMs come with certain drawbacks:

- High Torque Ripple: The torque generated by SRMs can exhibit significant fluctuations with changing speeds, potentially leading to vibration and noise issues.
- Acoustic Noise: SRMs can produce noticeable acoustic noise, particularly at higher speeds.
- Controller Requirement: The operation of SRMs necessitates a dedicated controller, which can contribute to the overall system cost.

Despite these drawbacks, the switched reluctance motor (SRM) stands as a versatile motor used across a diverse spectrum of applications, including but not limited to: [1-3]

- Fans and Pumps: SRMs are employed to drive fans and pumps efficiently in various ventilation and fluid handling systems.
- Electric Vehicles: In the realm of electric vehicles, SRMs find purpose as power sources, contributing to improved energy utilization. [12-15]
- Wind Turbines: SRMs play a crucial role in wind turbine systems, converting wind energy into electrical power with their efficiency and adaptability.
- Machine Tools: The precision and responsiveness of SRMs make them valuable components in machine tools, enhancing machining processes. [16-18]
- Robotics: SRMs are integrated into robotics to deliver precise and reliable motion control, supporting tasks ranging from manufacturing to automation.

The SRM's popularity is on the rise, primarily attributed to its remarkable attributes such as high efficiency, extensive speed range, and fault tolerance. This motor technology holds promise for a wide array of applications, contributing to the advancement of various industries.[19-21]

I.1.1. Different types of SRM

Switched reluctance machines can be categorized into two main types based on their construction:

1. Smooth Stator Machines: In this category, the stator features a continuous, unsegmented structure.
2. Vernier Machines: The second category encompasses machines with double teeth, often referred to as "vernier" machines. In both of these categories, the rotor exhibits teeth that are identical and evenly spaced throughout its structure.

I.1.1.1. Smooth Stator Machines

In the design of this particular machinery, the stator assumes a cylindrical configuration with a revolution radius, featuring strategically carved notches to facilitate the placement of conductors. The smooth character of the stator is primarily attributed to the minimal width of these notches within the air gap, representing a negligible local irregularity within the geometric structure.

Consequently, it becomes possible to compute the current density at each individual notch, which is equivalent to the current denoted as Ni traversing the conductor accommodated in that specific location. Given the assumption of infinite permeability for the stator, the equivalent current density is therefore expressed as:

$$J = \frac{NI}{\varepsilon} \tag{I.1}$$

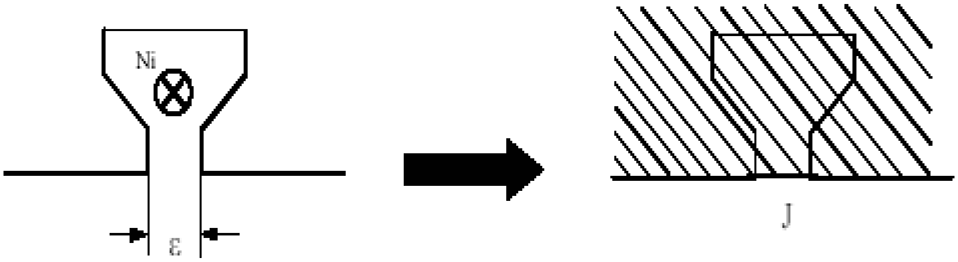

Figure I.2. Equivalent current density

I.1.1.2. Double-toothed Machinery

Double-toothed machinery refers to a class of devices in which the stator configuration deviates significantly from a smooth, uniform surface, owing to the prominent notches in relation to the rotor teeth. These notches play a pivotal role in energy conversion due to the localized irregularities stemming from the relative alignment of rotor and stator teeth. In Figure (I.3), we illustrate a specific example of a double-toothed variable reluctance machine featuring six stator poles, where each pair of diametrically opposite poles accommodates two windings connected in series, along with four rotor poles. This design stands out for its exceptional robustness and inherent simplicity, characterized by the absence of electrical conductors or magnets.

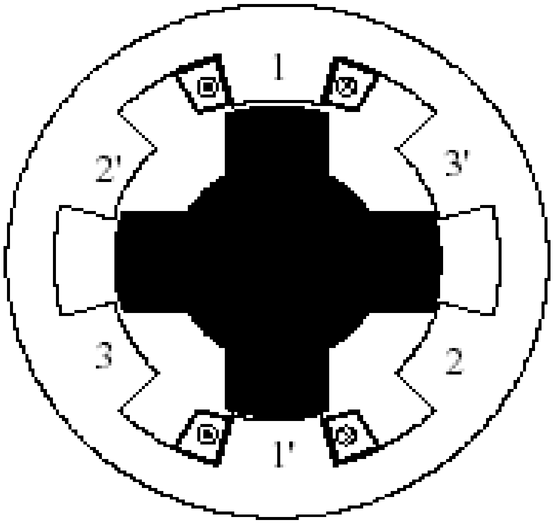

Figure I.3. Double-toothed "vernier" machine

I.1.2. Construction and Operation

The Switched Reluctance Motor (SRM) is renowned for its straightforward and minimalist construction. It features a basic design consisting of a wound stator and an unmagnetized iron rotor without windings. This rotor is crafted in a laminated iron form, shaped to create distinct salient poles. Similarly, the stator poles (Ns) also exhibit saliency and are strategically wound on poles positioned radially opposite each other. Each stator phase consists of tightly concentrated coils meticulously placed on these stator poles. Common configurations include the 6-rotor/8-stator poles 4-phase motor and the 6-rotor/4-stator poles 3-phase motor. The Switched Reluctance Machine is an electrical device that generates torque through electromagnetic forces of attraction acting on a moving rotor. This rotor moves towards a position where the reluctance, or opposition to magnetic flux, is minimal, resulting in the production of torque.

The operational principle of a Magnetic Reluctance Motor closely resembles that of an electromagnet. When one of the motor's phases is energized, it exerts an attractive force on the rotor, compelling it to pivot and align with this activated phase. The primary objective of this alignment is to optimize the magnetic flux within the motor. Consequently, two distinct positions emerge:

- The "Conjunction Position": At this juncture, the axes of the stator and rotor teeth are in precise alignment. In this configuration, the inductance of the energized phase is maximized, resulting in the highest possible magnetic flux within the motor.
- The "Opposition Position": In contrast, the rotor's tooth axis is oriented to minimize the inductance. This opposition position marks the point of minimum inductance within the motor. The inductance value varies as the rotor and stator teeth either draw nearer or move apart from each other, creating fluctuations in the magnetic field strength.

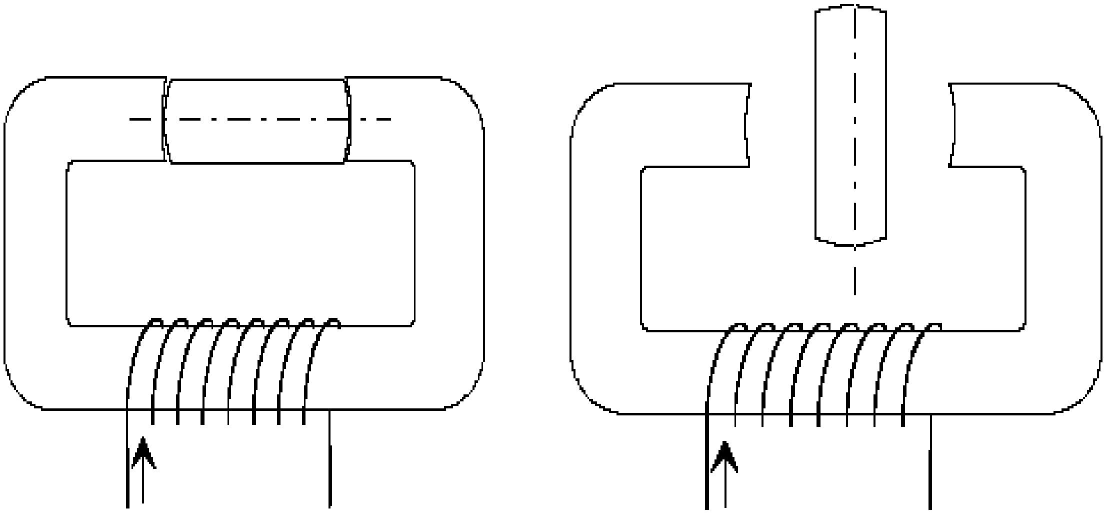

Figure I.4. Representation of a single-phase SRM.

I.1.2.1. Mathematic model

Due to the distinctive characteristics inherent to the motor, creating a mathematical model for a Switched Reluctance Motor (SRM) poses a formidable challenge, as it entails dealing with a complex system of nonlinear equations. To initiate this intricate endeavour, it is advisable to commence with a fundamental overview, progressively refining and expanding upon it to construct a simplified mathematical representation of the SRM.[14,16,22]

Disregarding any mutual coupling effects between phases, the voltage equation for phase k can be expressed as follows:

$$V_k = i_k R_k + \frac{d\psi_k(i_k,\theta)}{dt} \tag{I.2}$$

where V_k is the terminal voltage, i_k is the phase current, Ψ_k is the flux linkage in volt-seconds, θ is the rotor position and R_k is the phase resistance.

Magnetic Flux Linkages: It is imperative to establish a clear definition for the magnetic flux linkages within each phase. These linkages exhibit a nonlinear correlation with both the phase current and the position of the rotor. It can be expressed as,

$$\psi_k = \psi_k(i_k,\theta) \tag{I.3}$$

By incorporating Equation (I.3) into Equation (I.2), we derive Equation (I.4),

$$\begin{aligned} V_k &= i_k R_k + \frac{\partial\psi_k}{\partial i_k}\frac{di_k}{dt} + \frac{\partial\psi_k}{\partial\theta}\frac{d\theta}{dt} \\ &= i_k R_k + \frac{\partial\psi_k}{\partial i_k}\frac{di_k}{dt} + \omega_r\frac{\partial\psi_k}{\partial\theta} \end{aligned} \tag{I.4}$$

$$\omega_r = \frac{d\theta}{dt} \tag{I.5}$$

where ω_r is the angular velocity in rad/s. $\frac{\partial\psi_k}{\partial i_k}$ is defined as the instantaneous inductance L(θ,I) and the term is $\omega_r\frac{\partial\psi_k}{\partial\theta}$ le FCEM instant.

Torque Equation: The electromagnetic torque (T_e) produced by the motor is inherently dependent on both the rotor position and the currents flowing through each phase. This torque can be aptly described as a function of the alteration in magnetic energy concerning changes in rotor position. It is evident that a vital connection exists between the electrical and mechanical aspects through the medium of electromagnetic torque. Consequently, the central challenge revolves around formulating an accurate mathematical model for this critical parameter.

$$T_e = J\frac{d\omega_m}{dt} + B\omega_m + T_L \tag{I.6}$$

Switched Reluctance Motors (SRMs) exhibit notably pronounced nonlinear characteristics. Consequently, deriving a precise mathematical model for electromagnetic torque proves to be a formidable task. In this pursuit, certain researchers have explored the utilization of co-energy as a concept to encapsulate and express the average torque, addressing this complexity.

$$T_{av} = \frac{\Delta W_c}{\Delta \theta} \tag{I.7}$$

The variables are defined as follows: J represents the rotational inertia, B denotes the frictional coefficient, T_e signifies the electromagnetic torque, T_L stands for the load torque, and W_c corresponds to the co-energy inherent in the Switched Reluctance Motor (SRM).

Which can be expressed the co-energy as Equation (I.8),

$$W_c = \int_0^{\psi} \psi(\theta, i) di \tag{I.8}$$

I.1.2.2. Alimentation

In a switched reluctance motor, the magnetic flux is not constant but necessitates initialization from zero at each step of its operation. This procedure is orchestrated through the controlled application of the supply voltage at the Θ_0 angle and its subsequent deactivation at the Θ_{off} switching angle.[23-25]

Given the scenario where each motor phase is energized by the circuit depicted in Figure (I.5.a), with two transistors activated at time Θ_0 and deactivated at Θ_{off}, we observe in Figure (5) the waveforms of voltage, flux, current, and inductance taking on a distinctive undulating pattern at sufficiently high speeds. This particular operational mode, characterized by these waveforms, is referred to as "single-pulse" operation in the context of motor functioning.

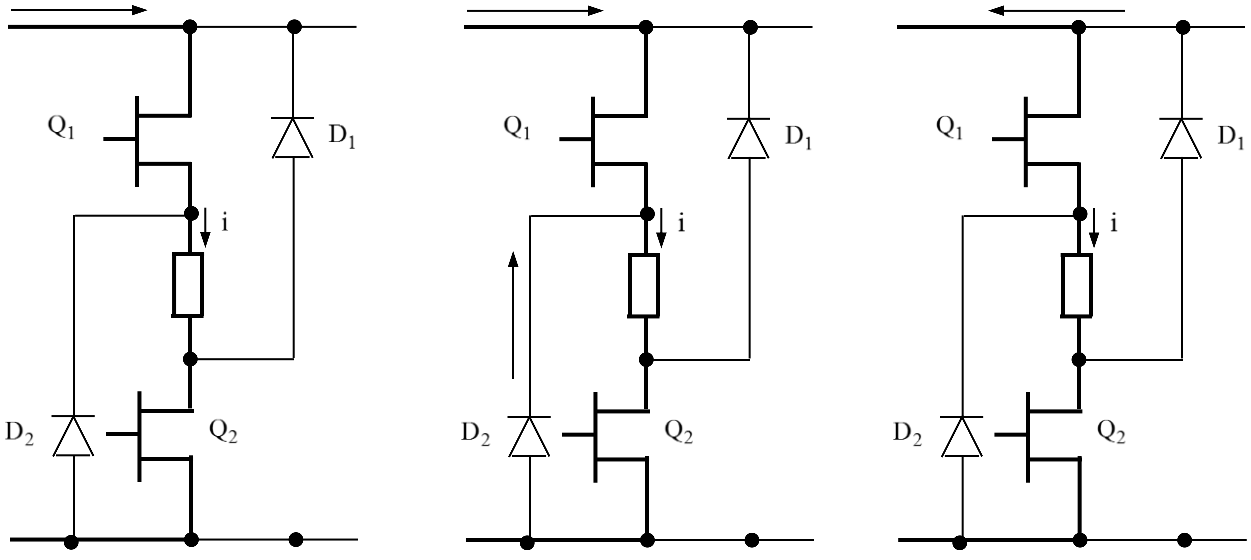

Q_1 & Q_2 on Q_2 & D_2 on D_1 & D_2 on

(a) (b) (c)

Figure I.5. Mode of conduction in one phase.

The predominant flow, as elucidated by Faraday's Law under the condition of a constant angular speed ω, can be succinctly summarized as:

$$\psi_C = \int_{\theta_0}^{\theta_{off}} (V_s - Ri)\frac{d\theta}{\omega} + \psi_0 \tag{I.9}$$

Here, ψo represents the primary flux that initially exists at angle θo, which is typically zero, V is the supply voltage, R denotes the phase resistance, and i signifies the momentary current. It is important to note that, at this juncture, any impedances and voltage reductions within the control circuit and power supply are considered negligible.[22,23]

It's worth noting that Faraday's Law characterizes the primary flow. Equation (I.9) can be reformulated as follows:

$$\omega\psi_C = (V_s - v_1).\theta_D \tag{I.10}$$

With : $\theta_D = (\theta_{off} - \theta_o)$

In this context, "V_1" signifies the voltage drop resulting from resistance during the period θd. When the internal resistance, Ri, is considerably smaller (Ri <<) in comparison to the other influencing factors, the primary flux follows a linear increase.

During motor operation, it is paramount to reduce the magnetic flux to zero prior to the separation of the rotor poles. This transition leads to a reversal in torque direction, effectively creating a braking torque. To achieve this, the voltage must be inverted at angle θc, a process typically accomplished through the use of freewheeling diodes when the transistors are in a carryover state. The precise angle at which the negative voltage propels the flux back to zero, known as the "extinction angle" θq, is further determined by the principles of Faraday's Law.

$$0 = \psi_C + \int_{\theta_{off}}^{\theta_q} (-V_s - Ri)\frac{d\theta}{\omega} \tag{I.11}$$

And this gives:

$$\omega\psi_C = (V_s + v_2).(\theta_q - \theta_{off}) \tag{I.12}$$

"V2" denotes the voltage drop attributed to resistance within the time frame ($\theta q - \theta_C$). When the internal resistance, Ri, is substantially smaller (Ri <<) than the supply voltage, Vs, the primary flux diminishes in a linear manner while maintaining a consistent velocity. The angle traversed during this process is nearly equivalent to θ_D, with both being essentially equal to the value denoted as "$\frac{\psi_C}{V_s}$" The total conduction angle is consequently equal to:

$$\theta_q - \theta_0 = \frac{2\omega\psi_C}{V_s} \tag{I.13}$$

The maximum primary flux, denoted as ψc, originates from the switching angle θoff.

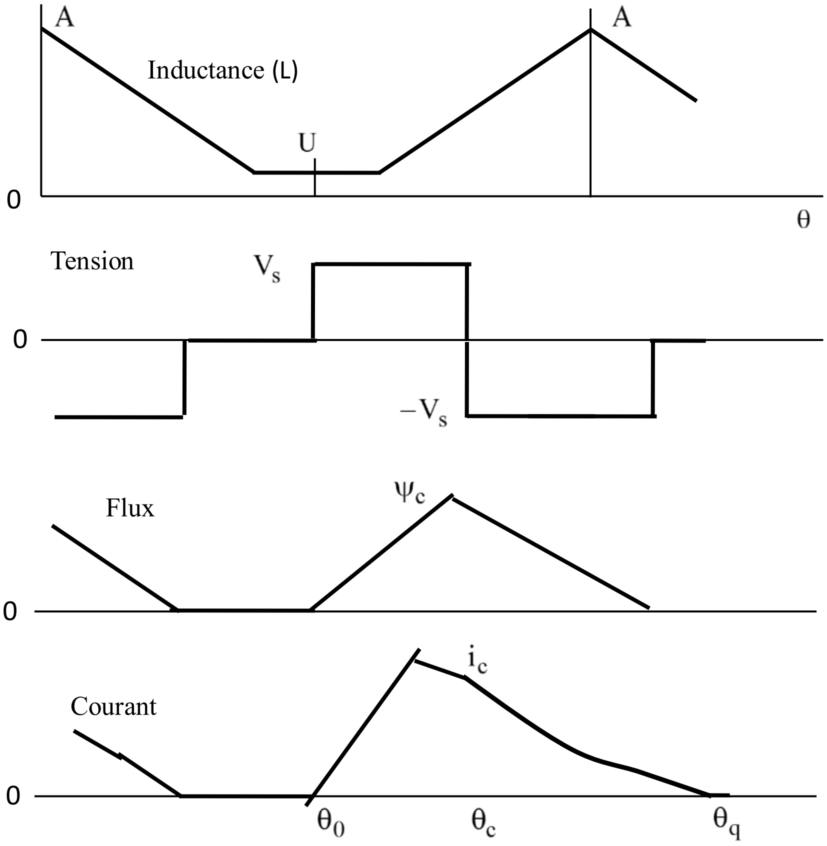

Figure I.6. Wavy shapes of single pulse

The period of the entire conduction is called the rotor pole pitch αp1:

$$\alpha_p = \frac{2\pi}{N_r} \tag{I.14}$$

This conduction is also called "continuous conduction":

$$\theta_q - \theta_o < \alpha p \tag{I.15}$$

Let's combine the two equations (I.14 and I.15), we find the maximum admissible:

$$\theta_D < \frac{\alpha_p}{1+\xi} \tag{I.16}$$

Either :

$$\xi = \frac{1}{1+\frac{V_S-v_1}{V_S+v_2}} \tag{I.17}$$

If the voltage drops V_1 and V_2 are approximately the same fractions ρ of, then equations (I.15) and (I.16) reduce to:

$$\theta_D < \alpha_p . \frac{(1+\rho)}{2} \quad \text{(I.18)}$$

I.2. Photovoltaic

I.2.1. Historic of Photovoltaic

The history of solar energy utilization has seen notable milestones. It began with early experiments, including focusing sunlight to ignite fires, but a pivotal moment arrived in 1866 when French scientist Augustin Mouchot introduced the first parabolic solar collector, which harnessed solar energy to boil water and power a steam engine. In 1839, young French scientist Alexandre Edmond Becquerel discovered the photoelectric effect, laying the foundation for photovoltaics. In 1876, Professor Willian Grylls and a student demonstrated the possibility of obtaining electricity from solid materials exposed to sunlight. In 1884, American inventor Charles Fritts improved efficiency, leading to the first rooftop PV module in New York City. Albert Einstein's theoretical explanation of the photoelectric effect in 1921 earned him a Nobel Prize. A breakthrough in the PV industry occurred in 1954 at Bell Laboratories when researchers realized impurity-doped semiconductor materials could efficiently generate electricity when exposed to light, achieving 6% efficiency. This marked the shift from selenium-based to semiconductor solar modules. Initially, solar applications powered remote sites and small loads on Earth. However, in the context of the space race, PV technology became pivotal for satellites. In 1958, the U.S. launched Vanguard I, the first solar-powered satellite, weighing just 3.5 pounds.

In the ongoing pursuit of mitigating environmental impacts, the scientific community within the energy sector is dedicating itself to the widespread adoption of clean energy solutions spanning multiple disciplines. Amid the array of clean energy options, solar energy has emerged as a prominent frontrunner, thanks to its inherent simplicity and abundant availability. The substantial potential of solar energy to provide clean and sustainable power has propelled it to the forefront of viable energy sources. The future landscape of the energy sector is poised to be significantly influenced by continuous research and investment in solar power technology. Photovoltaic systems, characterized by their low fuel costs, minimal maintenance requirements, and adaptability for installation in remote, off-grid areas, are pivotal players in the realm of alternative energy.

Nonetheless, solar energy, for all its advantages, does come with its set of challenges, including sensitivity to temperature fluctuations, humidity, and dust accumulation, all of which can impede its efficiency. In response to these challenges, experts are diligently working on developing cost-effective, environmentally friendly charging solutions, especially in light of the growing popularity of electric vehicles (EVs). One promising approach that is gaining traction is the integration of solar panels to power EVs. By harnessing the abundant energy provided by the sun, solar panels offer a reliable and economically sound source of electricity for recharging electric automobiles.[26-30]

I.2.2. .Equivalent Mathematical Model of PV Panel

The photovoltaic (PV) system is designed to convert sunlight into electrical energy with remarkable efficiency. At the core of this renewable energy generation technology lies the PV cell, which serves as the fundamental building block. These remarkable cells, their power output ranging from 1 to 2 watts depending on the materials used, are the backbone of the PV system. [31-34]Typically, these cells are clustered together to create PV panels or modules. To meet specific current and voltage demands, these PV modules are thoughtfully arranged in both series and parallel configurations, forming a cohesive PV array. For simplicity's sake, it is generally assumed that all PV modules within an array share identical characteristics.[35-39]

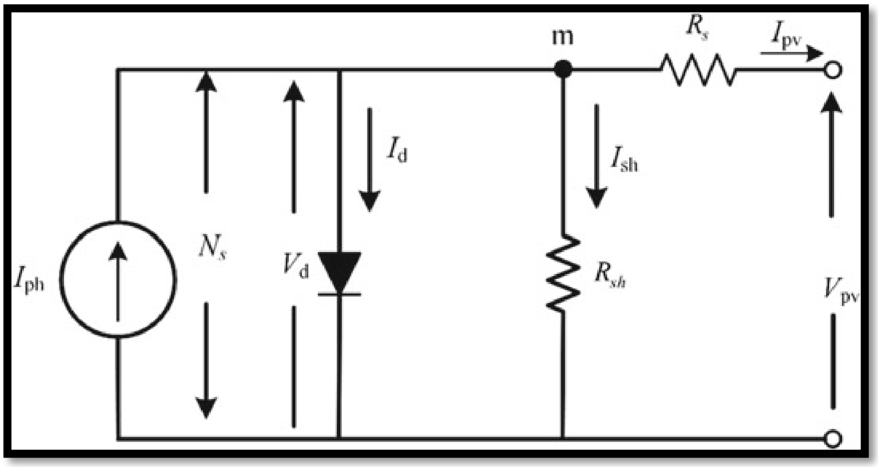

Figure I.7. Equivalent circuit representation of photovoltaic cell.

Illustrated in Figure I.7 is the equivalent circuit representation of a single-diode, five-parameter exponential model employed to describe a photovoltaic (PV) cell. This model encompasses essential components, notably a light-generated current source denoted as Iph, operating in parallel with a diode (D). Moreover, it comprehensively considers the influence of parasitic resistances, specifically the series resistance (Rs) and the shunt resistance (Rsh). By applying Kirchhoff's Current Law (KCL) at the designated node 'm,' the expression for the current generated by a solitary PV cell is succinctly articulated as follows:

$$I_{\mathrm{pv}} = I_{\mathrm{ph}} - I_{\mathrm{D}} - I_{\mathrm{sh}} \tag{I.19}$$

The magnitude of the generated current (Iph) is contingent upon the incident light's intensity upon the photovoltaic (PV) cell. Consequently, variations in temperature, which are indicative of alterations in light intensity, establish a direct proportionality with the light-generated current. This relationship can be formally articulated as follows:[32,33]

$$I_{\mathrm{ph}} = \left[I_{\mathrm{ph},n} + k_i(T - T_n)\right]S^{S}S_n \tag{I.20}$$

According to semiconductor theory, the diode current (I_{D}) can be expressed as:

$$I_{\mathrm{D}} = I_{\mathrm{o}}\left[\exp\left(\frac{qV_{\mathrm{d}}}{aKT}\right) - 1\right] \tag{I.21}$$

where

$$I_{\mathrm{o}} = \frac{I_{\mathrm{sc},n}+k_i(T-T_n)}{\exp\left(\frac{V_{\mathrm{oc},n}+k_{\mathrm{v}}(T-T_n)}{aN_{\mathrm{s}}V_{\mathrm{t}}}\right)-1} \tag{I.22}$$

Substituting (I.20) and (I.21) in (I.19) we get,

$$I_{\mathrm{pv}} = I_{\mathrm{ph}} - I_{\mathrm{o}}\left[\exp\left(\frac{V_{\mathrm{pv}}+R_{\mathrm{s}}I_{\mathrm{pv}}}{aV_{\mathrm{t}}}\right) - 1\right] - \frac{V_{\mathrm{pv}}+R_{\mathrm{s}}I_{\mathrm{pv}}}{R_{\mathrm{sh}}} \tag{I.23}$$

where

$$V_t = \frac{k \cdot T}{q} \tag{I.24}$$

The equation governing the PV module current consisting of ' N_{p} ' no. of parallel connected strings of PV cell as shown in Fig.I.7 is expressed as:

$$I_{\mathrm{PV}} = N_{\mathrm{p}}I_{\mathrm{ph}} - N_{\mathrm{p}}I_{\mathrm{o}}\left[\mathrm{e}^{\frac{q}{akT}\left(\frac{v_{\mathrm{pv}}}{N_{\mathrm{s}}}+\frac{I_{\mathrm{pv}}R_{\mathrm{s}}}{N_{\mathrm{p}}}\right)} - 1\right] - \frac{1}{R_{\mathrm{sh}}}\left[\frac{N_{\mathrm{p}}}{N_{\mathrm{s}}}V_{\mathrm{pv}} + I_{\mathrm{pv}}R_{\mathrm{s}}\right] \tag{I.25}$$

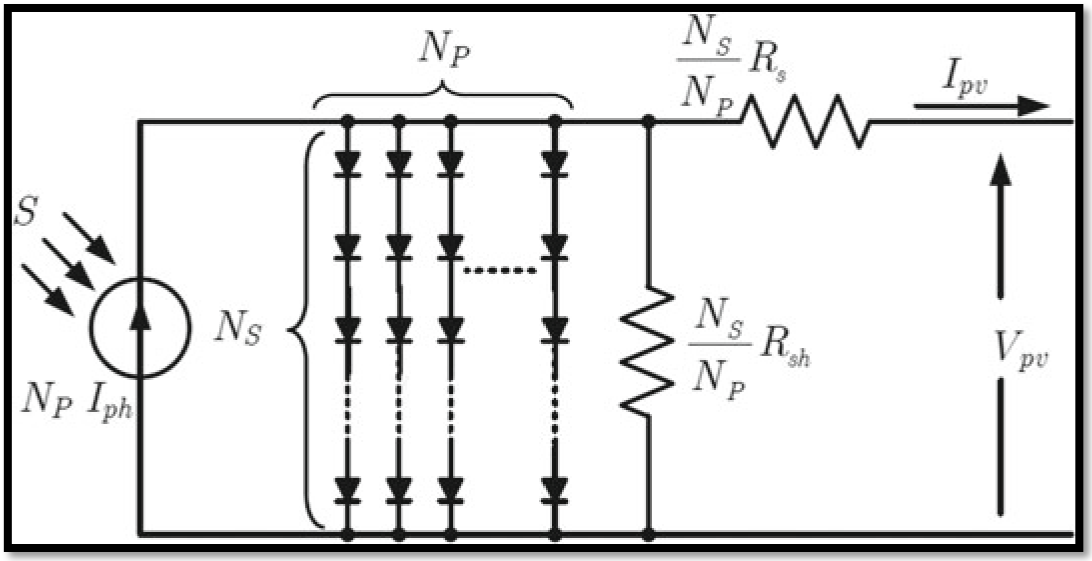

Figure I.8 Equivalent circuit representation of PV module consisting of 'Np' number of strings of

The current and operating voltage range of the photovoltaic (PV) cell are ascertained through the assessment of short-circuit and open-circuit conditions. By referencing the prior equation, we can calculate the values for short-circuit current and open-circuit voltage in the following manner:

$$V_{oc}\big|_{I_{pv}=0} = a \cdot N_s \cdot V_t \ln\left(\frac{I_{ph}}{I_o} + 1\right) \tag{I.26}$$

$$I_{sc}\big|_{V_{oc}=0} = I_{ph} / \left(1 + \frac{R_s}{R_{sh}}\right) \tag{I.27}$$

I.2.3.Boost converter

Boost converters find widespread utilization across various domains, including industrial drives, automotive applications, adaptive control systems, and battery-powered applications. Notably, they prove invaluable in scenarios necessitating the elevation of low input voltages to higher DC voltage levels. In particular, within photovoltaic (PV) applications, the boost converter assumes a critical role. It not only amplifies the PV output voltage to meet desired specifications but also orchestrates the vital task of maximum power point tracking (MPPT) control. The popularity of these converters can be attributed to their inherent attributes of simplicity and durability, requiring minimal maintenance, user-friendliness, and cost-effectiveness.

The maintenance of a constant output voltage level is achieved through precise control of the "duty cycle," which refers to the fraction of the switching period when the semiconductor switch is in the conducting state. Typically, this switch takes the form of an all-off, or off-saturated, semiconductor device, often a MOSFET transistor. In the off state, the semiconductor device experiences zero current, resulting in negligible power dissipation. Conversely, when the device is in the saturated state, the voltage drop across its terminals becomes nearly zero, leading to minimal power loss.[40-47]

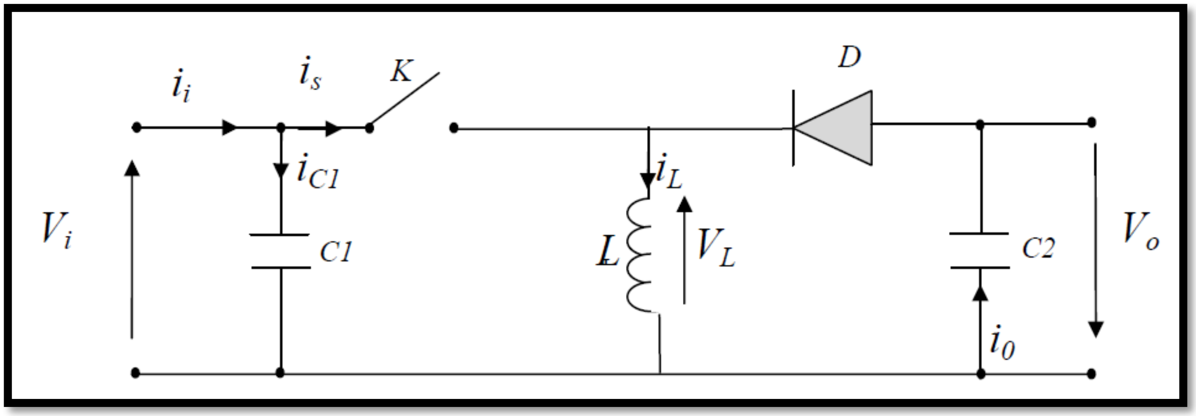

Figure I.8. boost converter.

During the operation of the chopper, the transistor undergoes cyclic switching at a consistent frequency denoted as fs. This switching action involves a closing time (Tds) and an opening time ((1-d)Ts), where:

- Ts signifies the switching period, equal to 1/fs.
- The duty cycle of the switch, denoted as 'd' and falling within the range of [0, 1], plays a pivotal role in determining the precise timing and duration of these states.

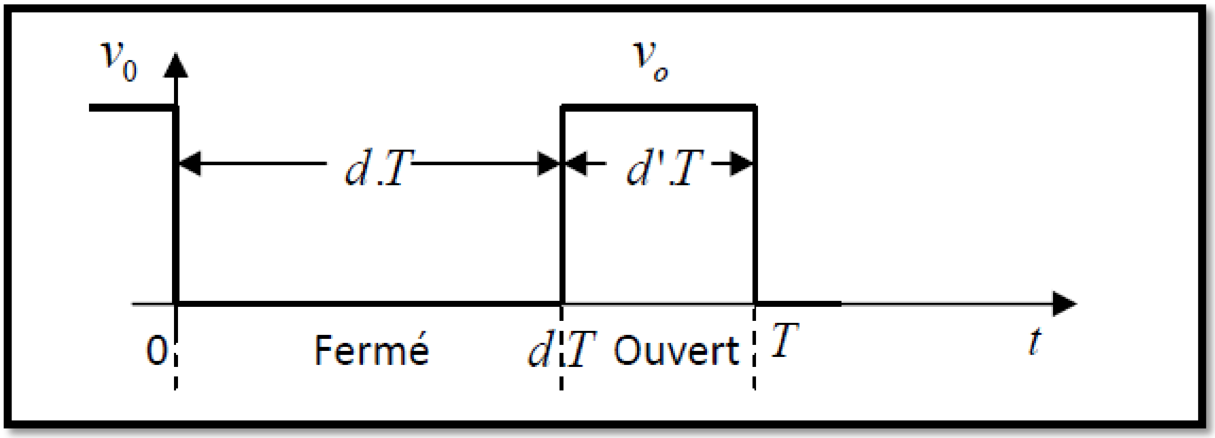

Figure I.9. closing and opening periods of a switch

We will dissect the operation of the booster converter into two distinct phases, contingent on the state of the switch Tp:

1. Energy Accumulation Phase (0 to αT): During this phase, the Tp switch is in the closed state, allowing for an increase in the inductor's current and the subsequent storage of energy in the form of magnetic energy. Simultaneously, diode D remains blocked, and the load is disconnected from the power supply.

2. Freewheeling Phase (αT to T): As we transition into this phase, the switch is open, and the inductor becomes part of the generator's circuit. Its electromotive force (e.m.f.) is additive to that of the generator, leading to a boost effect. The current, guided by the inductor, then passes through diode D, capacitor C, and load R. This results in the transfer of the energy previously accumulated in the inductor to the capacitance, ultimately establishing the desired output voltage.

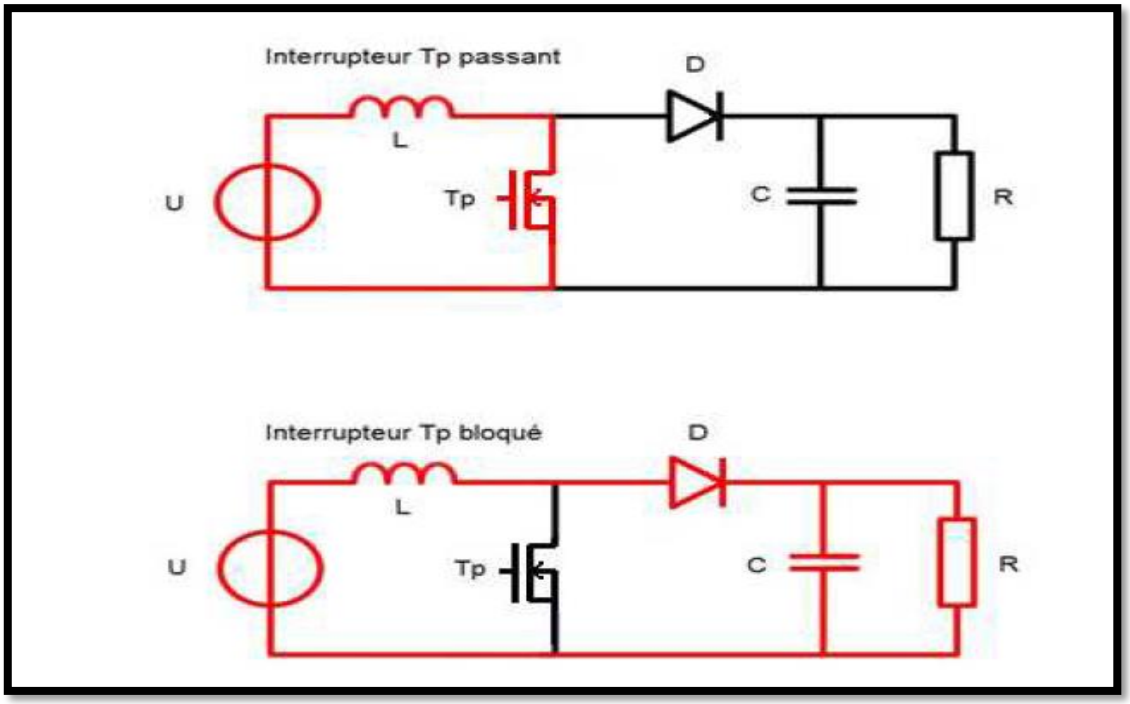

Figure I.10. operating phases of the booster converter.

I.2.3.1. Continuous conduction analysis:

The operation of this circuit can be systematically divided into two distinct stages, contingent upon the state of switch K.

1. **Energy Accumulation Phase (0 < t < αt, with α ∈]0, 1[):** During this phase, switch K is actively closed, and diode D remains in a blocked state. The equivalent circuit diagram for this stage is as follows:

We have :

$$Ve = L * \frac{di}{dt} \tag{I.28}$$

From where $i(t) = \frac{Ve}{L} * t + i_0$ (I.29)

At t= αt, the current will be maximum in the inductor.

$$i_{max} = \frac{Ve}{L} * \alpha t + i_0 \tag{I.30}$$

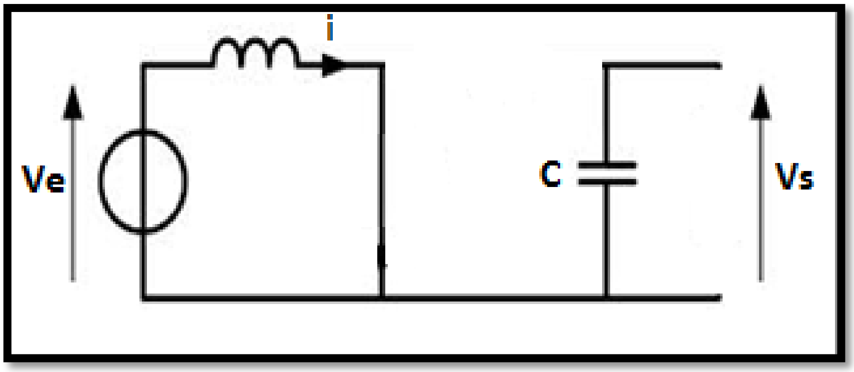

Figure I.11. Energy Accumulation Phase.

2. Energy Transfer: (αt < t < T)

We consider that the switch is now open, and diode D conducts. The equivalent diagram is as follows.

$$Ve - L * \frac{di}{dt} - Vs = 0 \tag{I.31}$$

From where: $Vs - Ve = L * \frac{di}{dt}$ (I.32)

$$i(t) = i_{max} - \frac{Vs - Ve}{L}(t - \alpha T) \tag{I.33}$$

At t=T, this current will be minimal and therefore equal to the current i_0

$$I_{min} = i_0 = i_{max} - \frac{Vs - Ve}{L}(1 - \alpha)T \tag{I.34}$$

Let Δi be the ripple of the current in the inductor

$$\Delta i = i_{max} - i_{min} \tag{I.35}$$

From equation (I.33) we draw

$$\Delta i = \frac{Ve}{L} * \alpha t \tag{I.36}$$

From equation (I.35) we draw

$$\Delta i = \frac{Vs - Ve}{L}(1 - \alpha)T \tag{I.37}$$

By combining these last two equations we obtain:

$$Vs = \frac{Ve}{1 - \alpha} \tag{I.38}$$

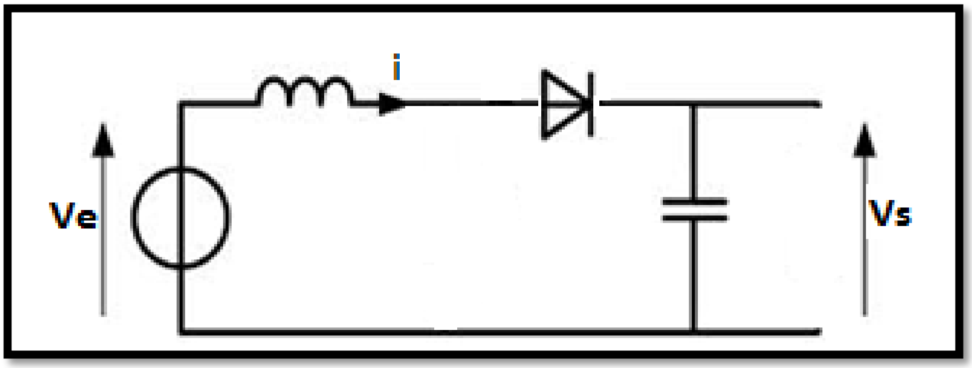

Figure I.12. Energy transfer.

In accordance with the aforementioned relationship, it becomes evident that the output voltage is contingent upon both the input voltage and the duty cycle α. It is important to note that α lies within the range of 0 to 1, characterizing the converter as a voltage booster.

In a theoretical context, the output voltage remains unaffected by changes in the load. However, in practical applications, the inherent imperfections of real components introduce disparities. These disparities result from the real-world imperfections inherent in the components used in the system.

As the converter is connected to a load, it gives rise to an output current flowing through this load. The magnitude of this current is contingent upon the load's value, with greater loads causing a decrease in the current. It's worth noting that an exceptionally low current value can prompt the circuit to transition into a discontinuous operating mode, leading to the concept of a continuous operating limit.[47,48]

I.2.4. MPPT

Specific control strategies are in place to optimize the operation of devices at their peak performance points, even when these points are not known beforehand, and without prior knowledge of when or why modifications to these points occur. This concept is particularly relevant for energy sources, where it translates into the quest for maximum power points. This approach is commonly referred to as "Maximum Power Point Tracking" or "MPPT" in the literature. The fundamental principle behind MPPT is to iteratively search for the Maximum Power Point (MPP) while ensuring a precise alignment between the power generator and its load, thereby enabling the transfer of maximum power.[49-53]

I.2.4.1. Perturb and Observe

Photovoltaic (PV) systems often exhibit initially low efficiency. To enhance their performance, the practice of maximum power point tracking is employed. In the perturb and observe method, minor perturbations are introduced to induce power variations. If an increase in voltage leads to a corresponding increase in power output, the operational point of the PV module is adjusted to the left of the MPP. The MPP is precisely situated at the point on the power curve of the PV array where the slope is zero, and the resistance matches the negative differential resistance. The adjustment of the photovoltaic (PV) array voltage consistently adheres to the prescribed algorithm designed to attain maximum power output. The flowchart outlining the implementation of the Perturb and Observe (P&O) algorithm for the charge controller can be found in Figure I.13.

The operational principle of Maximum Power Point Tracking (MPPT) controls employing the Perturb and Observe (P&O) method entails introducing a slight perturbation to the VPV (photovoltaic voltage) around its initial value and subsequently analyzing the resultant variation in PPV (photovoltaic power). Illustrated in Figure I.14, if a positive adjustment in VPV voltage results in an increase in PPV power, it signifies that the operating point is situated to the left of the Maximum Power Point (PPM).[54-60]

Conversely, a decrease in power implies that the system has moved beyond the PPM. A similar rationale applies when the voltage decreases. By scrutinizing the effects of voltage variations on the PPV (VPV) characteristic, it becomes feasible to precisely determine the operating point's position relative to the PPM and guide it toward the maximum power output through a suitable control strategy.

In essence, if an alteration in voltage leads to an increase in PV power, the direction of the perturbation is maintained. In contrast, if power decreases, the perturbation's direction is reversed to steer the system back towards convergence with the new PPM.

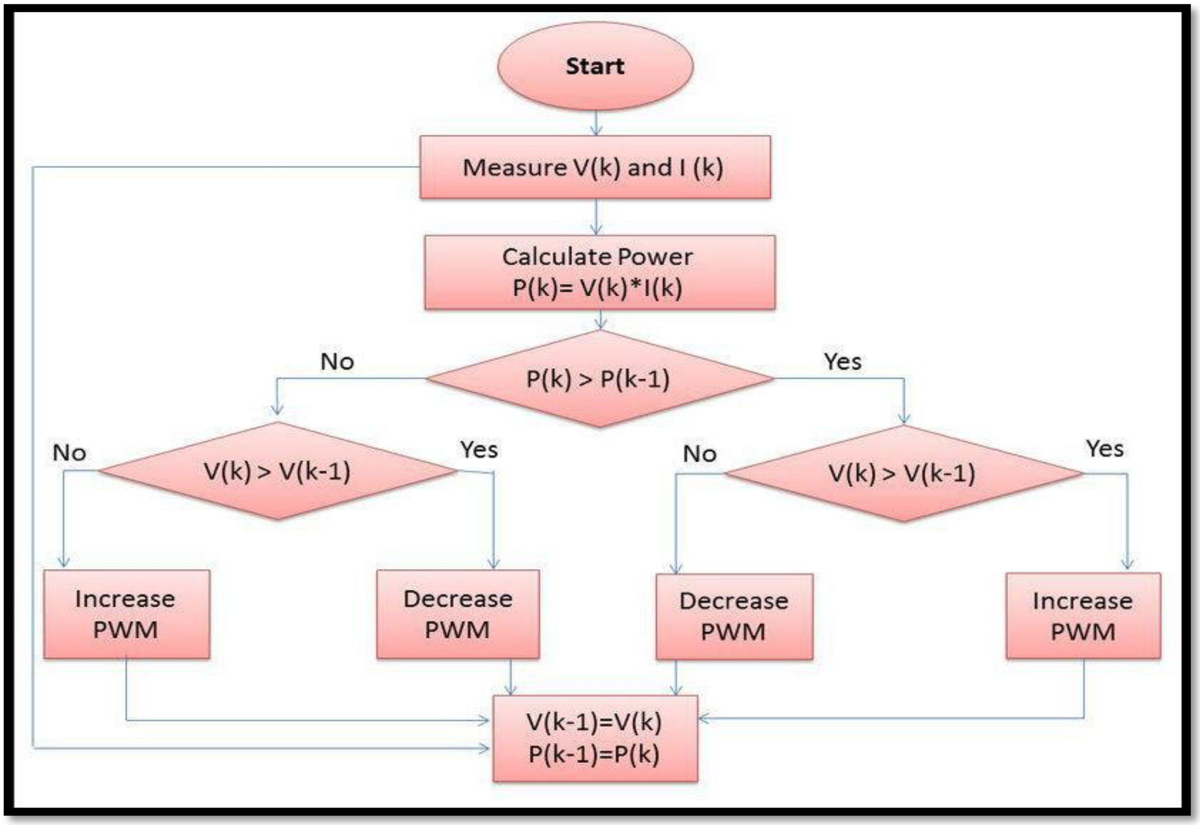

Figure I.13. Flowchart of the adopted P&O algorithm for the charge controller.

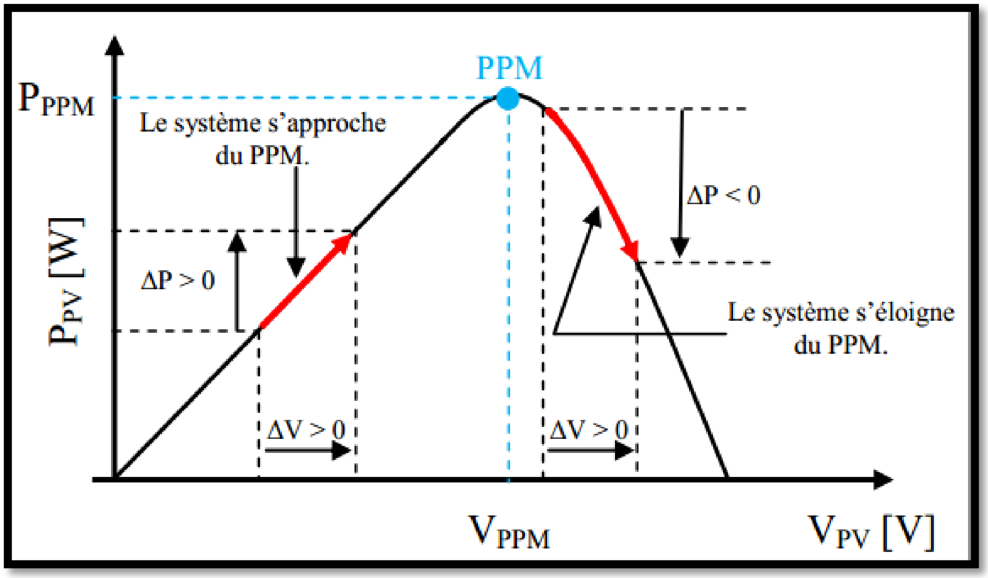

Figure I.14. MPPT working principle.

I.2.4.2. Incremental Conductance (InCond)

The Incremental Conductance (InCond) algorithm is a pivotal component in optimizing the performance of solar panels. Its operational principle involves an ongoing assessment of the solar panel's instantaneous conductance and its correlation with the incremental conductance.

Instantaneous conductance, in this context, is a real-time measure of the panel's ability to convert sunlight into electrical energy. On the other hand, incremental conductance represents the dynamic relationship between the power output and the voltage. It quantifies how the power output changes concerning variations in the voltage supplied to the solar panel.

The InCond algorithm is designed to maintain the solar panel at its maximum power point (MPP), which is the point at which the solar panel generates the most power. To do this, it continuously monitors the instantaneous conductance. When the instantaneous conductance exceeds the incremental conductance, it signifies that the solar panel can deliver more power than it currently does at the prevailing voltage level. In response, the algorithm raises the voltage supplied to the load. This action pushes the system closer to its MPP, ultimately leading to improved energy conversion efficiency.

Conversely, if the instantaneous conductance falls below the incremental conductance, it suggests that increasing the voltage would not result in a significant power output gain. In such instances, the InCond algorithm reduces the voltage supplied to the load, thereby ensuring the system operates efficiently and does not waste energy.

By continuously fine-tuning the voltage supplied to the solar panel, the InCond algorithm plays a critical role in ensuring that solar panels operate at their peak performance levels, maximizing energy production and enhancing the overall efficiency of solar energy systems. This approach is vital for harnessing the full potential of solar power and contributing to sustainable and renewable energy solutions.

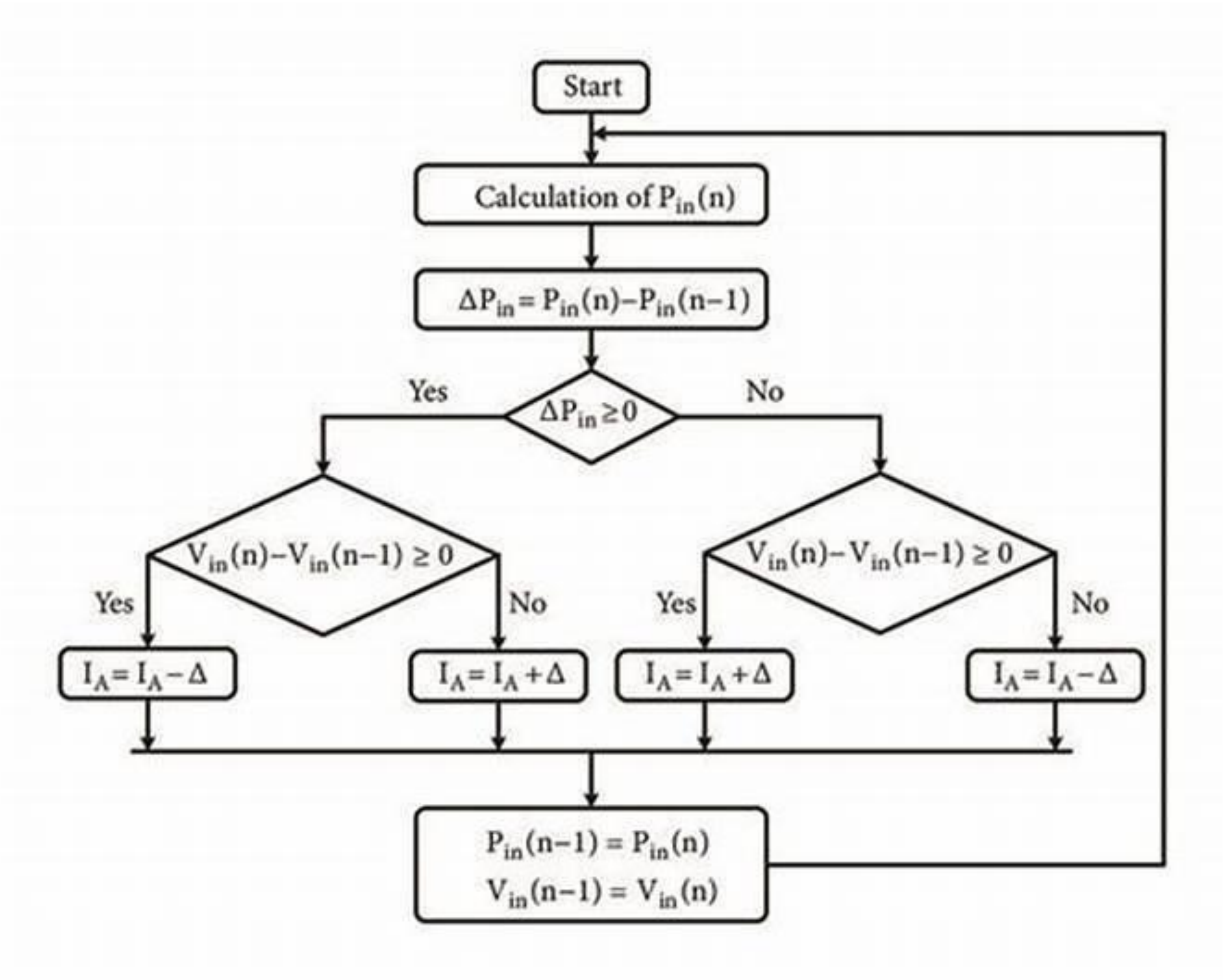

Figure I.16. A diagram of the Incremental Conductance (InCond) algorithm.

I.2.4.3. Benefits of MPPT

Maximum Power Point Tracking (MPPT) devices play a pivotal role in elevating the effectiveness of solar power systems. These devices, in certain scenarios, have the potential to augment the efficiency of a solar system by an impressive margin, with enhancements reaching as high as 30%. The underlying mechanism behind this remarkable boost in efficiency lies in the capability of MPPT devices to enable solar panels to consistently operate at their maximum power point. This optimal point represents the sweet spot at which the solar panel achieves its peak power output, ensuring that solar energy systems harness the maximum available energy potential from the sun.

Enhanced Battery Charging: The implementation of Maximum Power Point Tracking (MPPT) charge controllers brings substantial benefits to battery charging within solar systems. These controllers play a pivotal role in optimizing battery charging, ensuring that the battery receives the ideal voltage and current levels. This precise charging process not only extends the battery's lifespan but also enhances its performance, resulting in improved energy storage and discharge capabilities.

Cost-Efficiency: MPPT devices also offer a cost-effective advantage by enhancing the overall efficiency of the solar power system. Their ability to maximize energy conversion means that a smaller solar panel array can generate the same amount of energy as a larger one, thus reducing the upfront system costs. This cost-efficient approach not only makes solar energy more accessible but also strengthens its economic viability, promoting the widespread adoption of sustainable and renewable energy sources.

I.2.4.4. Applications of MPPT

Maximum Power Point Tracking (MPPT) devices find widespread application in the realm of solar charge controllers, playing a critical role in overseeing the regulation of voltage and current flow from solar panels to batteries. While it's true that MPPT charge controllers often come with a higher price tag compared to their non-MPPT counterparts, the long-term benefits they confer more than justify the initial investment. By significantly boosting the energy harvested from solar panels, MPPT charge controllers lead to substantial cost savings over time, making them a financially prudent choice for those seeking optimal energy efficiency in their solar systems.

Beyond solar applications, MPPT devices have found utility in various other domains, including wind turbines and fuel cells. In these diverse contexts, MPPT devices fulfill the vital role of maximizing power extraction from variable energy sources. Their adaptability and efficiency-enhancing capabilities make them a versatile and indispensable component in the pursuit of harnessing renewable energy and reducing reliance on conventional power sources.

Conclusion

In this chapter, an extensive exploration of switched reluctance motors (SRM) has been undertaken, encompassing the delineation of diverse SRM types, an elucidation of their operational principles, and a comprehensive examination of their power supply mechanisms. Furthermore, a comprehensive overview has been provided for photovoltaic systems alongside an analysis of maximum power point tracking (MPPT) techniques.

Introduction

In this chapter, our focus will be on modeling a photovoltaic system that powers an SRM motor. We'll delve into the various components of the system, including the SUNTECH PV module, boost converter, and H-bridge converter. To achieve optimal geometric dimensions and precise operational predictions for the motor, it is crucial to have a deep understanding of the magnetic field's distribution across all its active regions. The most reliable approach for accurately determining the electromagnetic characteristics during non-linear operation is through precise magnetic field calculations. Therefore, the use of a numerical method capable of delivering exceptional precision while minimizing the complexity of equations, such as the Finite Element Method (FEM), is imperative. To analyze the magnetic field for different combinations of excitation currents and rotor angular positions, multiple iterations are required. Several modeling software applications, notably "FEMM," are grounded in the principles of FEM, facilitating the assessment of saturation levels and a thorough examination of flux distribution throughout various segments of the magnetic circuit.

II.1. Photovoltaic module

Within our modelling framework, we employ a SUNTECH PV module, specifically depicted in Figure II.1, accessible at the research centre, FAB.Lab, within Mohamed Khaider Biskra University. This particular PV module is constructed using monocrystalline silicon and comprises a total of 72 individual PV cells. Under standard test conditions (CST), it demonstrates the capacity to produce 190 W of power, accompanied by a current rating of 5.20A, all at an optimal voltage level of 36.6V.

SUNTECH

Model Number		STP190S-24/Ad+
Rated Maximum Power	(P_{max})	190W
Output Tolerance		0/+5%
Current at Pmax	(I_{mp})	5.20A
Voltage at Pmax	(V_{mp})	36.6V
Short-Circuit Current	(I_{sc})	5.62A
Open-Circuit Voltage	(V_{oc})	45.2V
Nominal Operating Cell Temp.	(T_{NOCT})	45°C±2°C

Weight	15.5kg
Dimension	1580mm×808mm×35mm
Maximum System Voltage	1000V
Maximum Series Fuse Rating	15A
Cell Technology	mono-Si
Application Class A	

All technical data at standard test condition
AM=1.5 E=1000W/m² Tc=25°C

WARNING Hazardous electricity can shock, burn or cause death. Do not touch terminals.

Add: 17-6 ChangJiang South Road, New District Wuxi, China 214028
Customer Service Hot Line: +86 400 8888 009 Fax: +86 510 8534 3321
Made in China

Figure II.1. Photovoltaic solar panel of the SUNTECH type.

To augment the operational voltage of photovoltaic (PV) cells, a common strategy involves connecting them in series. This configuration aligns with the objective of matching the nominal voltage of the module to the load, optimizing overall system performance. Moreover, recognizing the inherent vulnerability of PV cells to breakage and corrosion, protective measures are imperative. As a standard practice, these cells are encapsulated beneath either glass or a plastic compound to shield them from environmental factors. This integrated assembly, comprising protected PV cells, is referred to as a photovoltaic module. To further enhance the utility of these modules, they can be interconnected both in series and in parallel, thereby augmenting both voltage and current outputs for enhanced operational efficiency.

In a parallel analogy, the structure of the photovoltaic generator can be likened to a matrix, wherein it is constituted by Ns modules arranged in series and Np branches configured in parallel. This modular configuration allows for a systematic organization of photovoltaic elements, facilitating an optimized interplay of series and parallel connections to meet specific operational requirements. Such a matrix-like arrangement not only underscores the modular nature of the generator but also affords a versatile framework for scalability and adaptability in addressing diverse energy generation needs.

II.1.2. Current-voltage characteristic (I-V)

This represents a foundational attribute of the solar module, akin to a P-N junction with one direction obstructed. However, it undergoes a displacement along the current axis, directly correlated with the incident irradiance. This characteristic is delineated under constant illumination and temperature conditions, as illustrated in Figure II-1. The modulation of the current axis position provides a key insight into the module's response to varying irradiance levels, which is essential for understanding its dynamic behaviour under fixed environmental parameters.

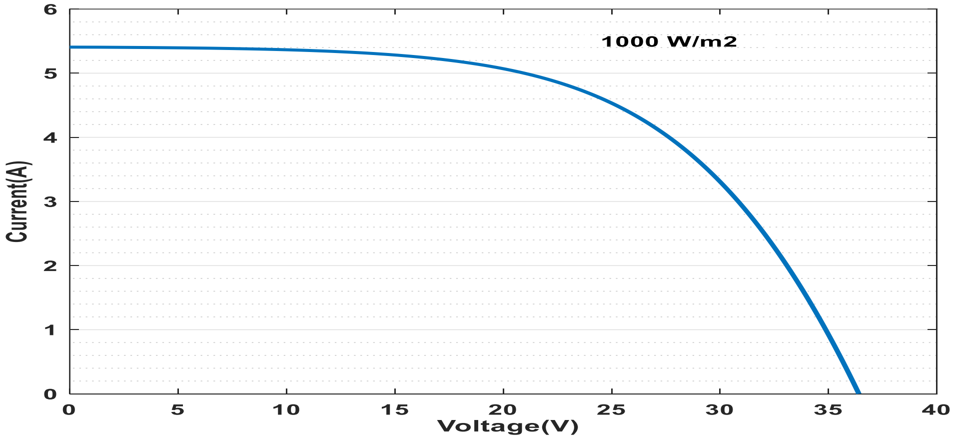

Figure II.1. I(V) characteristics of a solar module, (T=25°C).

II.1.3. Power-voltage (P-V) characteristic

The power output from the photovoltaic module is contingent upon its operational state. This power delivery is determined as the product of the current intensity and the voltage across its terminals, as depicted in Figure (II-2). Within this representation, the "M" point signifies the operational state at which the module achieves its maximum power output. Understanding and identifying this specific point is pivotal in optimizing the performance of the photovoltaic module for efficient energy conversion.

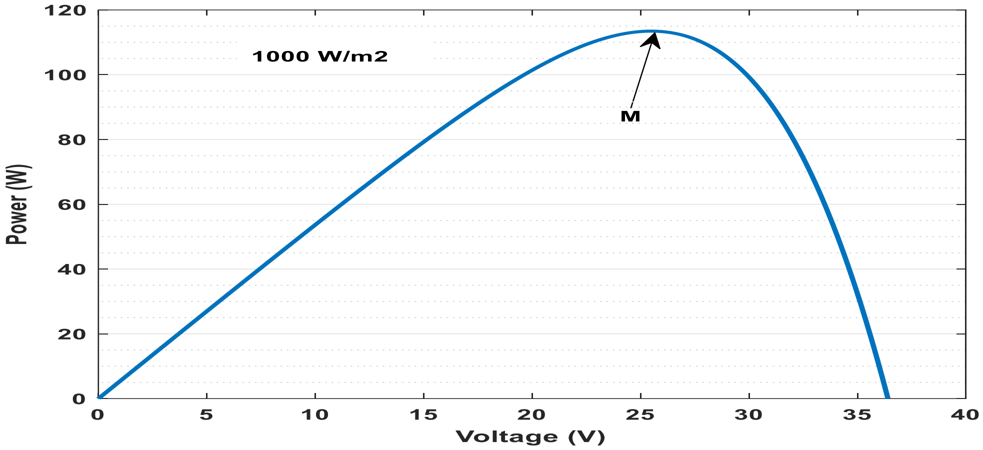

Figure II.2. P(V) characteristics of a solar panel.

II.1.4. the yield

This factor defines the rate of conversion of light energy into electrical energy; it represents the ratio of the power supply compared to that of the incident radiation.

$$\eta = \frac{I \cdot V}{G \cdot A_1} \tag{II.1}$$

II.1.5. Solar module operating zone

Distinct zones on the current-voltage (I-V) characteristic (Figure II-3) delineate varying operational states of the photovoltaic generator. These zones are categorized as follows:

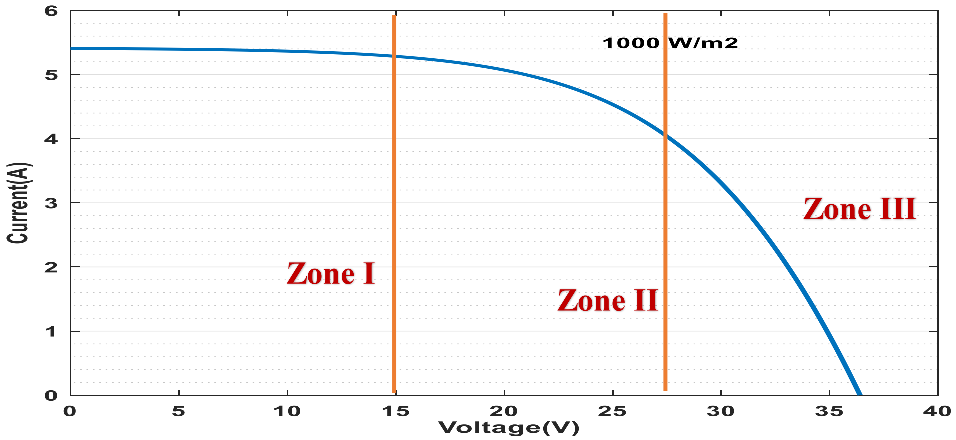

Figure II.3. The different zones of the I(V) characteristic, T=25°C.

- Zone (I): Characterized by a consistent current output irrespective of the voltage, this zone denotes a mode wherein the photovoltaic generator functions akin to a current generator.
- Zone (II): Representing the inflexion point on the characteristic curve, this intermediate region between Zones (I) and (III) is identified as the optimal operating region. It is in this

zone that the generator achieves its maximum power output, defining the preferred operational point.

- Zone (III): Marked by a fluctuation in current corresponding to a relatively constant voltage, this zone portrays the generator's behaviour resembling that of a voltage generator. Understanding and navigating these distinct zones are crucial for optimizing the performance of the photovoltaic generator across various operating conditions.

II.1.5. Effect of illumination

Figures (II-4) and (II-5) visually articulate the impact of incident illumination variation on voltage and extracted power characteristics, respectively. With an escalation in illumination, a nearly linear augmentation in the short-circuit current is observed, accompanied by a marginal decrease in the open-circuit voltage. This consequential interplay contributes to an overall increase in the extracted power, underscoring the sensitivity of the photovoltaic system's performance to changes in incident illumination levels. This nuanced understanding of the illumination-dependent variations in voltage and power characteristics is instrumental for optimizing the overall energy output of the photovoltaic system under dynamic environmental conditions.

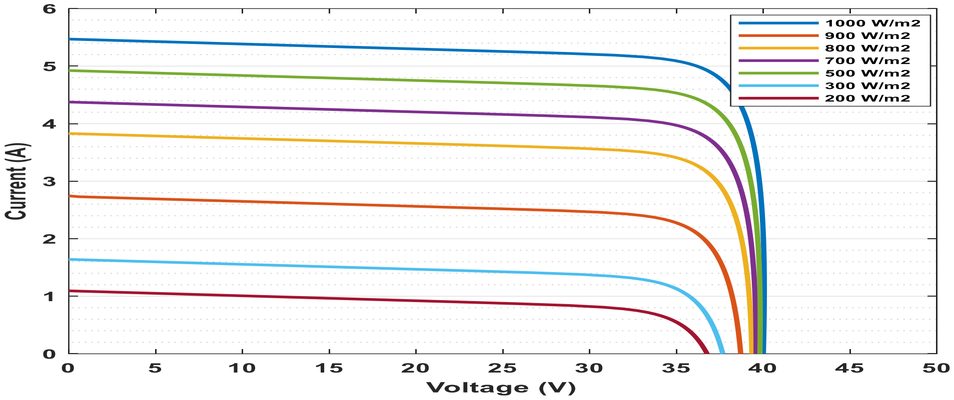

Figure II.4. I(V) characteristics of a solar panel.

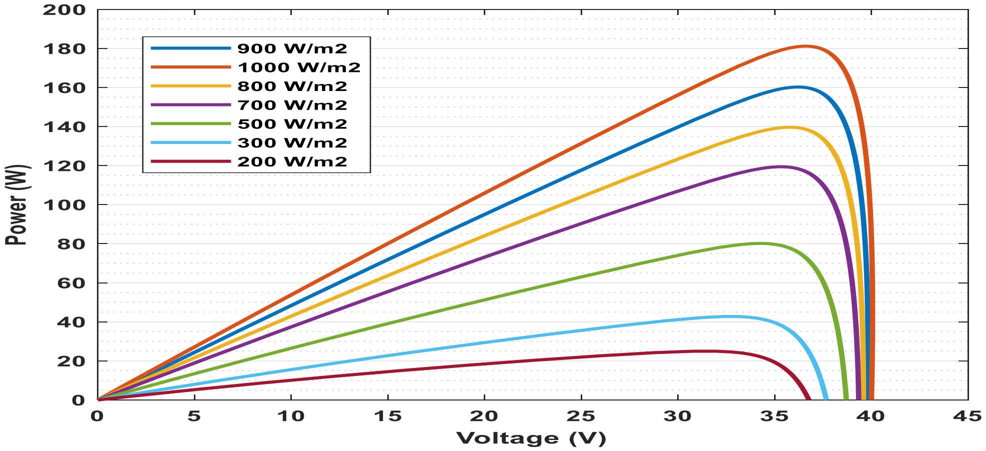

Figure II.5. P(V) characteristics of a solar panel for different illuminances.

II.2.Medium model of the boost converter

The DC/DC booster model is shown in the figure II.6

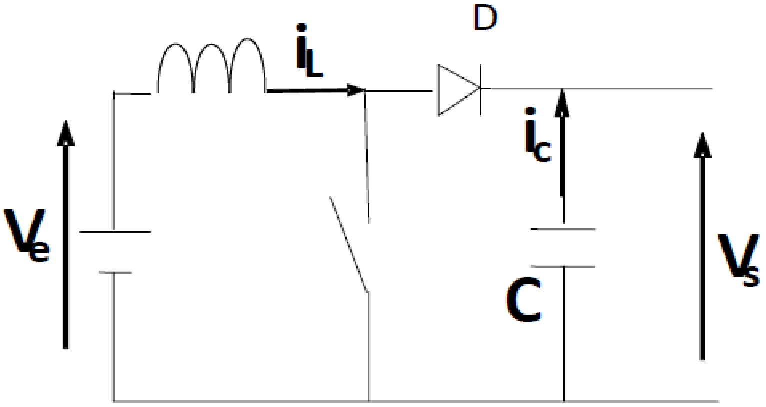

Figure II.6. Boost converter.

When dealing with a linear system, the representation of the system's state assumes the following form:

$$\begin{cases} \dot{x} = Ax + Bu \\ Y = Cx \end{cases} \qquad \text{(II.2)}$$

where what:

x: state vector;

$x = [x1, x2] = [i_L, v_c]$.

u: control vector, A: state matrix, B: input matrix and C: output matrix.[61,62]

II.2.1.Operating sequences and equations of state

II.2.1.1.First conduction sequence [0 to αT]

The circuit exhibits dynamic behavior characterized by the transistor Tr being in the "on" position while the diode is in the "off" position. The dynamic response of the circuit is expressed by:

$$V_e = L\frac{di_L}{dt} \qquad \text{(II.3)}$$

$$\dot{x}_1 = \frac{V_e}{L} \qquad \text{(II.4)}$$

$$v_c = \frac{1}{c}\int i_c dt \qquad \text{(II.5)}$$

$$\dot{x}_2 = \frac{1}{c} i_c \qquad \text{(II.6)}$$

$$i_c = \frac{v_c}{R} \qquad \text{(II.7)}$$

Where:

$$\begin{bmatrix}\dot{x}_1\\ \dot{x}_2\end{bmatrix} = \begin{bmatrix}0 & 0\\ 0 & \frac{1}{Rc}\end{bmatrix}\begin{bmatrix}x_1\\ x_2\end{bmatrix} + \begin{bmatrix}\frac{1}{L}\\ 0\end{bmatrix}V_e \tag{II.8}$$

Which can be written in the form:

$$\begin{aligned}\dot{x} &= A_1 x + B_1 V_e\\ V_s &= C_1 x\end{aligned} \tag{II.9}$$

With: $C_1 = [0 \quad 1]$

II.2.1.2.Second conduction sequence [αT to T]

The transistor Tr is in the “off” position and the diode is in the “on” position.

$$L\frac{di_L}{dt} = V_e - V_c \tag{II.10}$$

$$c\frac{dV_c}{dt} = i_L - \frac{V_c}{R} \tag{II.11}$$

$$\dot{x}_1 = \frac{V_e}{L} - \frac{1}{L}x_2 \tag{II.12}$$

$$\dot{x}_2 = \frac{1}{c}x_1 - \frac{1}{Rc}x_2 \tag{II.13}$$

Where:

$$\begin{bmatrix}\dot{x}_1\\ \dot{x}_2\end{bmatrix} = \begin{bmatrix}0 & -\frac{1}{L}\\ \frac{1}{c} & -\frac{1}{Rc}\end{bmatrix}\begin{bmatrix}x_1\\ x_2\end{bmatrix} + \begin{bmatrix}\frac{1}{L}\\ 0\end{bmatrix}V_e \tag{II.14}$$

Which can be put in the form:

$$\begin{aligned}\dot{x} &= A_2 x + B_2 V_e\\ V_s &= C_1 x\end{aligned} \tag{II.15}$$

II.2.2.Medium model

From equations (II.8) and (II.14), we can deduce the average form x and Vs for the entire period:

$$\dot{x}_1 = (A_1 x + B_1 V_e)\alpha + (A_2 x + B_2 V_e)(1-\alpha) \tag{II.16}$$

$$V_s = (C_1\alpha + C_1(1-\alpha))x \tag{II.17}$$

With: $$A = A_1\alpha + A_2(1-\alpha)$$ $$B = B_1\alpha + B_2(1-\alpha)$$

Where: A: state matrix; B: control matrix.

The average model of the booster converter is:

$$\begin{cases} \dot{x_1} = -\frac{1-\alpha}{L}x_2 + \frac{1}{L}u \\ \dot{x_2} = \frac{1-\alpha}{c}x_1 - \frac{1}{Rc}x_2 \end{cases} \tag{II.18}$$

II.3. Modeling of Switched reluctance motor

II.3.1. Magnetic field equations

The simulation can be accurately executed by applying Maxwell's equations within the framework of static states. Describing these equations involves representing them as a scalar equation that articulates the magnitude of the vector potential A within a Cartesian coordinate system:[63-67]

$$\frac{\partial}{\partial x}\left(\frac{1}{\mu}\frac{\partial A}{\partial x}\right) + \frac{\partial}{\partial y}\left(\frac{1}{\mu}\frac{\partial A}{\partial y}\right) + J = 0 \tag{II.19}$$

J: the magnitude of the excitation current density vector.

μ : magnetic permeability.

In solving the equation pertinent to the engine, consideration will be given to the continuity conditions of the magnetic field along the interfaces. Additionally, a Dirichlet boundary condition will be imposed on the exterior contour of the air, specifying that the vector potential A equals zero in that region.

II.3.2. Finite element method

In the realm of designing electromagnetic structures, the finite element method has emerged as a widely adopted tool. It involves the pursuit of an approximate solution derived from discretizing the field under investigation, upon which the Maxwell equations are solved. This method facilitates the determination of a scalar, vector, or even tensor field that complies with a set of partial differential equations and ordinary equations at any point within the study domain and at any given time while adhering to specified boundary conditions.

When time is absent as a variable in the formulation, the scenario is referred to as stationary. Conversely, if time is considered a variable, it constitutes an evolution problem .The simulation domain is divided into elements, and approximate solutions are constructed on these elements. The unknowns in this context are the values of the solution at a finite set of points, namely the nodes of the discretization. Figure (II.6) illustrates the calculation of a potential for each point in this discretized representation.

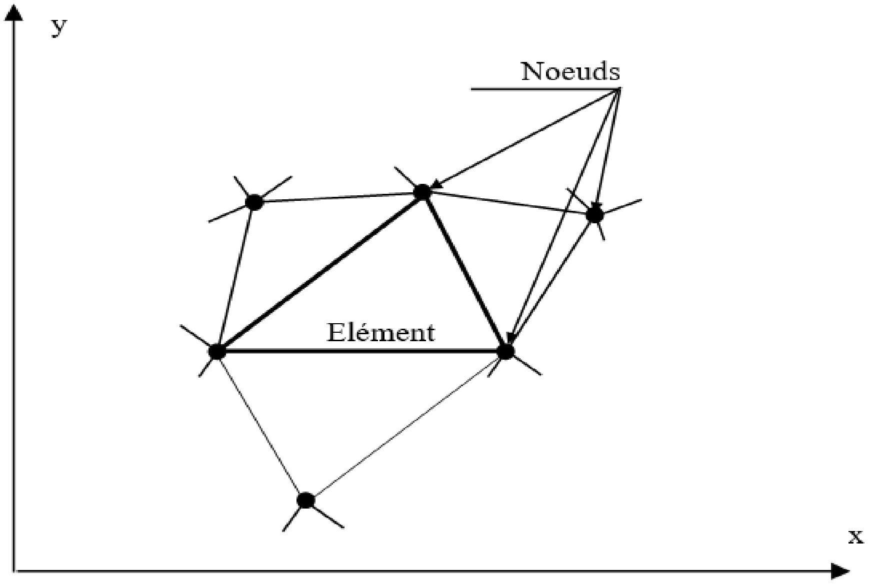

Figure II.6. Discretization by finite elements in two dimensions.

Let's consider a homogeneous Ω domain, which is subdivided into M' finite elements and M boundary elements. The discretization of the integral formulation for this scenario can be expressed as follows:

$$\overset{\overset{e=1}{M'}}{\Sigma} \iint_{\Omega_{e'}} \frac{1}{\mu}\left(\frac{\partial N}{\partial X}\frac{\partial A}{\partial X} + \frac{\partial N}{\partial Y}\frac{\partial A}{\partial Y}\right) d\Omega_{e'} = \overset{\overset{e=1}{M}}{\Sigma} \int_{\Gamma e} \frac{1}{\mu} N * \frac{\partial A}{\partial n} d\Gamma_e + \overset{\overset{e'=1}{M'}}{\Sigma} \iint_{\Xi_{e'}} NJd\Omega_{e'} \tag{II.20}$$

The nodal approximations of the vector potential and its normal derivative are functions of reference coordinates ξ and η:

$$A = \overset{\overset{j=1}{N_n}}{\Sigma} N_J(\xi,\eta).A_{IJ} \tag{II.21}$$

$$\frac{\partial A}{\partial n} = \overset{\overset{j=1}{3}}{\Sigma} N_J * (\xi).\left(\frac{\partial A}{\partial n}\right)_{IJ} \tag{II.22}$$

"Nn" represents the count of interpolation nodes associated with the considered finite element within the Ω_e domain. For a curvilinear quadratic triangle, the value of Nn is four, while for a curvilinear quadratic quadrilateral, it amounts to six. The functions denoted as "N" correspond to the shape functions associated with these particular finite elements.

II.3.3. Calculation of electromagnetic parameters

The value of magnetic induction flux which passes through a closed circuit Λ is given by:

$$\varphi = \oint_{\Lambda} A\,.\,dl \tag{II.23}$$

The inductance of a phase winding in a variable reluctance motor can be determined by evaluating the induction flux passing through that specific phase. The electromagnetic torque, denoted as Ce, exerted on the motor shaft is then computed using the following expression:

$$C_e = \frac{1}{\mu_0} L_n \int_{\Gamma_R} \left[(r \times B)(B.n) - \frac{1}{2} B^2 (r \times n) \right] d\Gamma \tag{II.24}$$

Where

$$B = rot(A) \tag{II.25}$$

B: the magnetic induction,

A: the magnetic vector potential

ΓR: the interface of the rotor and the motor interface,

Ln: the length of the magnetic core of the motor.

II.3.4. Numerical results

The computation is conducted through the utilization of FEMM software, with programming executed in the LUA language. FEMM operates on the resolution of the Maxwell equations employing the finite element method. This computational approach has been applied specifically to calculate the magnetic field in a switched reluctance motor characterized by 6 poles at the stator, 4 poles at the rotor, and a three-phase configuration. Each stator phase is composed of two opposed stator poles, as illustrated in Figure II.7.[63-65]

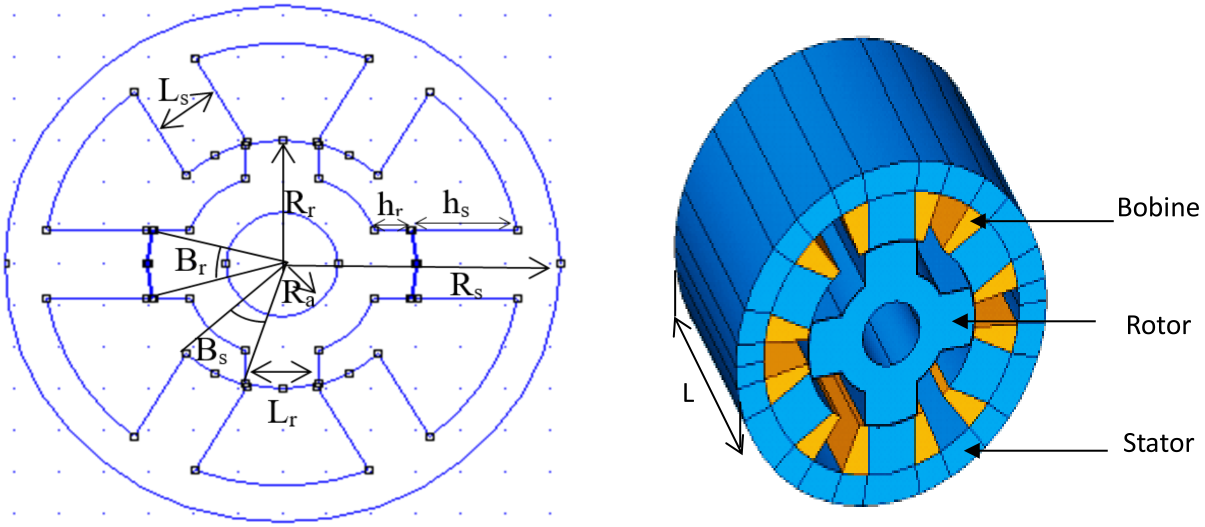

Figure II.7. switched reluctance motor 6/4.

II.3.5. Table of main geometric dimensions of the motor

Titled	**Notation**	**Dimensions**
Stator outer radius	R_s	**124.7 mm**
Length	**L**	**59.65 mm**
Rotor radius	R_r	**59.75 mm**
Air gap	**e**	**0.54 mm**
Stator polar arc	B_s	**30.85°**
Rotor polar arc	B_r	**32.26°**
Stator pole width	L_s	**16.18 mm**
Rotor pole width	L_r	**16.6 mm**
Stator pole height	h_s	**9 mm**
Rotor pole height	h_r	**10 mm**
Tree Radius	R_a	**25 mm**
Number of turns per phase	N_s	**312**
Steel	**M19**	**M19**

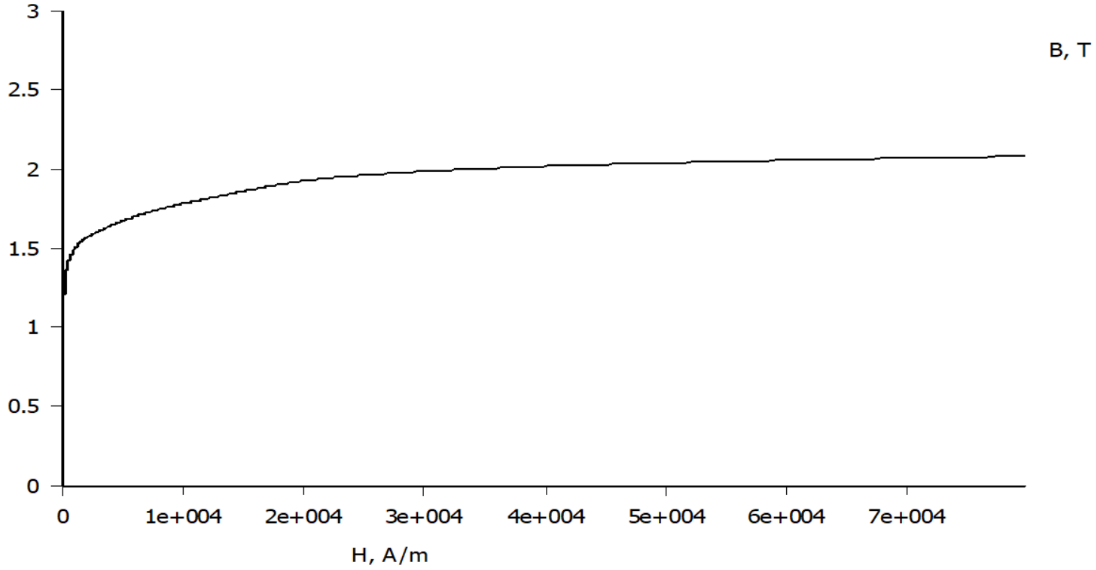

Figure II.8. magnetization curve of M19, B=f'(H).

II.3.6. Field lines for the two extreme positions and mesh

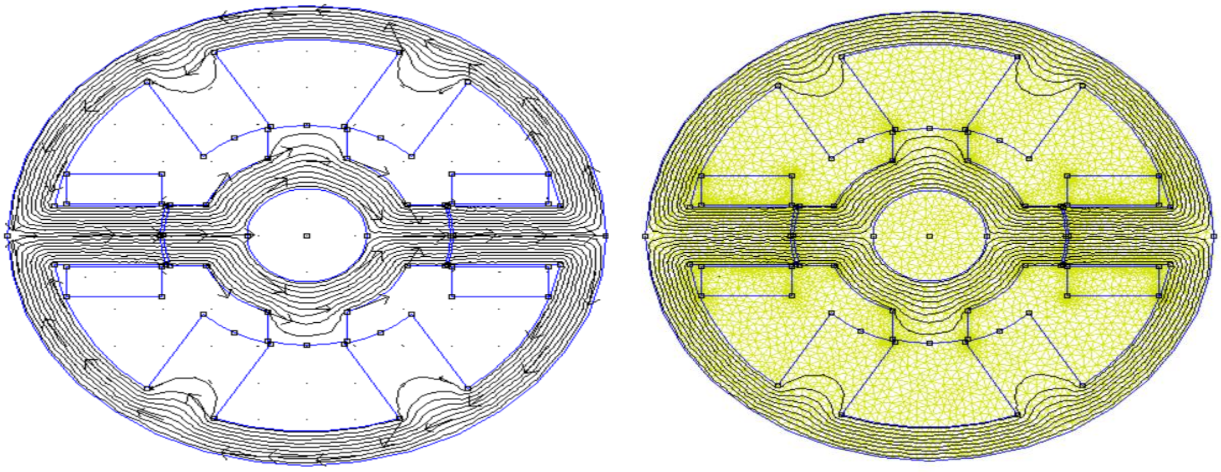

Figure II.9.a. Position conjonction.

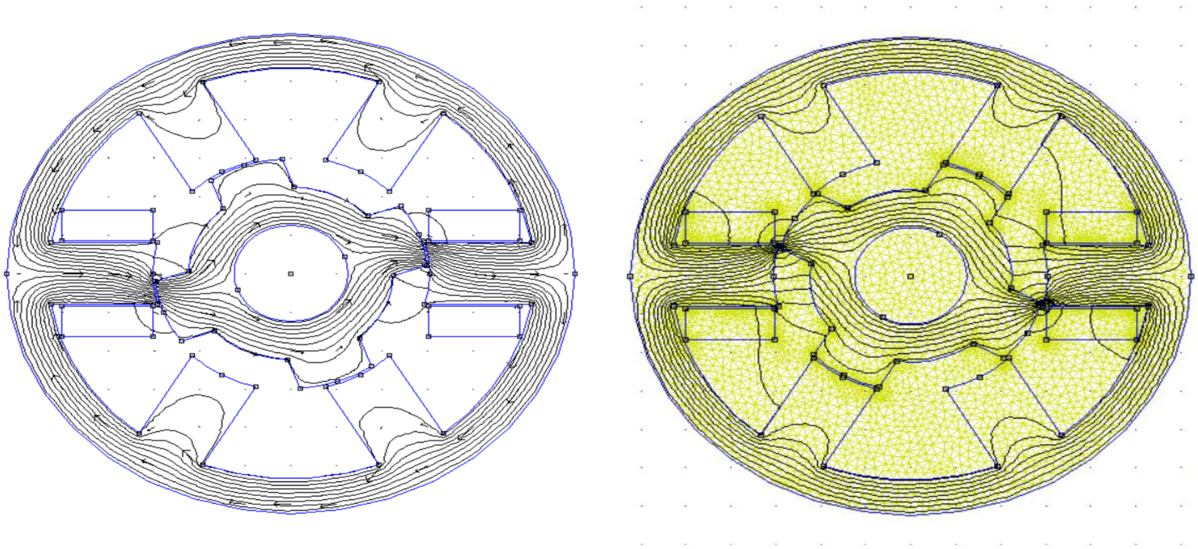

Figure II.9.b. Position opposition.

In Figure (II.9), the magnetic line distribution within a motor is depicted when a current of 8A is applied. Subfigures (a) and (b) of Figure (II.9) represent distinct rotor positions.

In Figure (II.9.a), the rotor is positioned at the conjunction point (θ° = 0°). At this particular angle, the phase inductance reaches its maximum value, denoted as Lmax. This signifies the point in the rotor's rotation where the inductance is at its peak within the given interval.

Contrastingly, Figure (II.9.b) illustrates the rotor in the opposite position (θ° = 45°). At this angle, the phase inductance reaches its minimum value, denoted as Lmin, in the interval. The magnitude of this inductance is of significance as it represents the lowest point in the inductance profile during the rotor's rotation. Understanding both the maximum and minimum inductance values is crucial for comprehending the motor's performance characteristics at different rotor positions.

II.3.7. Distributions of the vector field and induction density for the two extreme positions

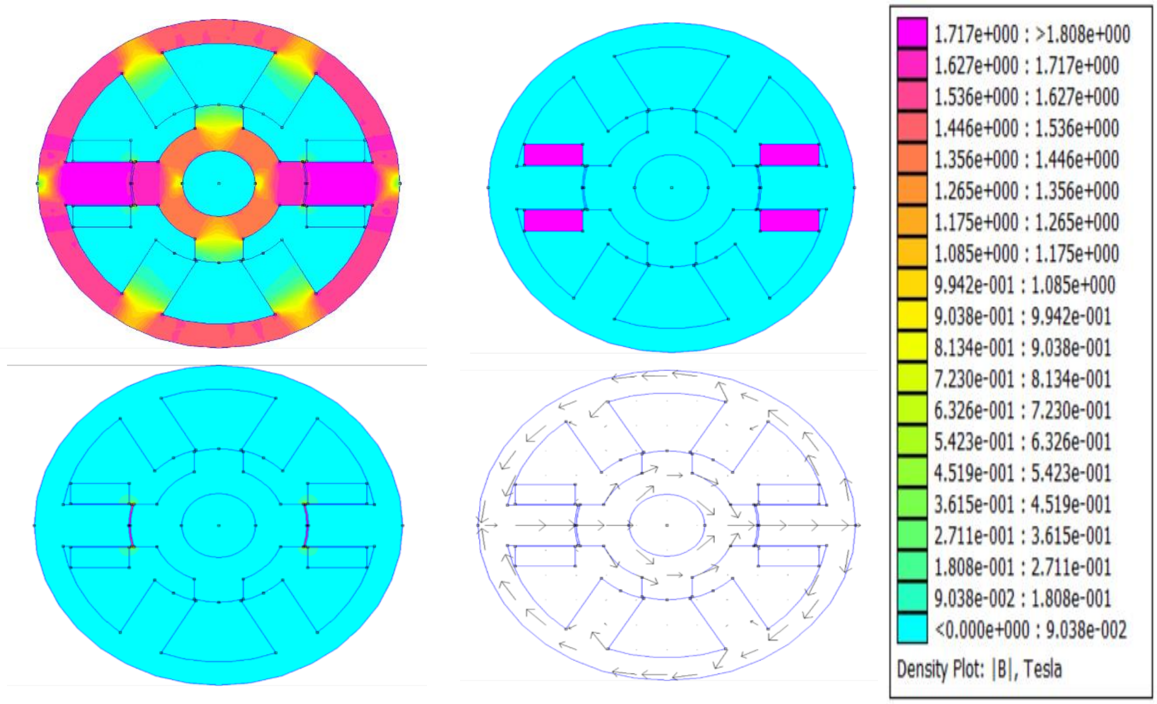

Figure II.10. a: Flux density (T), b: Field Intensity (A/m), c: Current density (MA/m^2) and c: induction vector field in conjonction position.

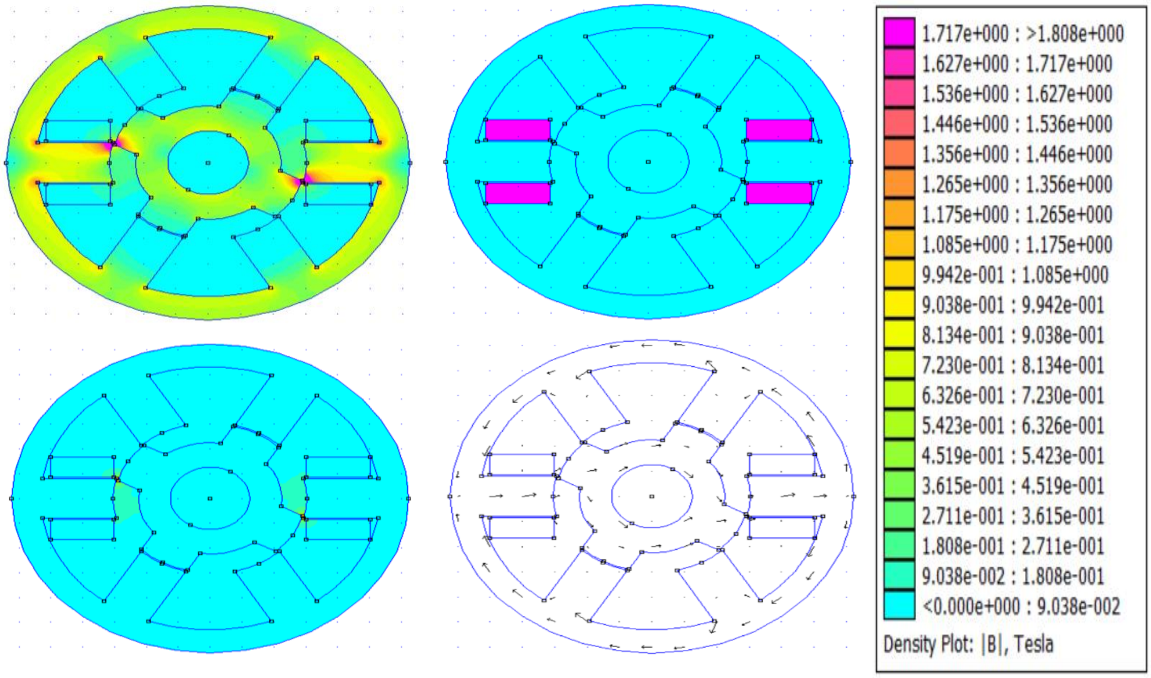

Figure II.11. a: Flux density (T), b: Field Intensity (A/m), c: Current density (MA/m^2) and c: induction vector field in opposition position.

We observe that the induction density is more pronounced when the rotor is in the conjunction position and less intense when it is in the opposition position. The deformation of the vector field in the conjunction position is attributed to the alternating increase and decrease of the air gap.

Induction Density Variation: When the rotor is in the conjunction position (where the rotor and stator align, θ° = 0°), the induction density is noted to be stronger. This implies that the magnetic field is more concentrated or intense at this specific rotor angle.

Conversely, when the rotor is in the opposite position, the induction density is weaker. In this scenario, the magnetic field is less concentrated or exhibits lower intensity compared to the conjunction position.

Deformation of a Vector Field: The term "vector field" refers to the distribution and behaviour of the magnetic field vectors.

The observed deformation in the vector field during the conjunction position is explained by the concurrent increase and decrease of the air gap. As the rotor moves into conjunction, the air gap between the rotor and stator decreases, causing a concentration and intensification of the magnetic field. This variation in the air gap results in a corresponding deformation of the vector field, which is visually apparent in the distribution of magnetic lines.

Understanding these induction density variations and vector field deformations is crucial for analyzing and optimizing the performance of the motor at different rotor positions.

II.3.8. Magnetization characteristic

II.3.8.1. Flux characteristic

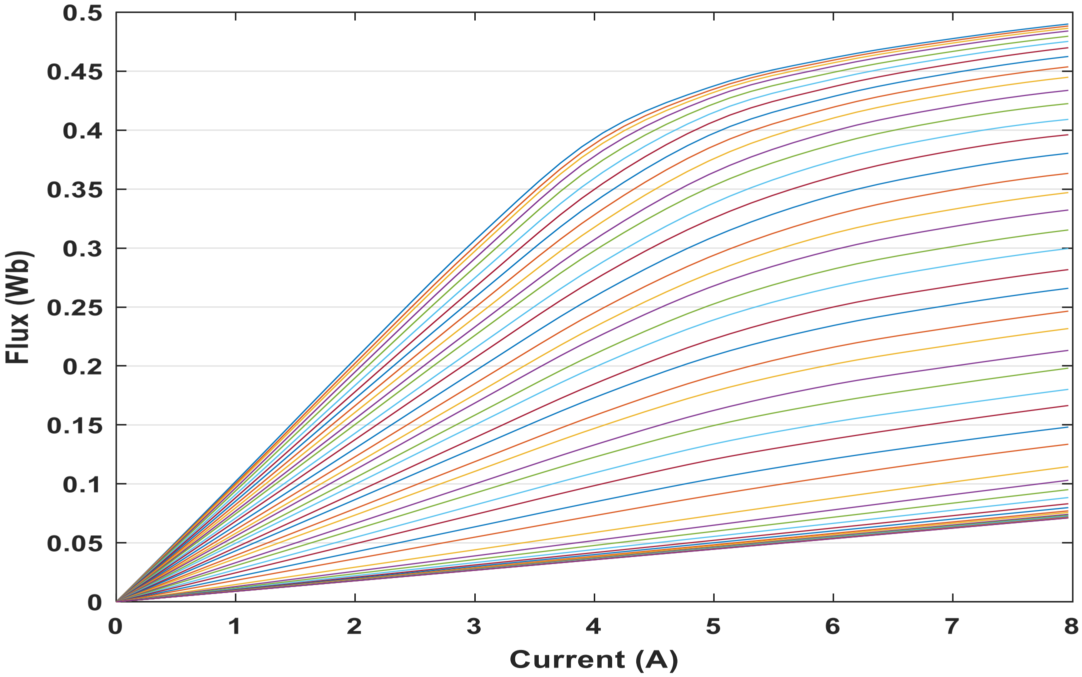

Figure II.12. Flux as a function of rotor offset and currents.

Figure II.12 serves as a visual tool to comprehend the influence of rotor position and phase current amplitude on magnetic flux, with particular attention to the effects of saturation in the motor. The graphical representation in Figure II.12 encapsulates a network of curves, each curve corresponding to a specific combination of rotor position and phase current amplitude. The lowest curve signifies the unaligned position, emphasizing the state where the rotor is furthest from alignment with the stator. In contrast, the top curve denotes the aligned position, indicating the configuration where the rotor aligns most closely with the stator.

II.3.8.2. Torque characteristic

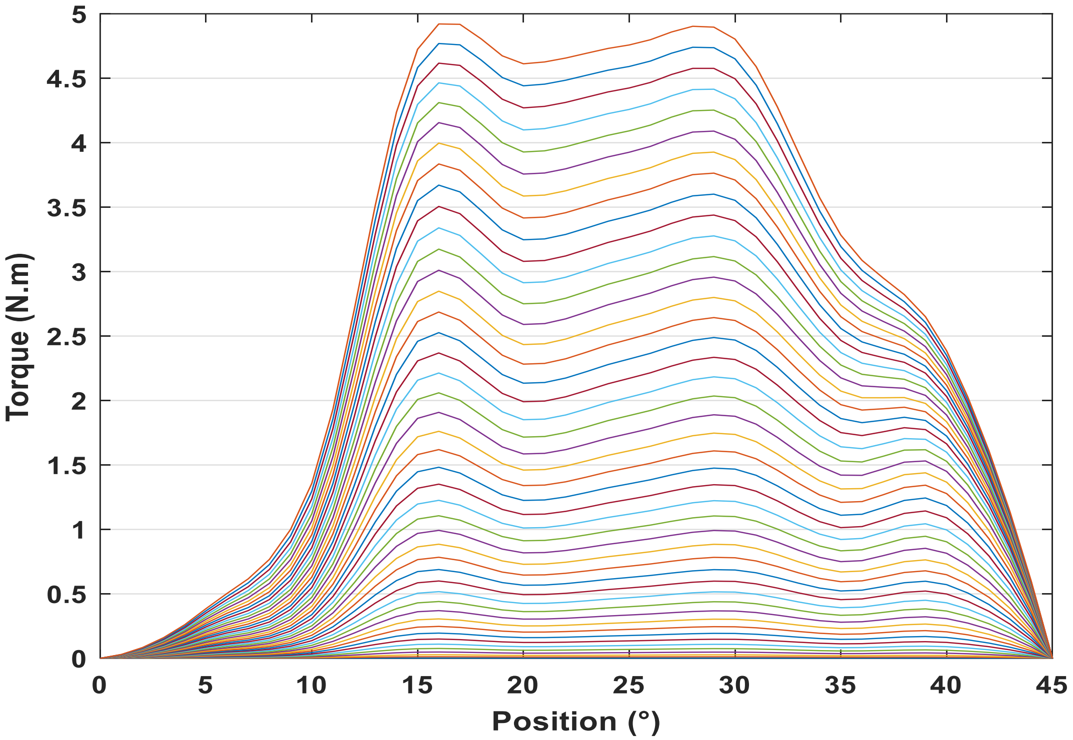

Figure II.13. Torque as a function of rotor offset and current.

Figure II.13 provides a comprehensive representation of the electromagnetic torque in relation to both the rotor position and varying phase current values. This visual depiction serves as a valuable tool for understanding how the torque is influenced by the interplay of rotor position and the amplitude of the phase current. A notable feature revealed by the figure is the impact of the nonlinearity inherent in the magnetic characteristic on the resulting torque profile.

To generate this torque curve, interpolation techniques were employed, leveraging the multitude of intermediate points derived from the Finite Element Method (FEM) analysis. The utilization of interpolation was deemed effective due to the abundance of detailed data points obtained through FEM analysis, ensuring a smooth and accurate representation of the torque across the entire range of rotor positions and phase current values.

A noteworthy observation in Figure II.13 is the phenomenon where the torque decreases as the rotor position approaches alignment. This intriguing behavior can be attributed to the influence of saturation, a condition that mitigates the co-energy variation and consequently diminishes the overall torque. This nuanced understanding of the torque behavior near alignment enhances our grasp of the motor's operational characteristics.

Furthermore, the figure illustrates that the maximum torque is directly proportional to the current. This correlation highlights a fundamental aspect of the motor's behavior, emphasizing the significance of the applied current in determining the torque output. Notably, the examination of the machine's behavior at the maximum torque operating regime reveals a resemblance to a series excitation direct current machine, unveiling a parallel in behavior between the two systems under certain operational conditions.

II.3.8.3. Inductance characteristic

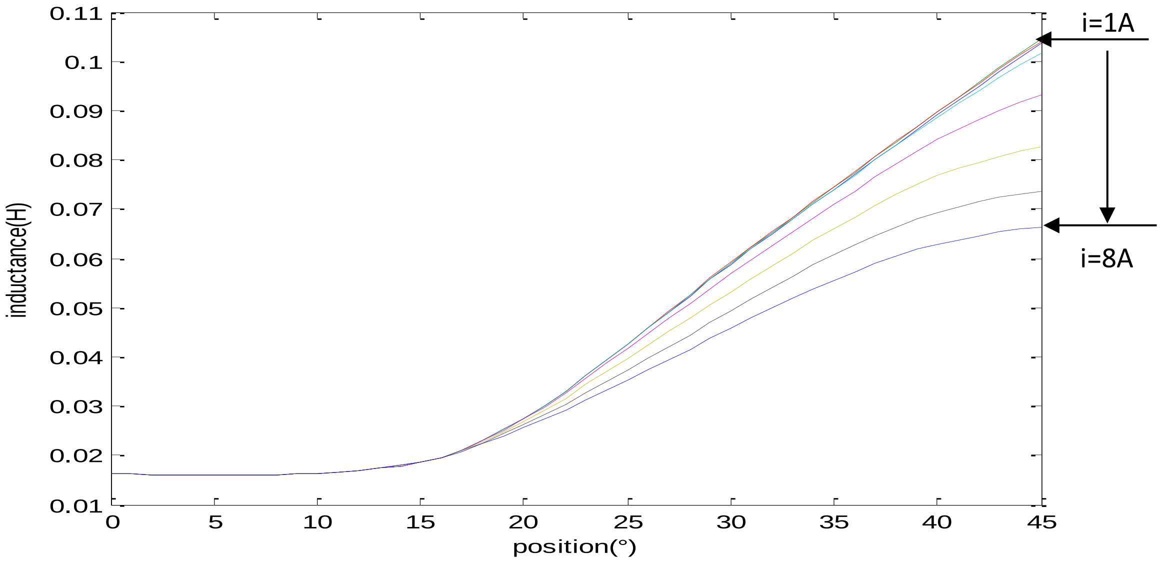

Figure II.14. Evolution of the inductance of a phase as a function of the rotor position for different excitation currents.

The inductance profile, denoted as L(θ, I), derived from finite element analysis is visually represented in Figure (II.14), showcasing a comprehensive overview across different values of phase current and rotor position. The graph vividly illustrates the dynamic nature of the inductance, with its minimal value occurring when the rotor and stator are in an unaligned position. In contrast, the inductance reaches its zenith in the aligned position, a configuration that facilitates the onset of the saturation regime.

Examining the inductance curve, it becomes evident that the relationship is non-linear, demonstrating that for elevated currents, significant saturation effects come into play. The non-linearity underscores the intricate interplay between phase current, rotor position, and saturation, influencing the overall inductance characteristics of the system.

Figure (II.14) unveils two axes of symmetry at θ = 0° and θ = +45°, corresponding to the unaligned and aligned positions, respectively. This symmetry highlights the balanced behavior observed at these critical rotor positions. The graphical representation enables a detailed analysis of how inductance varies across the rotor positions and current amplitudes, providing essential insights into the motor's operational dynamics. From this figure we have:

$$L_{min} = 16.4 \text{ mH} \quad \text{et} \quad L_{max} = 104.6 \text{ mH}$$

II.3.9. Calculation of instantaneous torque

Securing a positive torque essential for sustaining rotational motion hinges on the timely supply of phases, particularly as the tooth of the rotor approaches alignment with the tooth of the stator. This critical juncture, marked by the phase of the permeance's growth, plays a pivotal role in facilitating the generation of torque. It is during this phase that the magnetic coupling between the rotor and stator intensifies, leading to an increase in permeance.

Expanding on this concept, the term "permeance" refers to the measure of the ease with which magnetic flux passes through a magnetic circuit. As the rotor's tooth nears alignment with the stator's tooth, the permeance experiences a notable surge, amplifying the magnetic interaction between these components. This surge in permeance is crucial for fostering a positive torque, as the magnetic forces between the rotor and stator become optimized during this phase.

This phenomenon is particularly significant in the context of reluctance motors, where the variation in permeance directly influences the torque characteristics. Ensuring the timely supply of phases, synchronized with the strategic alignment of rotor and stator teeth, maximizes the potential for generating positive torque. This strategic coordination is fundamental for maintaining the continuous rotational movement of the motor.

In summary, the paragraph underscores the importance of phase supply during specific rotor-stator alignment phases, emphasizing the connection between torque generation and the growth of permeance. This understanding is fundamental for optimizing the operational efficiency and performance of reluctance motors in sustaining rotational motion.

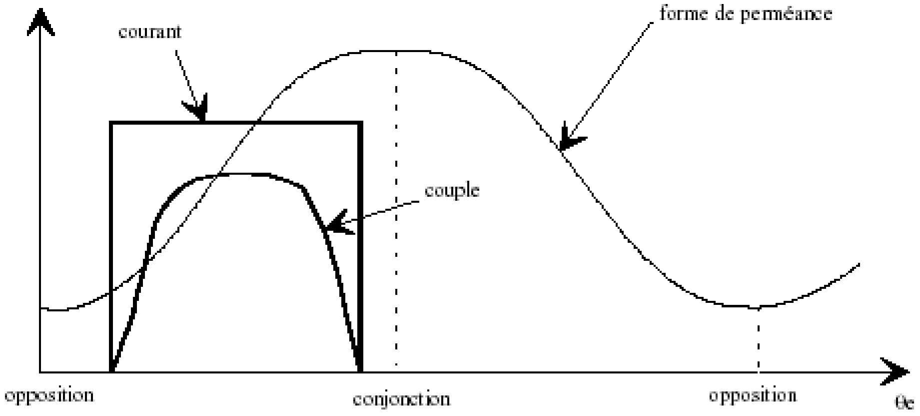

Figure II.15. Permanence, current, and torque depending on position.

Conversely, the power supply to the phase during the decrease in permeance generates a negative torque and, therefore, a braking operation of the SRM.

The energy variation method makes it possible to express the instantaneous torque of any electromagnetic machine:

$$c = -\frac{\partial W}{\partial \theta_m} = -N_r \frac{\partial W}{\partial \theta_e} \text{ with } \varphi = c^{te} \text{ (in engine agreement)} \tag{II.26}$$

Or:

$$c = -\frac{\partial \overline{W}}{\partial \theta_m} = -N_r \frac{\partial \overline{W}}{\partial \theta_e} \text{ with n.i } = c^{te} \tag{II.27}$$

where the energy W and the co-energy $\overline{W}$ are written:

$$W = \int_0^{\phi_0} ni.d\phi \tag{II.28}$$

And

$$\overline{W} = \int_0^{ni} \phi.dni \tag{II.29}$$

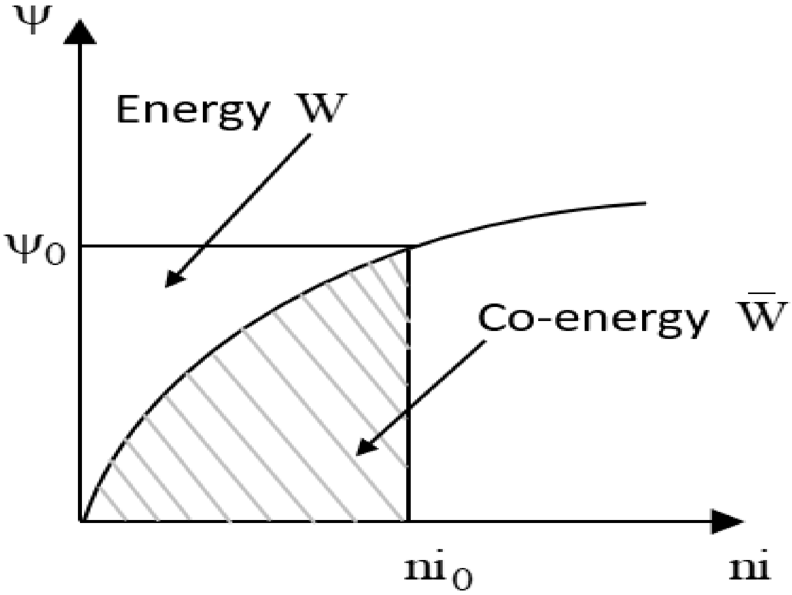

Figure II.16. Representation of energy and co-energy.

In a linear regime, the flux is linked to the ampere-turns (ni) by the permeance P(θ):

$$\varphi(\theta) = P(\theta).ni \tag{II.30}$$

So :

$$W = \int_0^{ni} P(\theta).ni.d\,ni = \frac{1}{2}.P(\theta).ni^2 \tag{II.31}$$

Which allows the torque to be expressed by:

$$C_e = \frac{N_r}{2}.ni^2.\frac{d(P)}{d\theta} \tag{II.32}$$

Or concerning the phase inductance L(θ):

$$C_e = \frac{N_r}{2}.i^2.\frac{d(n^2P)}{d\theta} = C_e = \frac{N_r}{2}.i^2.\frac{d(L)}{d\theta} \tag{II.33}$$

In the same way, if we impose the flux, we obtain from the expression of the magnetic energy the couple:

$$C_e = -\frac{N_r}{2}.n^2.\phi^2.\frac{d(R)}{d\theta} \tag{II.34}$$

Where R(θ): is the reluctance.

Upon examination of equation (II.33), it becomes apparent that the sign of the torque remains independent of the current's direction. This observation implies that a unidirectional current converter can effectively power our machine. In other words, the torque generation in the system is not contingent on the polarity of the current, allowing for the simplification of the power supply apparatus by employing a unidirectional current source. This inherent property streamlines the design and implementation of the power system for the machine, offering practical advantages in terms of simplicity and efficiency in driving the Switched Reluctance Motor (SRM).

When the machine is saturated, the phase inductance does not vary with position. It is then necessary to calculate the torque from the energy converted during a power cycle.

The converted electromagnetic power Pe is then expressed by:

$$P_e = f.W \tag{II.35}$$

With:

f: the electrical supply frequency, which can be written from the rotational pulsation of the motor Ω:

$$f = N_r.\frac{\Omega}{2\pi} \tag{II.36}$$

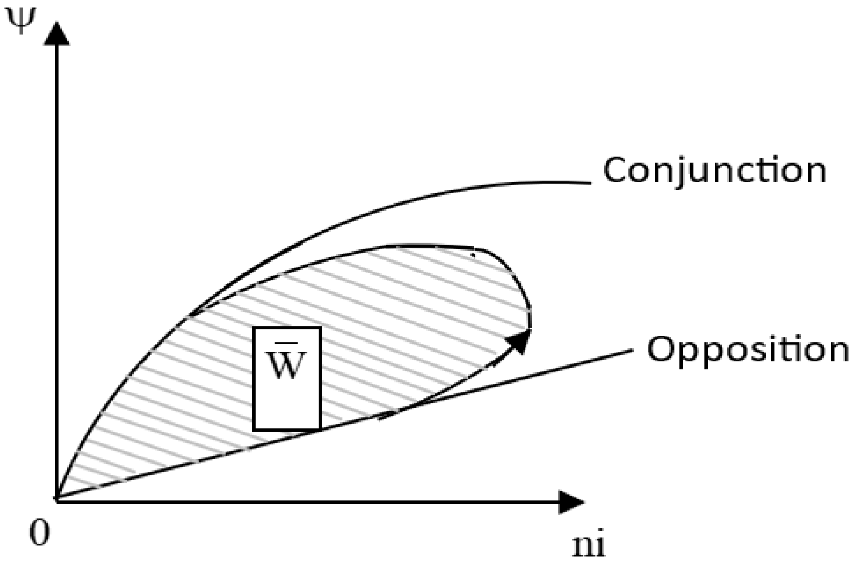

Figure II.17. Representation of co-energy.

Thus, the electromagnetic torque is valid if the motor has q phases:

$$Ce = \frac{q.Pe}{\Omega} = q.N_r.\frac{W}{2\pi} \tag{II.37}$$

Conclusion

The modelling of the Switched Reluctance Motor (SRM) is conducted through the Finite Element Method Magnetics (FEMM) software. FEMM employs the finite element method to numerically solve Maxwell's equations, enabling the determination of electromagnetic characteristics in the static regime based on specified dimensions. The outcomes of this simulation yield crucial insights into the inductance profile, static torque, and flux distribution within the SRM.

These obtained results serve as foundational data, integrating seamlessly with the electrical and mechanical equations governing the SRM. The intention is to leverage this data to construct a dynamic simulation model, a process detailed in the subsequent chapter. The dynamic simulation model considers two scenarios: firstly, an assumed linear model, followed by a more intricate nonlinear model. This comprehensive simulation approach aims to capture the dynamic behaviour of the SRM under varying operational conditions, providing a holistic understanding of its performance characteristics and facilitating the development of effective control strategies.

Introduction

Modeling is a crucial aspect for engineers and researchers, providing the means to anticipate, scrutinise, and regulate the dynamic behavior of Switched Reluctance Motors (SRMs), thereby constituting an indispensable stage in the design and development process. Within a specific training framework, any enhancement in performance necessitates intervention in one of the three fundamental elements: the motor itself, the power supply, or the employed control strategies. The power supply's role is to sequentially apply voltage to the terminals of the motor's various phases, ensuring the activation of a specific winding upon command while also facilitating a controlled power cutoff. This chapter focuses on simulating the variable reluctance machine, delving into the study of its dynamic behavior initially in a linear regime and subsequently in a nonlinear regime, employing diverse control strategies.

III.1. Electromagnetic equations

The instantaneous voltage applied to the winding of a phase of the SRM motor has a relationship with the flux by Faraday's law:

$$V_S = Ri + \frac{d\psi}{dt} \tag{III.1}$$

"V_S" denotes the applied voltage, representing the external electrical potential applied to the system. The variable "i" signifies the current flowing through the phase. "R" corresponds to the resistance of the phase winding. Lastly, the symbol "Ψ" represents the flux, a measure of the magnetic field intensity within the system.

Owing to the distinctive dual saliency structure inherent in the switched reluctance motor (SRM) and the influence of magnetic saturation, the flux within an SRM phase exhibits variability contingent upon both the rotor position (θ) and the magnitude of the phase current. To account for these dynamic factors, Equation (III-1) is subject to expansion, as detailed below:

$$Vs = Ri + \frac{d\psi}{di}\frac{di}{dt} + \frac{d\psi}{d\theta}\frac{d\theta}{dt} \tag{III.2}$$

$\frac{\partial \Psi}{\partial i}$ is defined as the instantaneous inductance L(θ,I) and the term $\frac{\partial \Psi}{\partial \theta}\frac{\partial \theta}{\partial t}$ is the instantaneous FCEM.

III.2. Torque production

The characterization of the switched reluctance motor (SRM) involves a convex function defined by the position of the rotor (θ) and the current in the nth phase. This function is denoted as the co-energy (ψ, θ). Likewise, the energy function W(ψ, θ), incorporating variables such as the n-phase fluxes and rotor position, provides a comprehensive description of the SRM. When considering the vectors ψ and I, the co-energy and energy functions satisfy the following inequality:

$$\bar{W}(I,\theta) + W(\Psi,\theta) \geq \Psi^t I \quad \text{(III.3)}$$

The SRM, endowed with its dual saliency, exhibits the capability for magnetic energy variation, leading to the generation of torque. The torque of the machine is determined by taking the partial derivative of the energy function with respect to the position of the rotor:

$$C_e(\Psi_1,\ldots,\Psi_n,\theta) = \frac{\partial W}{\partial \theta}(\Psi_1,\ldots,\Psi_n,\theta) \quad \text{(III.4)}$$

Utilizing this connection in the context of a 6/4 Switched Reluctance Motor (SRM), the resulting relationship is:

$$C_e(\Psi_1,\Psi_2,\Psi_3,\theta) = \frac{\partial W}{\partial \theta}(\Psi_1,\Psi_2,\Psi_3,\theta) \quad \text{(III.5)}$$

Upon exciting a particular phase, torque manifests itself, causing the rotor to progress in the direction of increasing inductance. Consequently, the torque aligns itself with the closest aligned position.

III.3. Linear Model of SRM

The electromagnetic properties employed for simulating the 6/4 Switched Reluctance Motor (SRM) were acquired through finite element analysis in Chapter II. Figure (III.1) illustrates the linear inductance profile, represented as L(θ), wherein each phase inductance is offset by an angle θs.

$$\theta_s = 2\pi\left(\frac{1}{N_r} - \frac{1}{N_s}\right) \quad \text{(III.6)}$$

Nr and Ns denote the number of poles for the rotor and stator, respectively. In cases where the arcs of the rotor and stator poles in the motor are not equal, represented by $\beta_r \neq \beta_s$, the following angle relationships are observed:

$$\theta_x = \left(\frac{\pi}{N_r}\right) - \frac{(\beta_r + \beta_s)}{2} \quad \text{(III.7)}$$

$$\theta_y = \left(\frac{\pi}{N_r}\right) - \frac{(\beta_r - \beta_s)}{2} \tag{III.8}$$

$$\theta_z = \frac{(\beta_r - \beta_s)}{2} \tag{III.9}$$

$$\theta_z = (\theta_y + \theta_z + \theta_s) \tag{III.10}$$

These indications are illustrated in Figure (III.1). Figure (III.2) depicts the angle δ associated with the displacement of one phase about another, as given by:

$$\delta = 2\Pi\left(\frac{1}{N_r} - \frac{1}{N_s}\right) \tag{III.11}$$

The electrical equation governing each phase is expressed as follows:

$$V_i = Ri_i + \frac{d\psi_i(\theta, i_i)}{dt}, \quad \mathrm{i} = \{1,2,3\} \tag{III.12}$$

The flow in each phase is defined by the linear equation:

$$\Psi_i(\theta, i_i) = L(\theta)i_i \tag{III.13}$$

The cumulative energy attributed to all three phases is represented by:

$$W_{total} = \frac{1}{2}\sum_{i=1}^{3} L(\theta + (n - i - 1)\theta_s)\, i_i^2 \tag{III.14}$$

The overall torque generated by the motor is captured by the equation:

$$C_e = \frac{1}{2}\sum_{i=1}^{3} \frac{L(\theta + (n-i-1)\theta_s)}{d\theta}\, i_i^2 \tag{III.15}$$

The mechanical aspects are encapsulated by the following equations:

$$J\frac{d\omega}{dt} = C_e - C_r - F\omega \tag{III.16}$$

$$\frac{d\theta}{dt} = \omega \tag{III.17}$$

C_r : represents the load torque.

F : The coefficient of friction of the machine.

J : Moment of inertia.

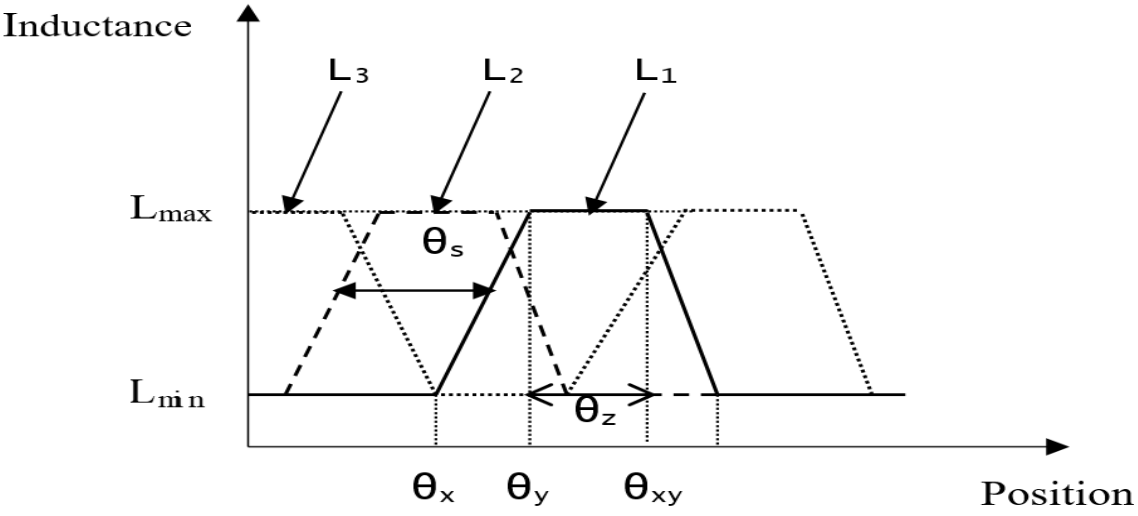

Figure III.1. Inductance as a function of position.

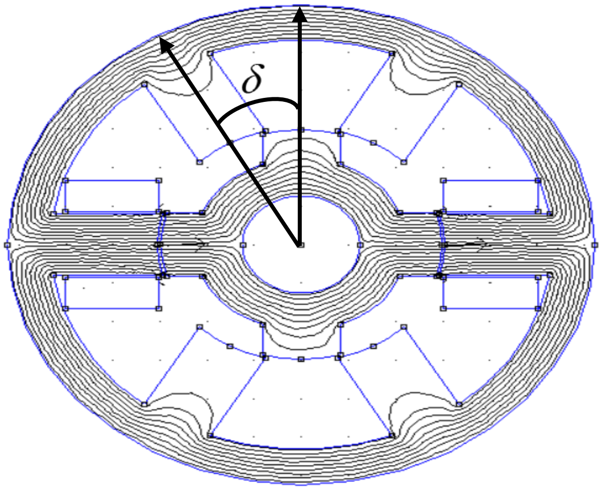

Figure III.2. The δ angle corresponds to the displacement of one phase relative to another.

Figure (III.3) presents the simulation diagram utilized for the linear model of the Switched Reluctance Motor (SRM). Meanwhile, Figure (III.4) details the components within the phase 1 block. This block encompasses three additional blocks, each corresponding to a distinct MATLAB function.

These components include:

The Converter: Responsible for facilitating the switching of the power converter at specific angles, namely θon, θoff, and θd.

Inductance: Computes the current flowing through the inductance of each phase, contingent upon the rotor position (θ) and the phase flux (ψ). The output of this calculation represents the current in Phase 1.

Torque: Determines the torque generated in the respective phase based on the rotor position (θ) and the current value (I).

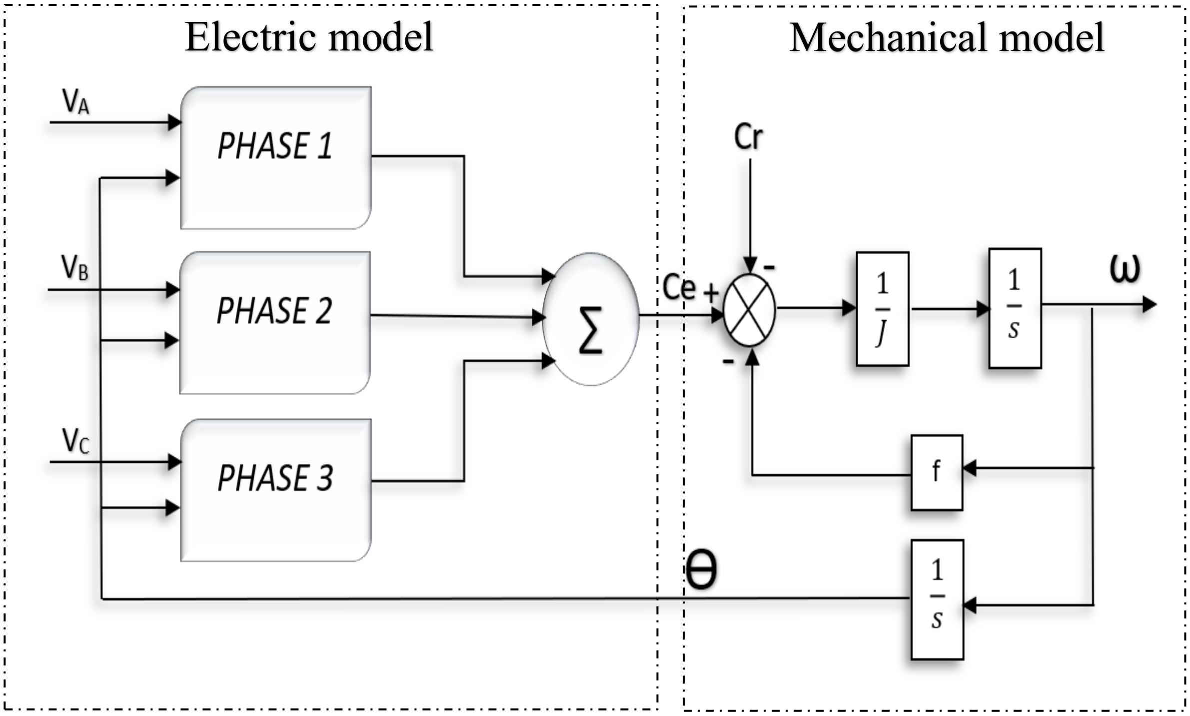

Figure III.3. SRM simulation diagram.

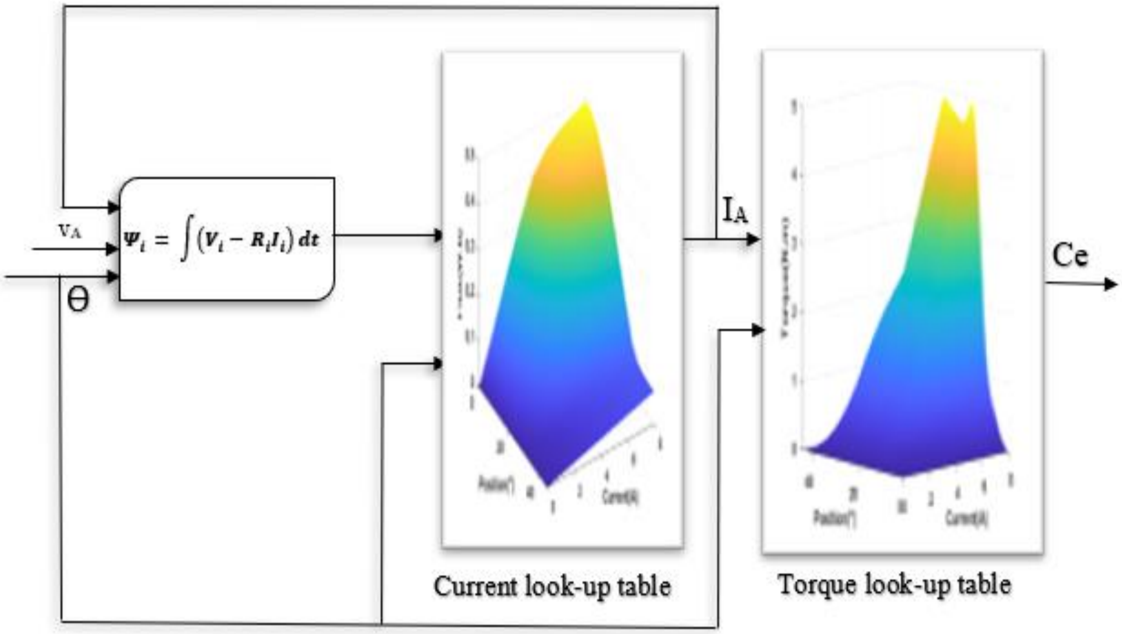

Figure III.4. SRM simulation diagram by phase (linear model).

Initiating the simulation of the Switched Reluctance Motor (SRM) using its linear model requires careful consideration in selecting an initial rotor position outside the zone where the inductance (L) maintains a constant value, thereby preventing torque production. In instances where the load torque is zero, the rotor position (θ) remains unchanged, resulting in the machine being stationary. However, under non-zero load torque conditions, the rotor adjusts to attain a speed where the resistive torque (Cr) equals the electromagnetic torque (Ce). For our specific machine, an initial angle (θ) exceeding 15° was chosen, as evident from its inductance profile in Figure (III.2), to circumvent the scenario of zero load torque in the initial stages.

III.4. SRM control strategies

There are various configurations for controlling a switched-reluctance motor with a static converter. These control structures can be distinguished by the number of semiconductors and passive components, as well as the number of phases and the connection of the stator coils. The single-ended H-bridge converter, shown in Figure III.5, offers maximum control and flexibility. Each phase has two IGBTs and two diodes, similar to a converter in a synchronous machine. However, the structure is completely different, and it is not possible to short-circuit the source due to the resistance of the coils limiting the current.

Key features of this configuration include:

- Semiconductors: The number of semiconductors is similar to that of a converter in a synchronous machine, but the structure is different.
- Phases: The number of phases depends on the specific configuration, with common configurations being 6/4 three-phase and 8/6 four-phase SRMs.
- Stator Coils: The stator coils are connected in a specific manner, which determines the motor's operation and control requirements.
- Control Flexibility: The single-ended H-bridge converter offers maximum control and flexibility, allowing for precise control of the motor's speed and torque.
- Short-Circuit Protection: The resistance of the coils limits the current, preventing short-circuit conditions in the motor.

Since we are in a linear regime, the flux relation is given by:

$$\Psi = L(\theta)i \qquad \text{(III.18)}$$

The Co Energy :

$$\overline{W} = \frac{1}{2}L(\theta)i^2 \qquad \text{(III.19)}$$

The torque is given by:

$$C_e = \frac{1}{2}\frac{dL}{d\theta}i^2 \qquad \text{(III.20)}$$

Expression (III-20) shows that this converter is unidirectional in current because the production of torque does not depend on the sign of current but only on the sign of $\frac{dL}{d\theta}$.

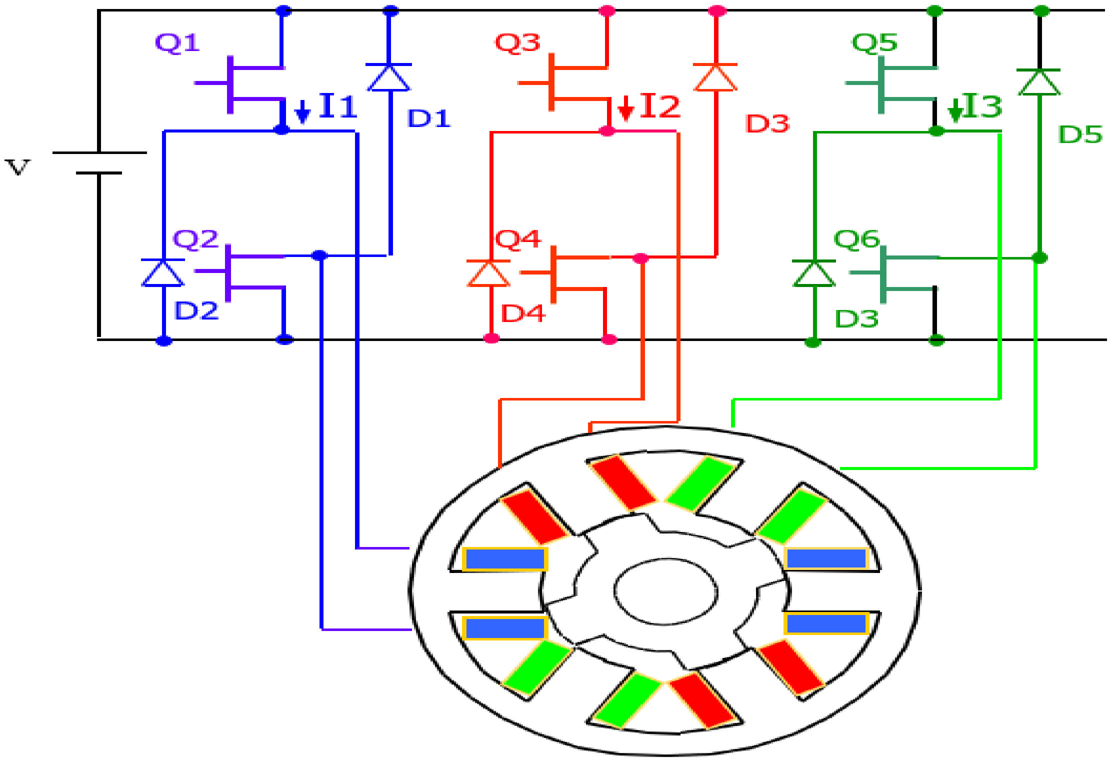

Figure III.5. Half bridge converter.

III.4.1. Current control

Hysteresis current control is a widespread technique used in the control of switched reluctance motors (SRMs), which are known for their simple construction and robustness but can be challenging to control due to their nonlinear characteristics. This control strategy aims to address these challenges by measuring the current flowing through the motor phases, typically using current sensors, and comparing it with a reference current. Based on the comparison results from the hysteresis comparator, a switching logic determines whether to increase, decrease, or maintain the current in each phase. H-bridge converters are then controlled to either connect or disconnect the phases from the power supply based on the switching logic. In Figure III.6, the current control block diagram is depicted, offering a visual representation of the control system. This diagram captures the dynamic behavior of the Switched Reluctance Motor (SRM), specifically when employing hysteresis current control. The outcomes portrayed in Figure III.7 were derived under specific conditions: θon = 0°, θoff = 30°, and a reference current (Iref) set at 6A. Notably, these results were obtained while the motor was operating under no-load conditions. The set of results presented in Figure III.8 pertains to the second group, where a notable alteration involves an increase in the angle θ_off, now adjusted to 38°. This adjustment in θ_off has a direct impact on the observed outcomes, signifying a variation in the experimental conditions and offering insight into the system's response under these modified parameters.[63-65]

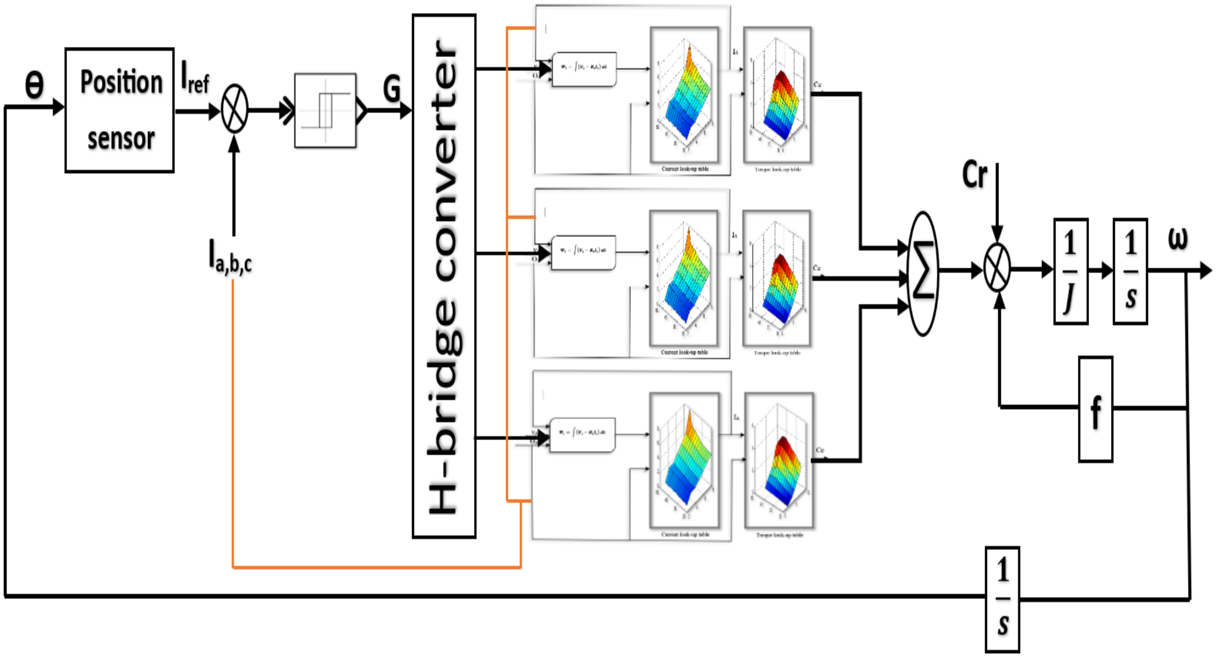

Figure III.6. schema of Current control for switched reluctance motor 6/4..

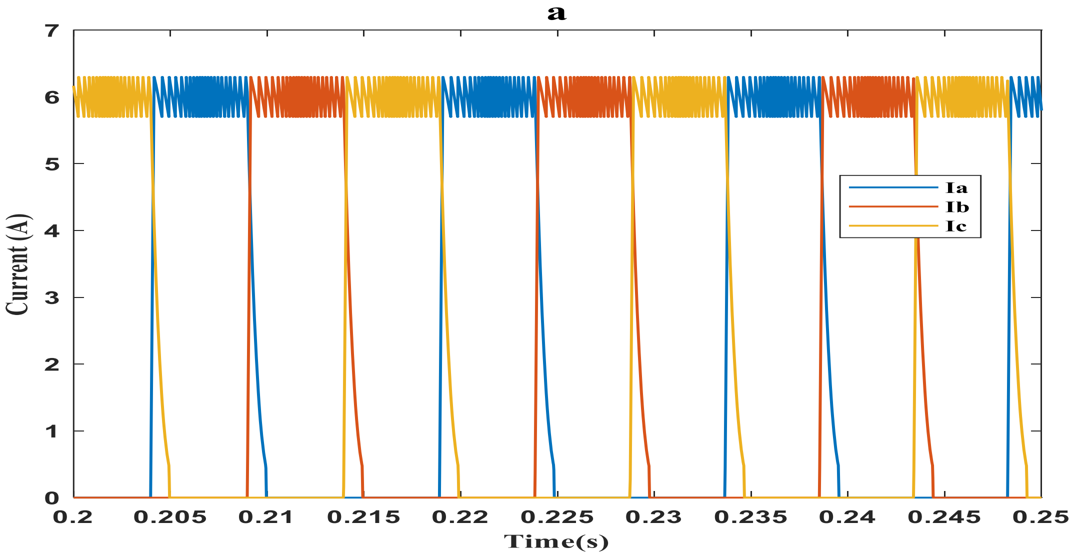

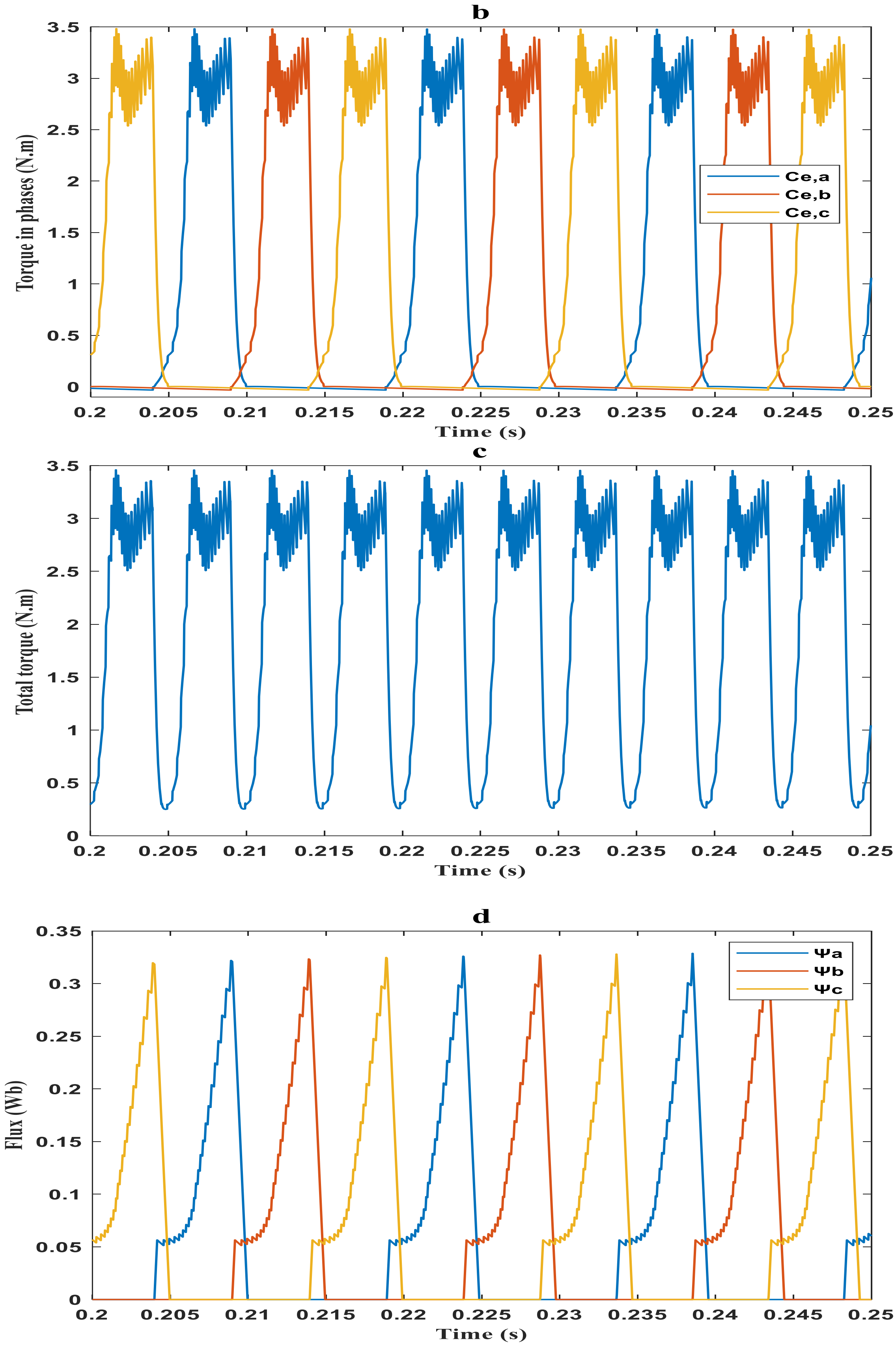
b
Torque in phases (N.m)
3.5
3
2.5
2
1.5
1
0.5
0
Ce,a
Ce,b
Ce,c
0.2
0.205
0.21
0.215
0.22
0.225
0.23
0.235
0.24
0.245
0.25
Time (s)
c
Total torque (N.m)
3.5
3
2.5
2
1.5
1
0.5
0
0.2
0.205
0.21
0.215
0.22
0.225
0.23
0.235
0.24
0.245
0.25
Time (s)
d
Flux (Wb)
0.35
0.3
0.25
0.2
0.15
0.1
0.05
0
Ψa
Ψb
Ψc
0.2
0.205
0.21
0.215
0.22
0.225
0.23
0.235
0.24
0.245
0.25
Time (s)

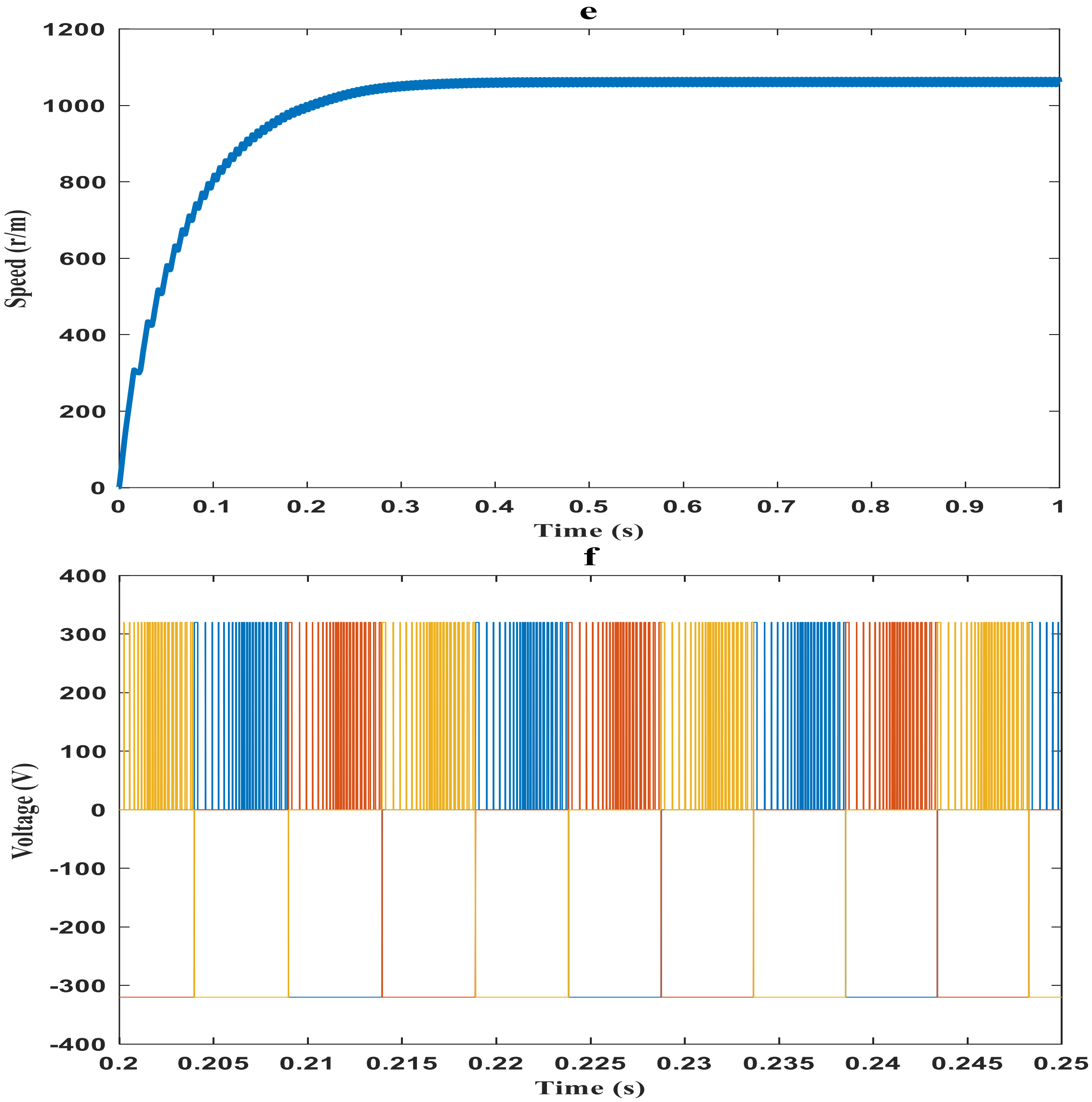

Figure III.7. Simulation results utilizing θon = 0° and θoff = 30°, with the SRM working without charge applied (a: Current, b: Torque in phases, c: Total Torque, d: Flux, e: Speed, and f: Voltage).

The results, depicted in Figure III.7, showcase the impact of hysteresis current regulation under specific conditions: a reference current (Iref) of 6 A, absence of torque charge, and angular parameters set at θon = 0° and θoff = 30°. The influence of hysteresis current control on the current waveform is elucidated in Figure III.7(a), while Figure III.7(b) illustrates the corresponding torque in phases. Furthermore, Figure III.7(c) provides insight into the cumulative effect of hysteresis current regulation on the total torque. Additionally, Figure III.7(d) represents the flux for θoff = 30°, with its characteristics influenced by the velocity of oscillation, as depicted in Figure III.7(e). Lastly, Figure III.7(f) offers a visualization of the voltage applied to the switched reluctance motor, providing a comprehensive view of the system's behavior under the specified conditions.

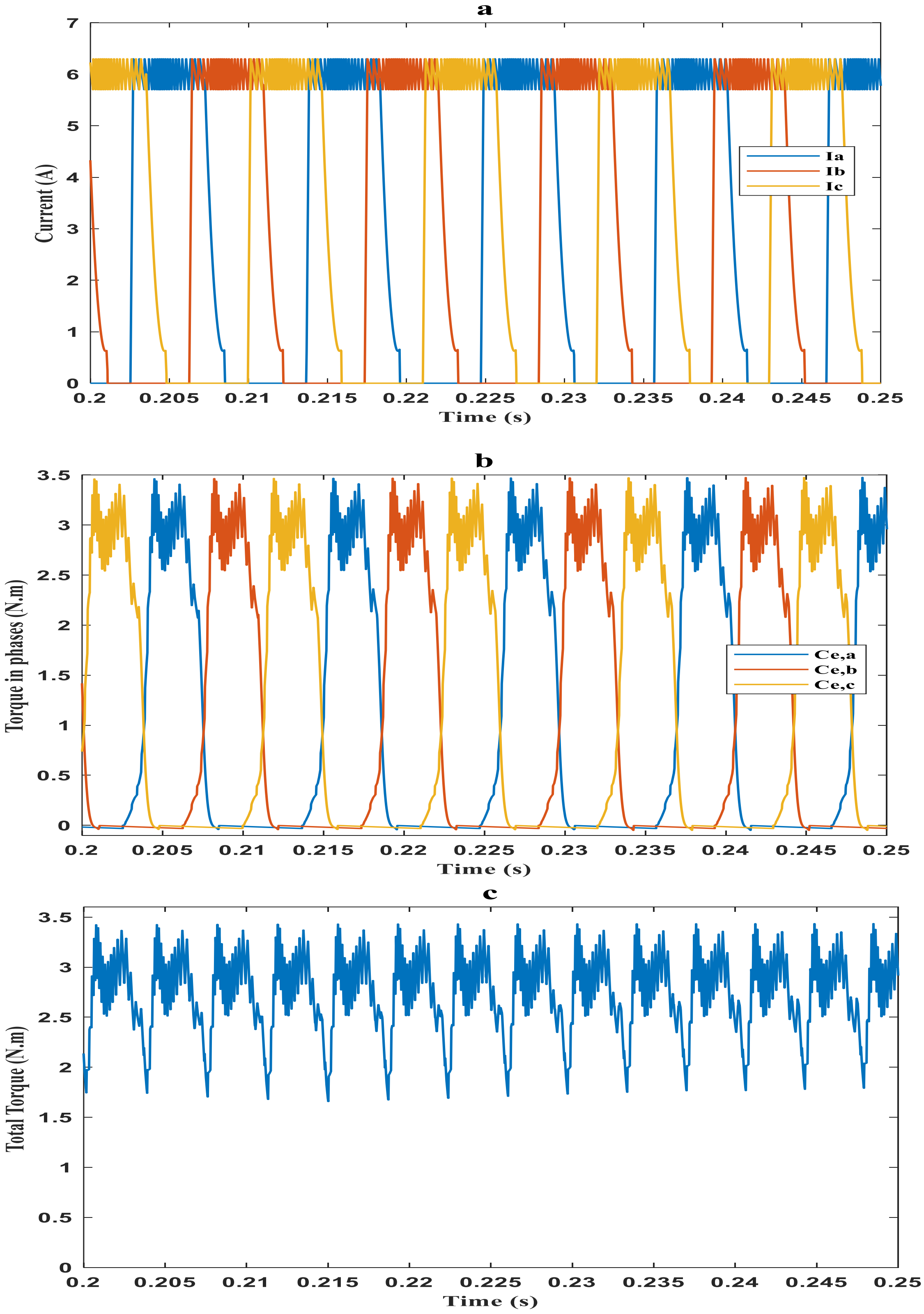

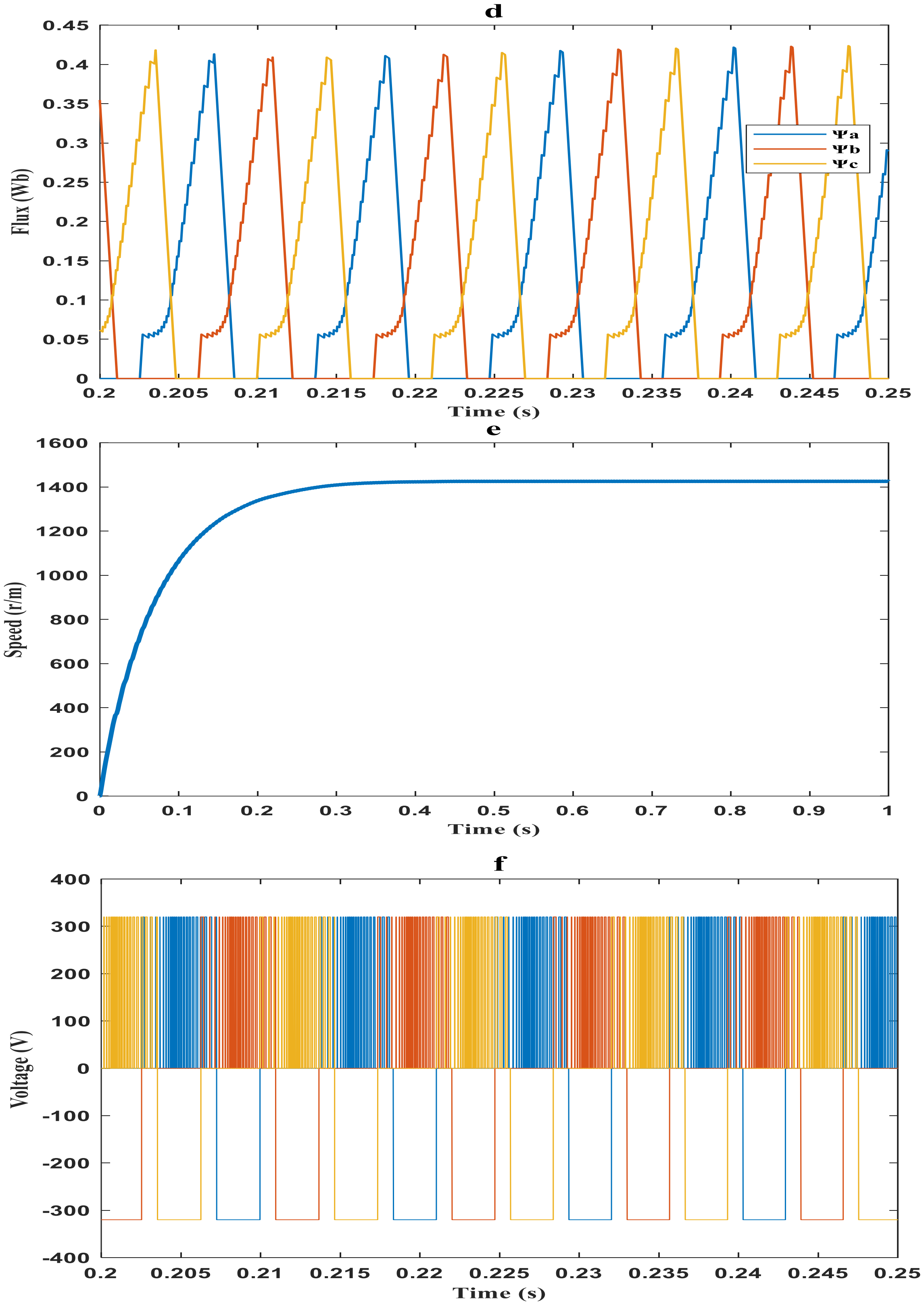

Figure III.8. Simulation results utilizing θon = 0° and θoff = 30°, with the SRM working without charge applied (a: Current, b: Torque in phases, c: Total Torque, d: Flux, e: Speed, and f: Voltage).

To mitigate speed oscillations, it was imperative to enhance torque production. Consequently, we fine-tuned the angle θoff, adjusting it from 30° to 38°. The updated dynamics of the Switched Reluctance Motor (SRM) are illustrated in Figure III.8 for θon = 0° and θoff = 38°, with Iref set at 6A, while the machine continues to operate without a load. Figure (III.8.a) delineates the current waveform in a single phase. In Figure (III.8.b), it is observed that the revised θoff value still results in the presence of phase current in the region where the inductance of the phase is decreasing, accompanied by the emergence of negative torque. Figure (III.8.c) demonstrates a reduction in torque ripple following the adjustment of the angle θoff. Consequently, the machine speed exhibits fewer oscillations, as depicted in Figure (III.8.e). Nevertheless, minimizing ripple proves to be a challenging task, given the influence of other parameters such as motor speed and load values on the magnitude of torque ripple.

III.4.2. Direct Torque Control DTC

In this section, we unveil a method for the direct control of torque and flux in the switched reluctance motor (SRM), offering a substantial reduction in torque ripples and a significant enhancement in performance.[66]. This control strategy hinges on the direct determination of the command sequence applied to the switches of a half-bridge converter.[68-70]. The decision-making process predominantly relies on the utilization of hysteresis regulators, serving to regulate the system's state, encompassing the amplitude of the stator flux and the electromagnetic torque. The schematic for direct torque and flux control is depicted in Figure 9.[71-73]

The fundamental approach to inverter regulation involves direct control through sequential applications during the inverter control period (Te) using non-zero vectors (VK) and null vectors (V0 and V7). This enables the selection of appropriate voltage vectors, directing the stator flux along a predetermined trajectory. The objective of flux control is to maintain the constant modulus of the latter. Ideally, this is achieved by trapping its reference trajectory within two concentric circles of extremely close radius. The width (s) of this circular ring is contingent on the switching frequency of the inverter switches; a higher frequency results in a narrower band. The role of the hysteresis comparator is to confine the end of the total torque vector within a circular crown. This comparison is straightforward to implement, and the total torque is the summation of the torque from the phases of the SRM. This complexity arises from multiple phases contributing to electromagnetic torque, with the signal generator determining the active phases based on the rotor's position.

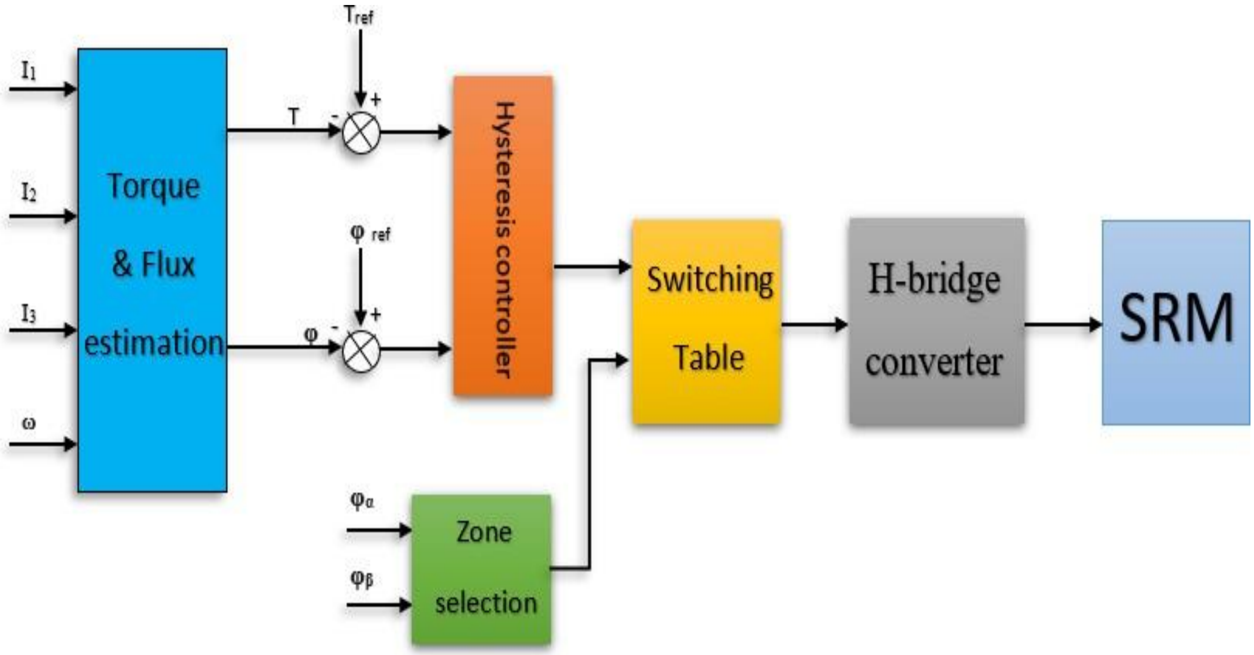

Figure III.9. Schematic for direct torque and flux control DTC.

In switched reluctance motor (SRM) systems, the asymmetric half-bridge circuit is a prevalent choice for power conversion, providing a straightforward control mechanism and phase independence. The selection of the appropriate voltage vector is crucial in determining the flux module's development direction. To achieve robust dynamic performance, a two-level hysteresis corrector is commonly employed. This corrector directly assesses whether the flux amplitude requires an elevation or reduction.

Moreover, the utilization of a three-level hysteresis corrector extends the control capability of the SRM to both directions of rotation. This advanced corrector indicates whether the torque amplitude should be increased or decreased, catering to positive or negative setpoints. The decision-making process is based on the correction of torque-related parameters. The ensuing table delineates the voltage vector choices and the corresponding control sector, providing a comprehensive guide for effective SRM control in diverse operational scenarios.

section	**dCe=1, $d\psi$=1**	**dCe=1, $d\psi$=0**	**dCe=0, $d\psi$=1**	**dCe=0, $d\psi$=0**	**dCe=-1, $d\psi$=1**	**dCe=-1, $d\psi$=0**
S1	**V2**	**V3**	**V7**	**V0**	**V6**	**V5**
S2	**V3**	**V4**	**V0**	**V7**	**V1**	**V6**
S3	**V4**	**V5**	**V7**	**V0**	**V2**	**V1**
S4	**V5**	**V6**	**V0**	**V7**	**V3**	**V2**
S5	**V6**	**V1**	**V7**	**V0**	**V4**	**V3**
S6	**V1**	**V2**	**V0**	**V7**	**V5**	**V4**

Table III.1. selection of vectors of control.

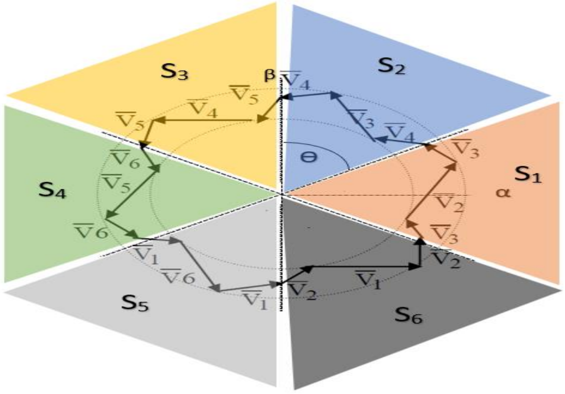

Figure III.10. organizational chart of the direct force and energy control DEFC.

This section presents the simulation results of Direct Torque Control (DTC), encompassing torque in individual phases, total torque, current, flux, and speed. The Switched Reluctance Motor (SRM) operates at a speed of 1600 rpm. At this speed, the total torque is initially recorded at 5 Nm. However, upon the introduction of a load to the SRM, the torque undergoes a notable shift, surging to 9 Nm. Simultaneously, the current experiences a sudden transition from 7 A to 12 A, while the flux fluctuates between 0.29 Wb and 0.32 Wb.

Remarkably, the speed manages to track the reference speed even in the presence of the added load. Nonetheless, the response time of the speed to attain the reference speed is characterized by a delayed reaction, and the system exhibits a considerable torque ripple under these conditions. These findings underscore the intricacies associated with achieving optimal control and performance in the SRM, particularly when subjected to variable loading conditions.

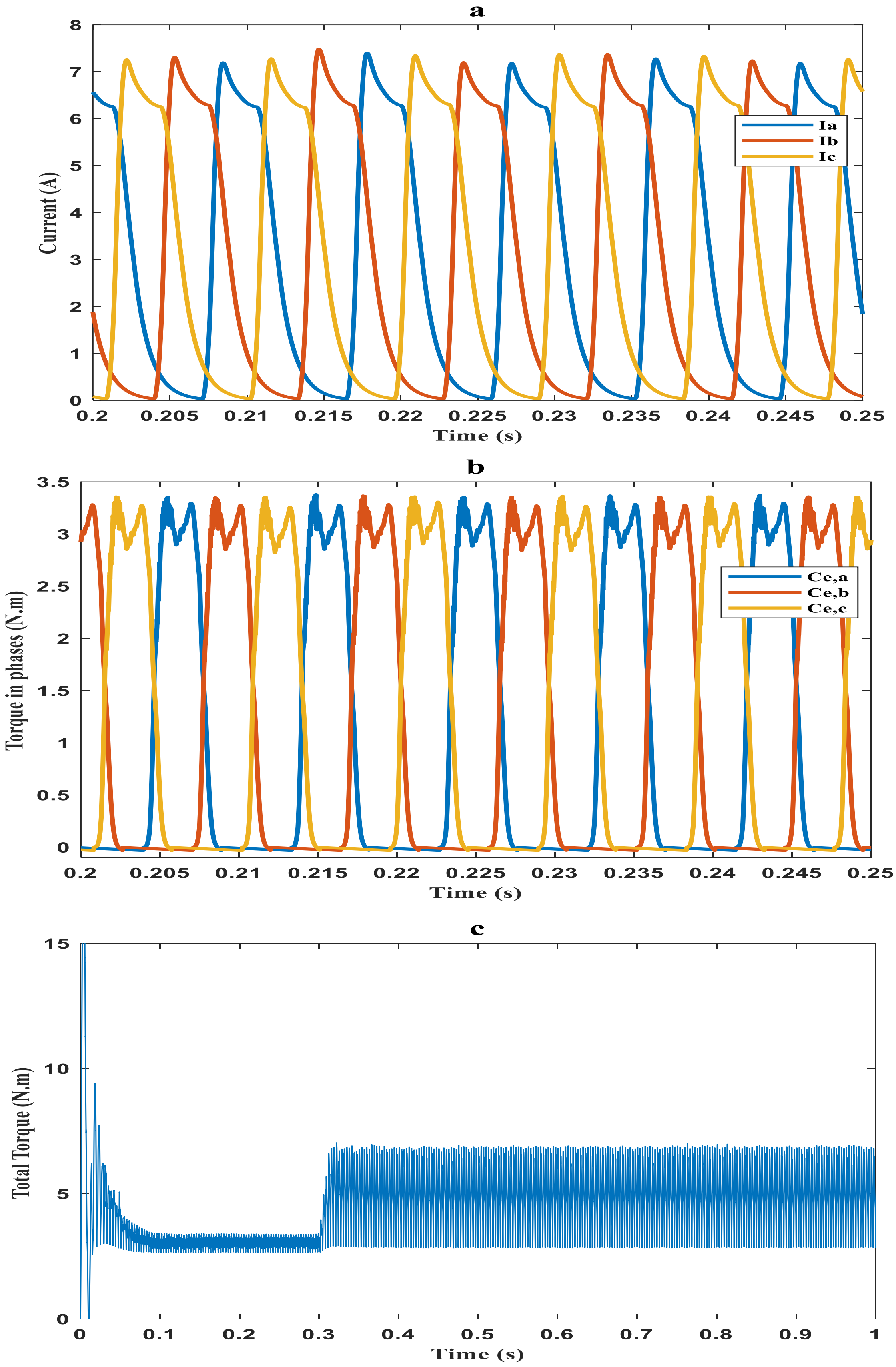
a
Current (A)
0
1
2
3
4
5
6
7
8
0.2
0.205
0.21
0.215
0.22
0.225
0.23
0.235
0.24
0.245
0.25
Time (s)
Ia
Ib
Ic
b
Torque in phases (N.m)
0
0.5
1
1.5
2
2.5
3
3.5
0.2
0.205
0.21
0.215
0.22
0.225
0.23
0.235
0.24
0.245
0.25
Time (s)
Ce,a
Ce,b
Ce,c
c
Total Torque (N.m)
0
5
10
15
0
0.1
0.2
0.3
0.4
0.5
0.6
0.7
0.8
0.9
1
Time (s)

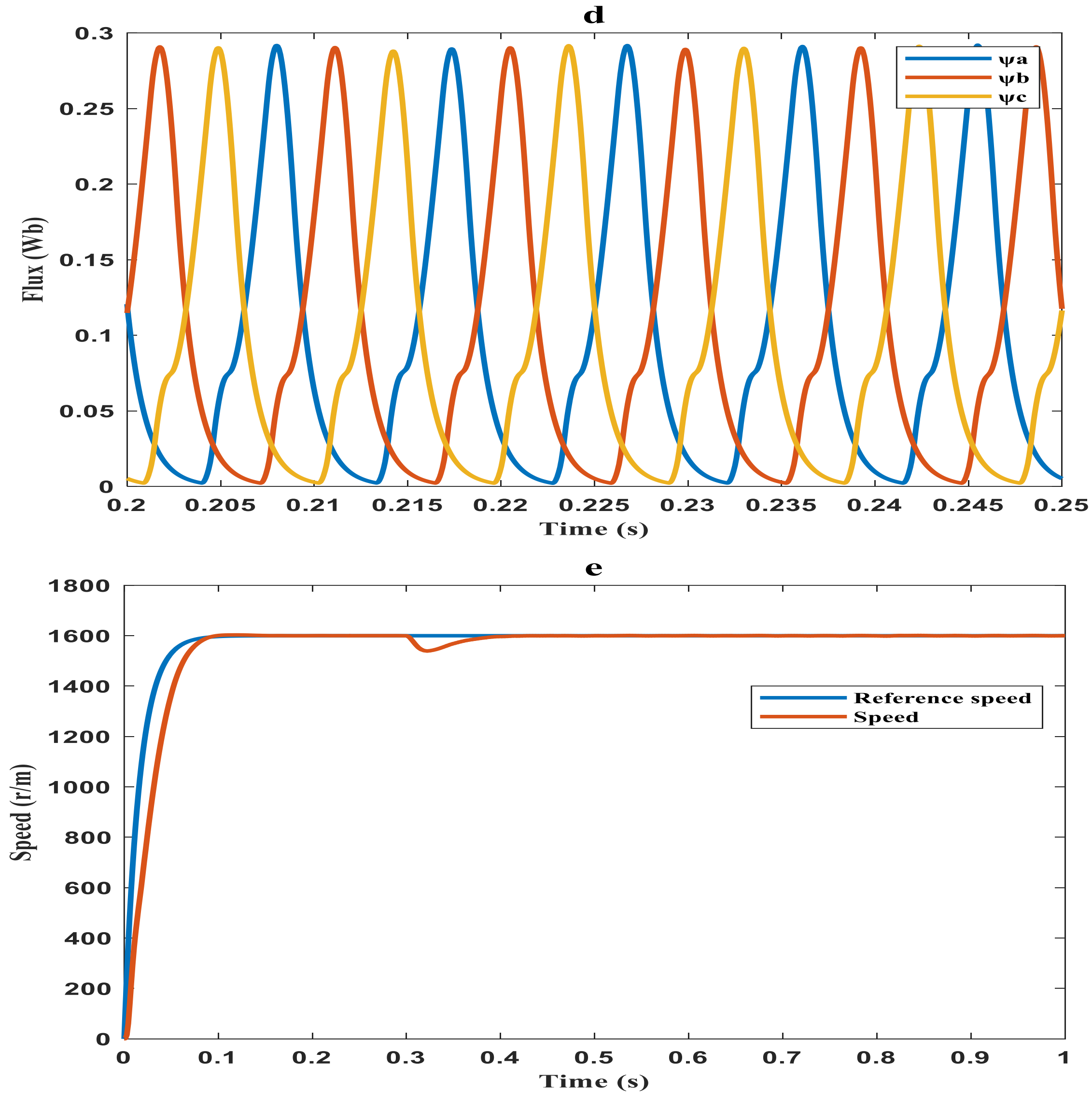

Figure III.11. Simulation results of Direct Torque Control with the SRM working with a charge applied 2 N.m (a: Current, b: Torque in phases, c: Total Torque, d: Flux, and e: Speed).

III.4.3. Direct Force Control DFC

The primary objective of the profession is to attain a specific reference trajectory through the control of direct force. The Direct Force Controller (DFC) is instrumental in achieving a consistent and smooth total radial force by overseeing the switches of the converter. This regulatory process is designed to reach a predefined value, Fref, representing the sum of radial forces (Fs) generated in the stator phases. The DFC, by maintaining a constant maximum value, effectively prevents mechanical excitation. To bridge the disparity between the required total radial force (Fref) and the actual sum of radial forces (Fs) in the phases, the DFC block generates switching signals for the power converter. The selected converter, featuring an asymmetric half-bridge topology, provides three alternative terminal voltages for the coupled phase winding. Figure III.12 illustrates a schematic representation of direct force control.

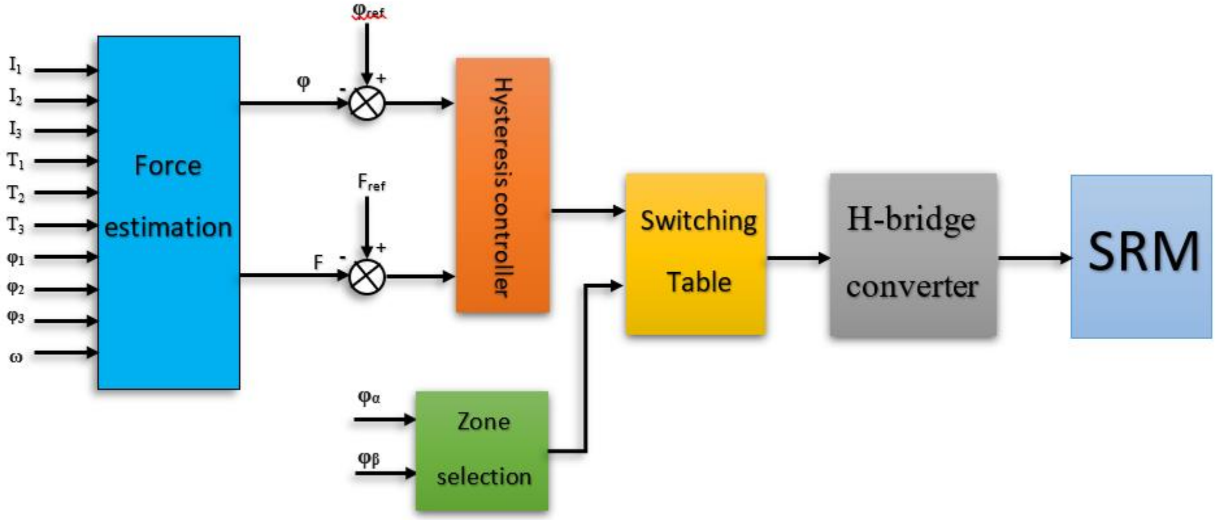

Figure III.12. Schematic for direct force control DFC.

The most straightforward method for inverter regulation involves direct control through the sequential application of non-zero voltage vectors VK, along with null vectors V0 and V7, throughout the inverter's control period Te. This approach facilitates the strategic selection of voltage vectors to guide the stator flux along a desired trajectory. The primary goal of flux control is to uphold a consistent flux magnitude. The preferred strategy involves confining the reference flux trajectory within two concentric circles of closely spaced radii. The width of this circular ring is contingent on the switching frequency of the inverter switches, with higher frequencies resulting in a narrower band. The hysteresis comparator plays a pivotal role in confining the resultant force vector within a circular boundary. This comparator, known for its ease of implementation, ensures that the cumulative force—comprising the forces of the Switched Reluctance Motor (SRM) phases—remains within the circular crown. The signal generator, driven by rotor position, determines the active phases. In SRMs, the asymmetric half-bridge circuit commonly serves as the power source for the converter, allowing for uncomplicated control and phase independence. To select the appropriate voltage vector, the corrector's output must specify the direction of flux development. This integrated approach ensures effective and controlled regulation of the inverter for optimized performance.[74-76]

section	**dF=1, dψ=1**	**dF=1, dψ=0**	**dF=0, dψ=1**	**dF=0, dψ=0**	**dF=1, dψ=1**	**dF=-1, dψ=0**
S1	**V2**	**V3**	**V7**	**V0**	**V6**	**V5**
S2	**V3**	**V4**	**V0**	**V7**	**V1**	**V6**
S3	**V4**	**V5**	**V7**	**V0**	**V2**	**V1**
S4	**V5**	**V6**	**V0**	**V7**	**V3**	**V2**
S5	**V6**	**V1**	**V7**	**V0**	**V4**	**V3**
S6	**V1**	**V2**	**V0**	**V7**	**V5**	**V4**

Table III.2. Selection of vectors of Direct Force control.

In the context of Direct Force Control (DFC), the total torque is initially measured at 5 Nm. Upon introducing a load to the Switched Reluctance Motor (SRM), the torque undergoes an increase, reaching 9 Nm, concomitant with a shift in current from 7.2 A to 11.8 A. The flux exhibits variations within the range of 0.29 Wb to 0.32 Wb. Similar to Direct Torque Control (DTC) , the speed maintains alignment with the reference speed despite the presence of a load. However, it's

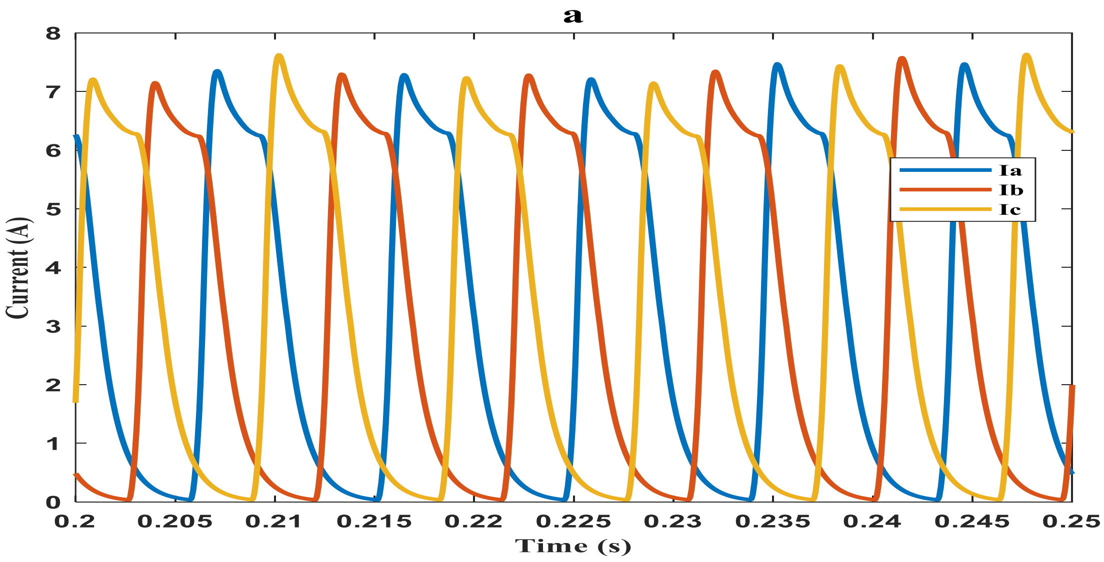

noteworthy that while the speed response is somewhat accelerated, it may not be the most efficient in promptly attaining the reference speed.

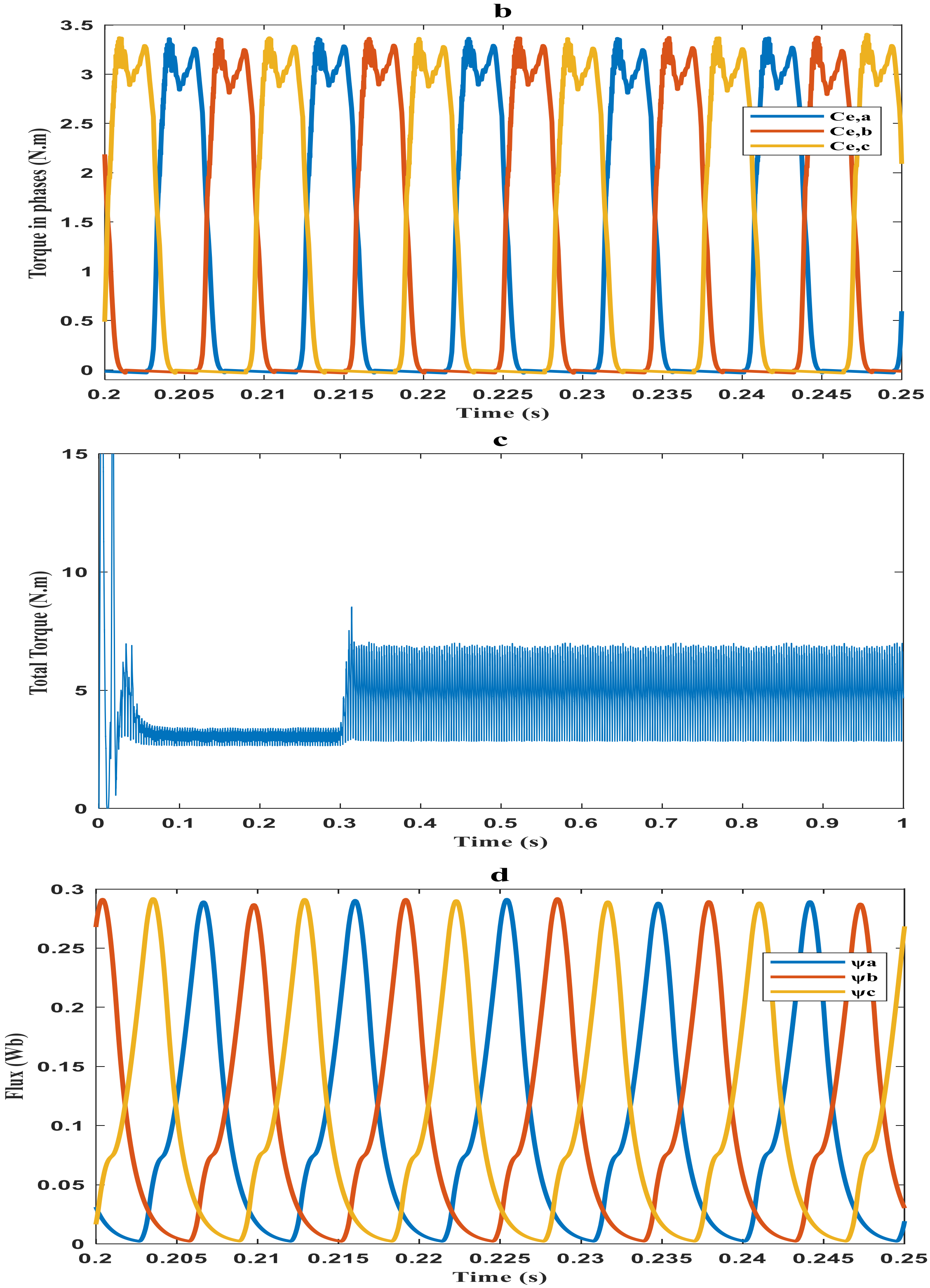

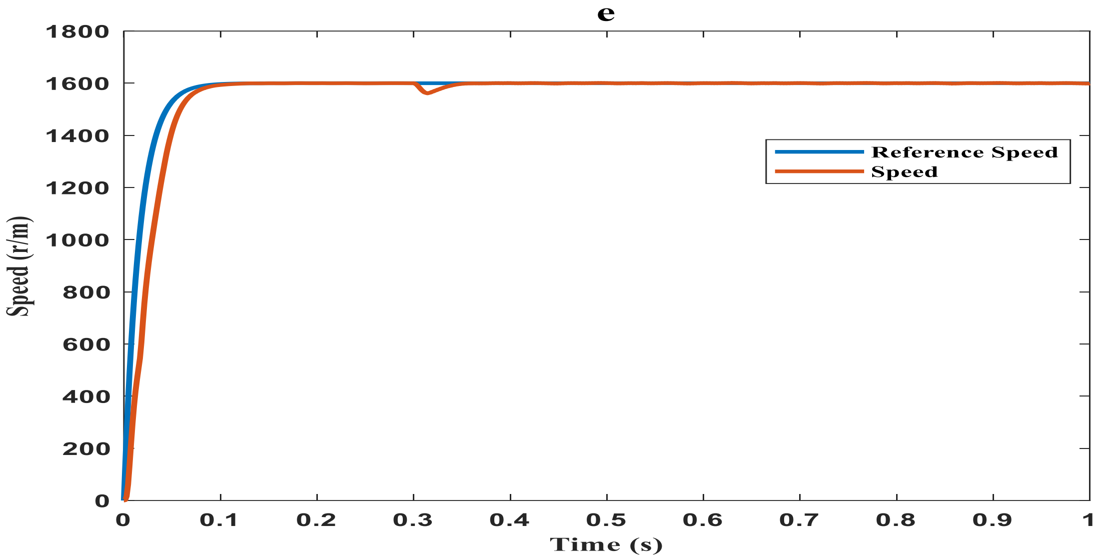

Figure III.13. Simulation results of Direct Force Control with the SRM working with a charge applied 2 N.m (a: Current, b: Torque in phases, c: Total Torque, d: Flux, and e: Speed).

III.4.4. Direct Energy Control DEC

In this section, we unveil the direct control mechanism governing the energy and torque of the Switched Reluctance (SR) motor. This approach brings about a noteworthy reduction in torque ripples, significantly elevating overall performance. The essence of this control version lies in the direct determination of the command sequence imparted to the switches of a half-bridge converter. Typically, this selection hinges on the utilization of hysteresis regulators, whose primary role is to govern the system's state, the energy amplitude, and the electromagnetic torque.[77]

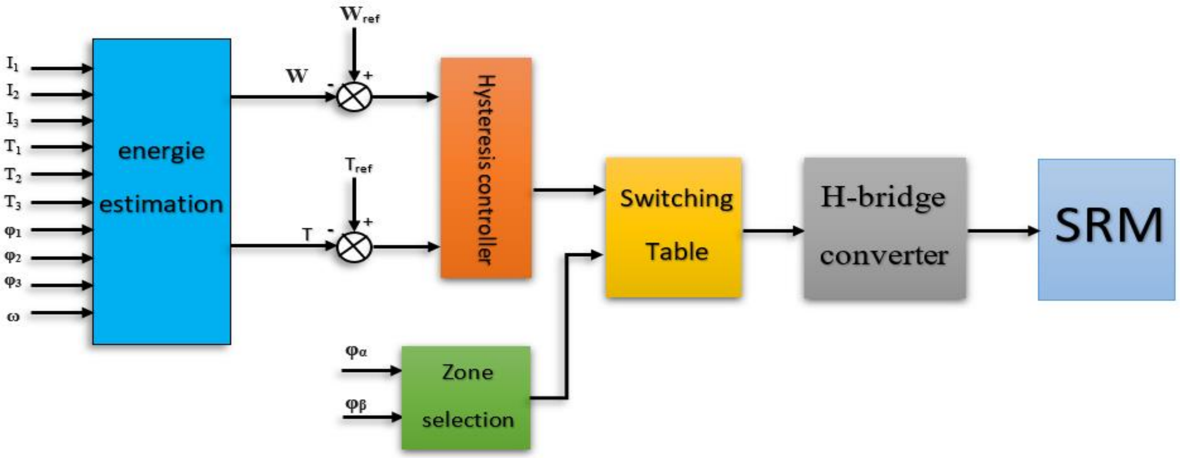

Figure III.14. Schematic for direct Energy control DEC.

The control process involves the sequential application of non-zero vectors VK, along with null vectors V0 and V7, to the inverter's control period Te. This allows for the strategic selection of appropriate voltage vectors to guide the energy along a predetermined trajectory. The objective of energy control is to maintain a constant modulus of the latter. A favourable approach is to confine its reference trajectory within two concentric circles of extremely close radius. The width 's' of this circular ring is contingent upon the switching frequency of the inverter switches, with a narrower band associated with higher frequencies.

The hysteresis comparator plays a crucial role in keeping the end of the total torque vector within a circular crown. This comparison is user-friendly, and it ensures effective control. On the flip side, the total torque represents the sum of the torque from the phases of the Switched Reluctance Motor (SRM). This complexity arises due to the presence of numerous phases contributing to electromagnetic torque. Consequently, the signal generator determines the active phases based on the rotor's position to effectively manage and control the overall system.

section	dCe=1, dW=1	dCe=1, dW=0	dCe=0, dW=1	dCe=0, dW=0	dCe=-1, dW=1	dCe=-1, dW=0
S1	V2	V3	V7	V0	V6	V5
S2	V3	V4	V0	V7	V1	V6
S3	V4	V5	V7	V0	V2	V1
S4	V5	V6	V0	V7	V3	V2
S5	V6	V1	V7	V0	V4	V3
S6	V1	V2	V0	V7	V5	V4

Table.III.3 Selection of vectors of Direct Energy control.

In the context of Direct Energy Control (DEC), prior to the introduction of the load, the current is recorded at 10A, and the flux stands at 0.42Wb. Upon adding the load, both the current and flux experience changes, reaching 21A and 0.45Wb, respectively. Simultaneously, the total torque undergoes a sudden shift from 4.5N.m. to 6.2N.m. Notably, the speed closely adheres to the reference speed even with the additional load. Although the speed response is somewhat accelerated, it may not be the most optimal for reaching the reference speed promptly. Nevertheless, the torque ripple remains minimal in this particular method.

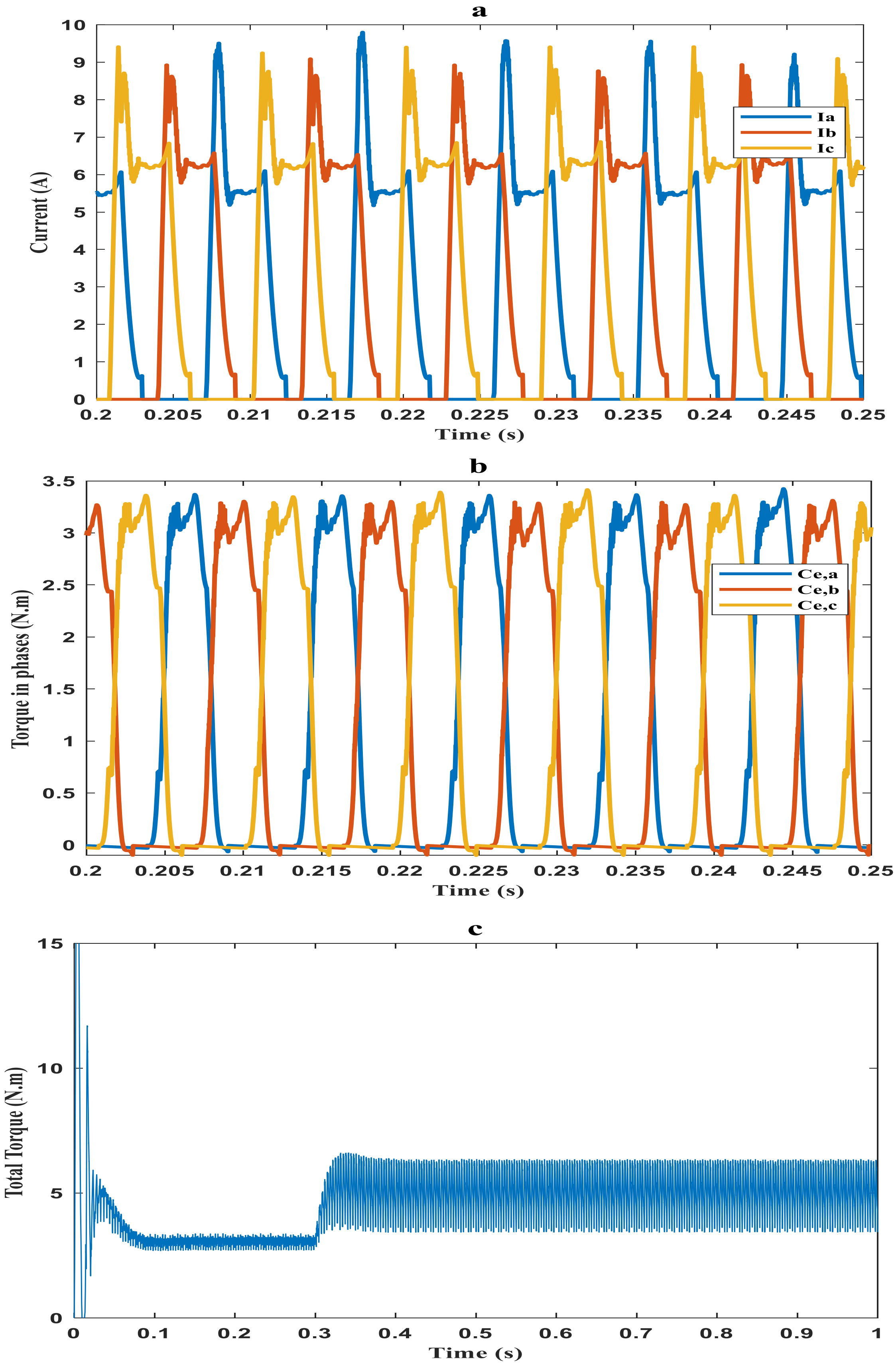
a
Current (A)
10
9
8
7
6
5
4
3
2
1
0
0.2
0.205
0.21
0.215
0.22
0.225
0.23
0.235
0.24
0.245
0.25
Time (s)
Ia
Ib
Ic
b
Torque in phases (N.m)
3.5
3
2.5
2
1.5
1
0.5
0
0.2
0.205
0.21
0.215
0.22
0.225
0.23
0.235
0.24
0.245
0.25
Time (s)
Ce,a
Ce,b
Ce,c
c
Total Torque (N.m)
15
10
5
0
0
0.1
0.2
0.3
0.4
0.5
0.6
0.7
0.8
0.9
1
Time (s)

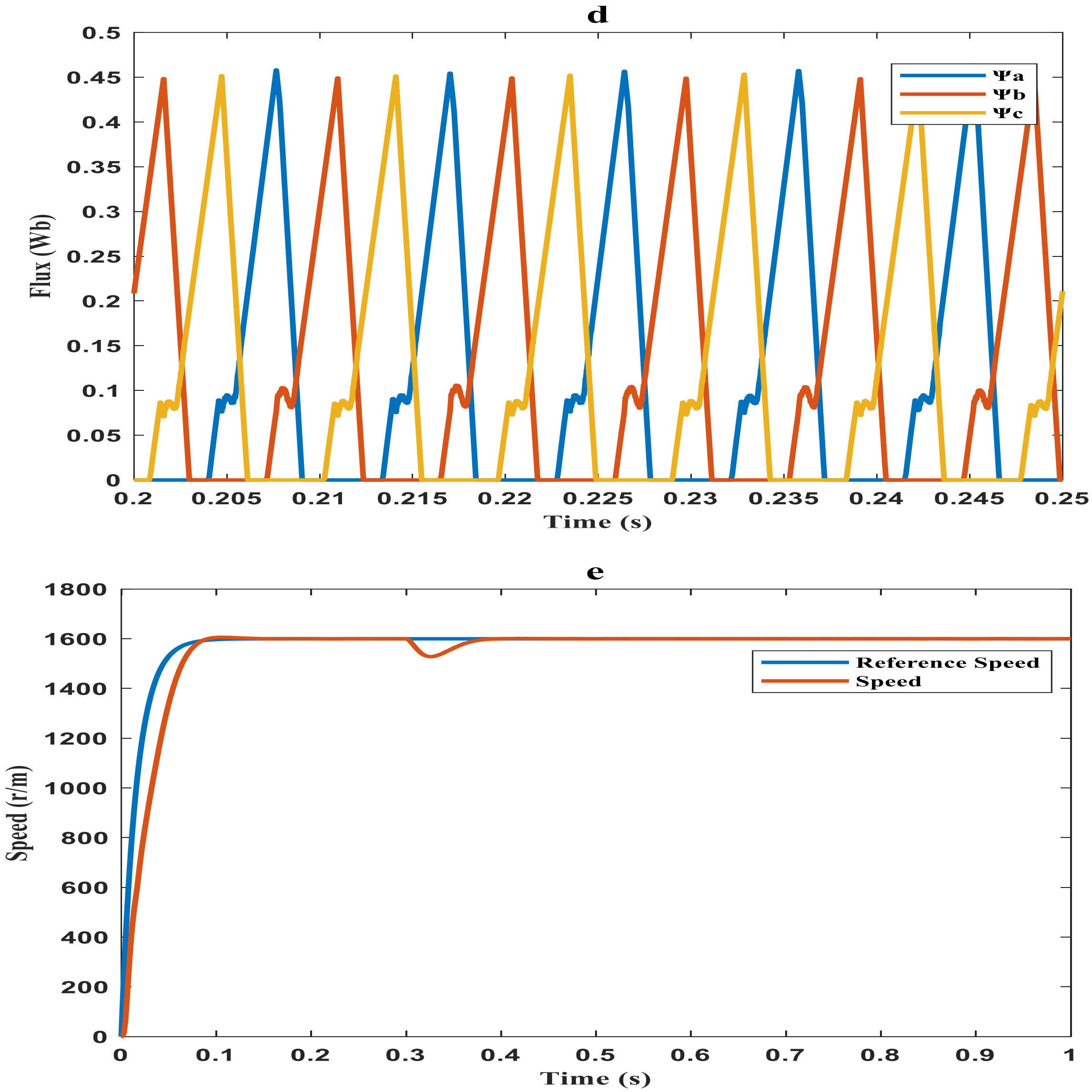

Figure III.15. Simulation results of Direct Energy Control with the SRM working with a charge applied 2 N.m (a: Current, b: Torque in phases, c: Total Torque, d: Flux, and e: Speed).

III.4.5. Direct Energy and Force Control DEFC

After conducting an in-depth analysis of existing research on Switched Reluctance Motors (SRMs), we have identified potential enhancements in current control methodologies applied to these motors. In our pursuit to improve SRM efficiency, we propose a novel control technique named Direct Energy and Force Control (DEFC). Drawing inspiration from direct torque control, DEFC aims to achieve consistent overall radial force and energy by effectively manipulating the converter switches. The objective is to align the total radial forces and energies generated by the stator phases with predefined values, Fref and Wref, respectively.

The DEFC control method generates switching signals for the power converter, strategically minimizing the differences (dF and dW) between the desired radial force and energy and their actual sums from each phase. Introducing a unique approach, the Direct Force and Energy Controller involves the computation of digital control signals applied to the SRM's converter. DEFC employs two hysteresis controller units for force and one for energy, generating precise switching signals for each phase of the SRM. The DEFC command diagram, depicted in Figure III.16, provides a visual representation of this innovative control strategy.

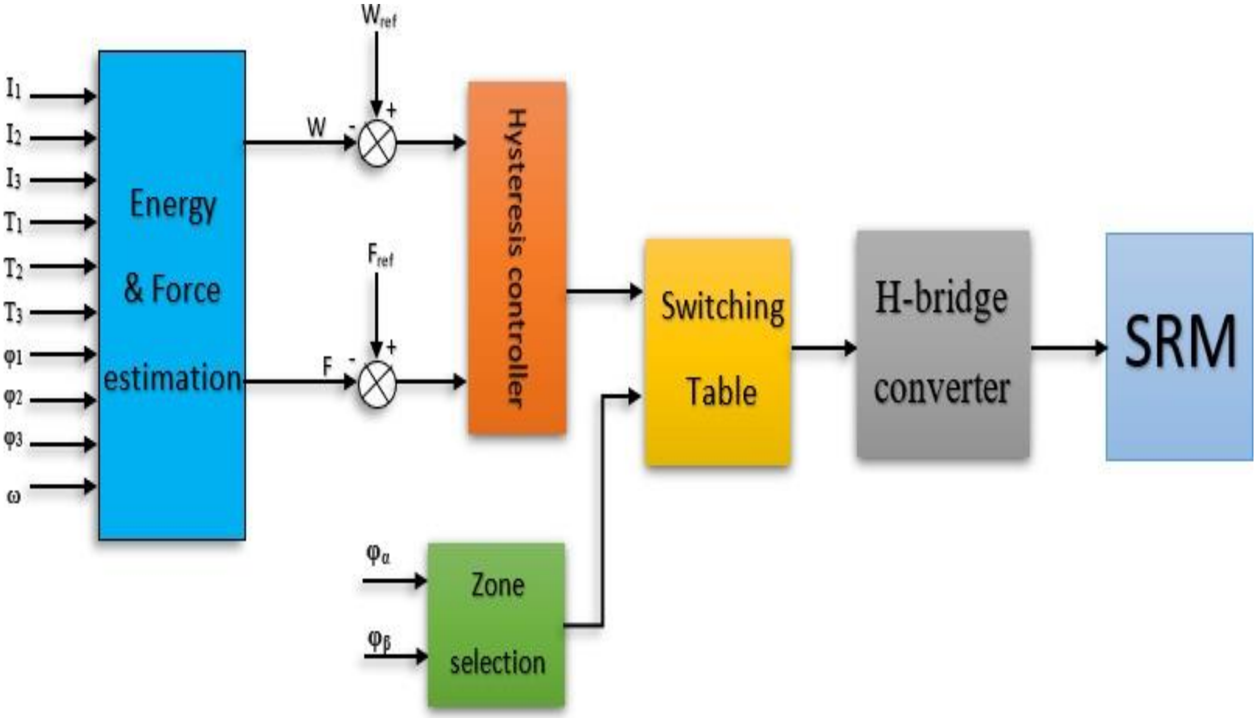

Figure III.16. Schematic for Direct Energy and Force control DEFC.

The energy W is represented by the following equation.

$$\overline{W}(\theta,i) = L(\theta)i \tag{III.21}$$

From equation 3 we find:

$$\overline{W}(\theta,i) = \frac{1}{2} i\, \Psi(\theta,i) \tag{III.22}$$

the force F is determined by the following equations:

$$\mathrm{Ce}(\theta,\mathrm{i}) = \frac{1}{2}\frac{\mathrm{F}(\theta,\mathrm{i})}{\omega} * \mathrm{i}(\theta) \tag{III.23}$$

$$\mathrm{F}(\theta,\mathrm{i}) = \frac{2*\mathrm{Ce}(\theta,\mathrm{i})*\omega}{\mathrm{i}(\theta)} \tag{III.24}$$

the organizational chart of the DEFC is represented in figure III.17.

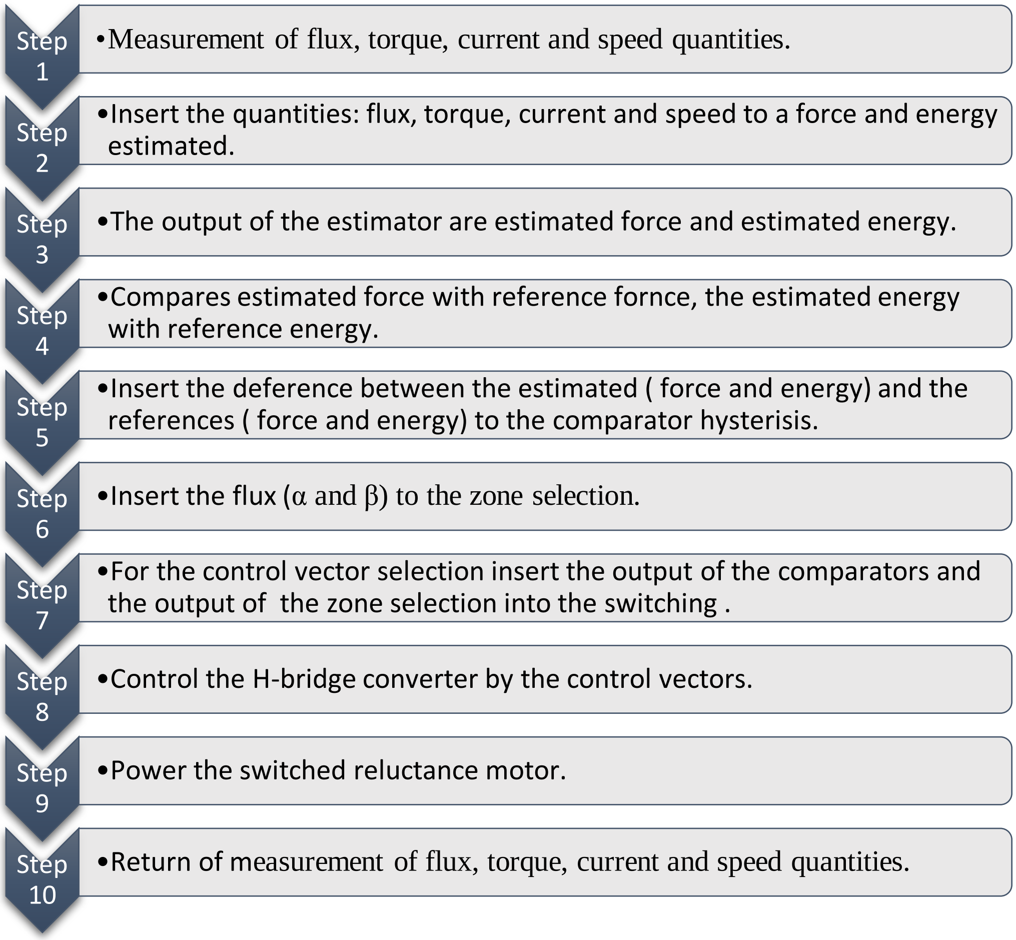

Step 1 •Measurement of flux, torque, current and speed quantities.

Step 2 •Insert the quantities: flux, torque, current and speed to a force and energy estimated.

Step 3 •The output of the estimator are estimated force and estimated energy.

Step 4 •Compares estimated force with reference fornce, the estimated energy with reference energy.

Step 5 •Insert the deference between the estimated (force and energy) and the references (force and energy) to the comparator hysterisis.

Step 6 •Insert the flux (α and β) to the zone selection.

Step 7 •For the control vector selection insert the output of the comparators and the output of the zone selection into the switching .

Step 8 •Control the H-bridge converter by the control vectors.

Step 9 •Power the switched reluctance motor.

Step 10 •Return of measurement of flux, torque, current and speed quantities.

Fig.III.17 organizational chart of the direct Energy and Force control DEFC.

In the realm of Switched Reluctance Motors (SRMs), the widely adopted asymmetric half-bridge circuit serves as the preferred power converter, valued for its simplicity and phase independence. The critical task of selecting the appropriate voltage vector relies on the corrector's output, which indicates the direction of energy module development. A straightforward two-level hysteresis corrector proves remarkably effective, delivering excellent dynamic performance. The corrector's output, presented as a Boolean variable, directly communicates whether the energy amplitude should increase (1) or decrease (0).

Moreover, employing a three-level hysteresis corrector enables versatile control of the SR motor in both rotation directions. The corrector's output, expressed as a Boolean variable, dictates whether the force amplitude should increase in absolute value (1) for a positive setpoint, decrease in absolute value (-1) for a negative setpoint, or remain unchanged (0). The voltage vector choices and control sectors are vividly illustrated in Table III.4 and Figure III.18, respectively.

The primary goal of the energy corrector is to confine the extremity of vector W within a rounded crown. For selecting the appropriate voltage vector, the corrector's output must indicate the direction in which the modulus of W is evolving. The utilization of a straightforward two-level hysteresis corrector proves highly suitable for this purpose, ensuring exceptional dynamic performance. The corrector's output represented as a Boolean variable, straightforwardly conveys whether the energy amplitude should increase (1) or decrease (0).

By incorporating a three-level hysteresis corrector, the SR motor gains control in both rotational directions, accommodating positive and negative forces. The corrector's output, expressed as a Boolean variable, guides the adjustment of force amplitude, increasing it in absolute value (1) for a positive setpoint, decreasing it in absolute value (-1) for a negative setpoint, and remaining unchanged (0) otherwise. Figure III.18 and Table III.4 provide a comprehensive graphical representation of the voltage vectors and their corresponding control sectors.

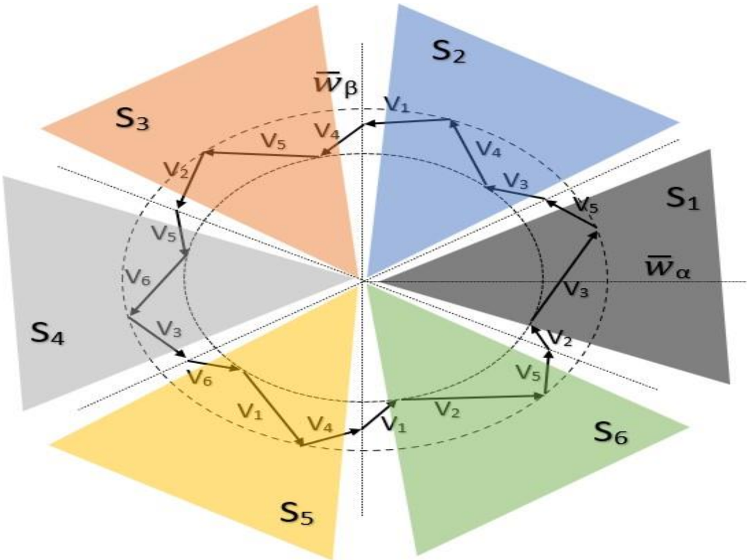

Figure III.18.Schematic of Selection of vectors of control.

section	dF=1, dW=1	dF=1, dW=0	dF=0, dW=1	dF=0, dW=0	dF=-1, dW=1	dF=-1, dW=0
S1	V2	V3	V7	V0	V6	V5
S2	V3	V4	V0	V7	V1	V6
S3	V4	V5	V7	V0	V2	V1
S4	V5	V6	V0	V7	V3	V2
S5	V6	V1	V7	V0	V4	V3
S6	V1	V2	V0	V7	V5	V4

Table III.4. Selection of vectors of control.

In the proposed Direct Energy and Force Control (DEFC) method, the total torque initially registers at 3.7 Nm. Upon the introduction of a load to the Switched Reluctance Motor (SRM), the torque undergoes a notable increase, reaching 6.4 Nm. Concurrently, the current experiences a shift from 8A to 12 A, and the flux displays variations within the range of 0.28 Wb to 0.32 Wb. Remarkably, the speed closely follows the reference speed even under load conditions, demonstrating a rapid response and the most optimal performance among the previously mentioned methods in swiftly reaching the reference speed. Additionally, the SRM exhibits a notable reduction in torque ripple when compared to the preceding methods, highlighting the enhanced stability and efficiency of the DEFC approach.

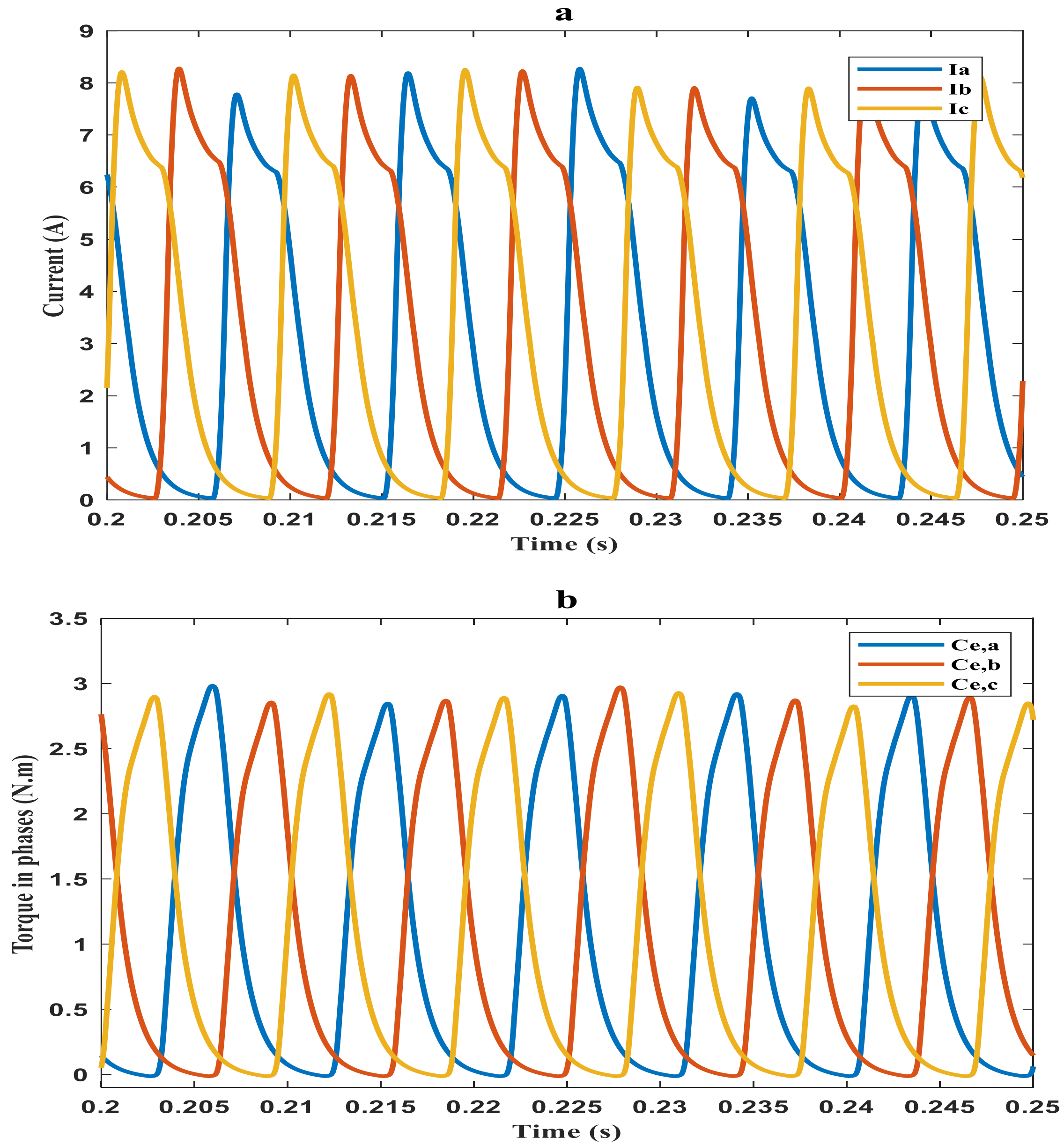

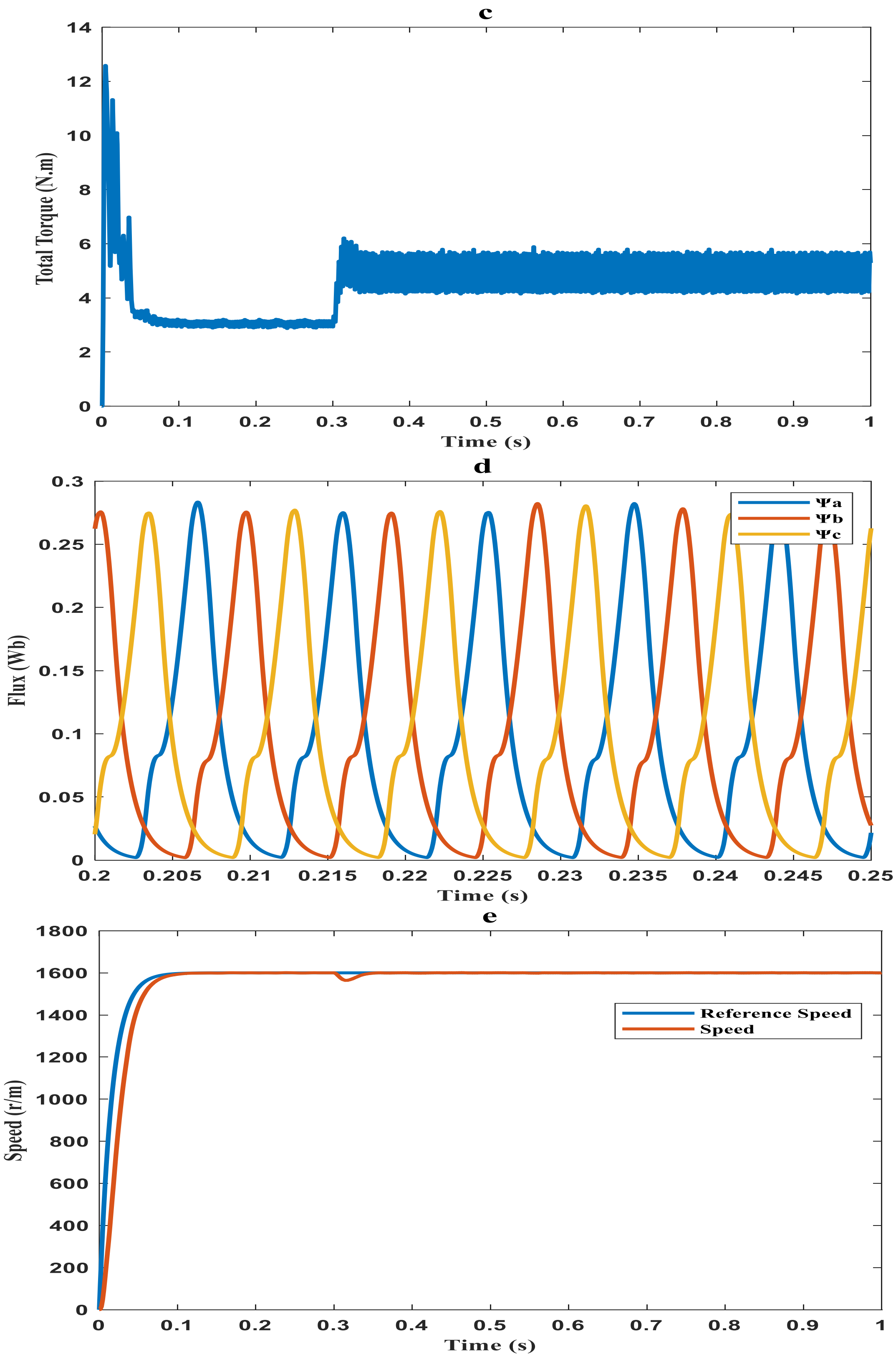

Figure III.19. Simulation results of Direct Energy And Force Control with the SRM working with a charge applied 2 N.m (a: Current, b: Torque in phases, c: Total Torque, d: Flux, and e: Speed).

III.5.Comparison with different methods

Throughout this section, the motor is operated at various speeds for each of the methods (DTC, DEC, DFC and proposed method DEFC) that were examined in order to compare them and determine which produces the least torque ripple. Utilizing this relationship to determine the torque ripple factor Trf, we can determine the torque ripple ratio.

$$Trf = \frac{Tmax - Tmin}{Tav} \qquad \text{(III.25)}$$

Three key torque parameters, Tmax (maximum torque), Tmin (minimum torque), and Tav (average torque), play a pivotal role in evaluating the performance of different control methods. Simulation results for Direct Torque Control (DTC), Direct Energy Control (DEC), Direct Force Control (DFC), and the proposed method Direct Energy and Force Control (DEFC) are systematically presented in tables, considering various speeds (2200, 2000, 1800, 1600, 1400, and 1200 r/m) for the Switched Reluctance Motor (SRM). For each speed, comprehensive data including total torque, torque in phases, current, and flux are collected, and the torque ripple factor is calculated to assess the efficacy of each control method.

Upon comparison, it is evident that the DEFC method yields the lowest torque ripple factor across different speeds. At 2200 r/m, DEFC achieves a Trf of 37%, surpassing DTC (Trf = 70%), DEC (Trf = 38%), and DFC (Trf = 44%). Similarly, at 2000 r/m, DEFC and DEC both exhibit a torque ripple factor of 31%, outperforming DFC (Trf = 62%) and DTC (Trf = 55%). Notably, at 1600 r/m, DEFC stands out with a torque ripple factor of 10%, while DEC, DFC, and DTC register 11%, 11%, and 31%, respectively. Remarkably, the SR motor demonstrates the lowest torque ripple factor at 1600 r/m across all studied methods, emphasizing DEFC's superior efficiency.

Through a comprehensive analysis of different control methods, it is evident that the proposed DEFC method consistently outperforms others, showcasing the SRM's highest efficiency and significantly reducing torque ripple. This superior performance contributes to the minimization of vibration in the Switched Reluctance Motor, validating DEFC as a promising and effective control strategy.

Speed (r/m)	Total torque (N.m)	Torque in phase (N.m)	Current (A)	Flux (Wb)	Trf (%)
2200	5,34	5,42	17,2	0,395	70
2000	4,6	4,72	17,15	0,38	55
1800	3,9	4,15	17	0,382	36
1600	3,4	3,53	13,4	0,4	31
1400	3,42	3,45	7,15	0,45	43

Table III.5. torque ripple factor of DTC.

Speed (r/m)	**Total torque (N.m)**	**Torque in phase (N.m)**	**Current (A)**	**Flux (Wb)**	**Trf (%)**
2200	5, 6	5, 7	15, 95	0, 415	39
2000	4, 9	4, 87	16, 4	0, 409	34
1800	4, 15	4, 1	20, 1	0, 435	26
1600	3, 4	3, 38	10, 4	0, 43	14
1400	3, 6	3, 58	7, 5	0, 48	37

Table III.6. torque ripple factor of DFC.

Speed (r/m)	**Total torque (N.m)**	**Torque in phase (N.m)**	**Current (A)**	**Flux (Wb)**	**Trf (%)**
2200	6, 4	6, 15	16, 5	0, 385	44
2000	5, 5	5, 25	13, 2	0, 387	42
1800	4, 5	4, 4	17, 5	0, 386	27
1600	3, 4	3, 4	16	0, 39	13
1400	3, 65	3, 6	7, 4	0, 452	39

Table III.7. torque ripple factor of DEC.

Speed (t/m)	**Total torque (N.m)**	**Torque in phase (N.m)**	**Current (A)**	**Flux (Wb)**	**Trf (%)**
2200	5, 8	5, 85	16, 4	0, 39	37
2000	5	5, 05	17, 05	0, 385	31
1800	4, 2	4, 23	17, 4	0, 383	23
1600	3, 3	3, 28	15, 8	0, 395	10
1400	3, 55	3, 56	7, 6	0, 475	35

Table III.8. torque ripple factor of DEFC.

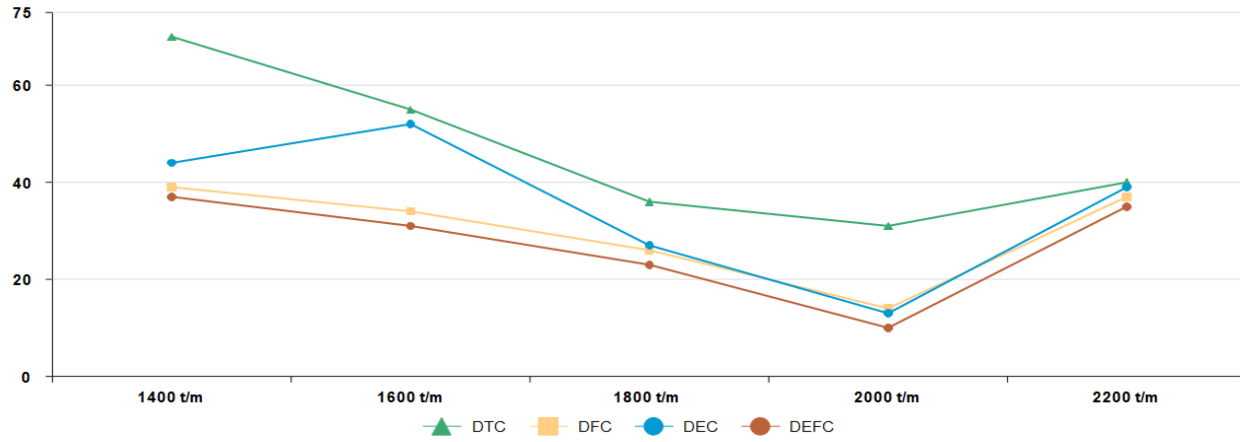

Figure III.20. torque ripple factor.

Conclusion

This chapter offers a comprehensive exploration and discussion of the simulation of Switched Reluctance Motors (SRMs). It became evident that relying solely on the linear model for accurate torque oscillation analysis is insufficient. To delve into the dynamic behavior of the SRM, numerous simulations were conducted, with a primary focus on understanding the impact of the angle on its dynamics. It became evident that optimizing this angle proves instrumental in mitigating torque oscillations. The characteristics reflecting co-energy were utilized to glean insights into the quality of the average electromagnetic torque.

In validating the model, various control strategies, including current control, direct torque control, direct force control, direct energy control, and the proposed Direct Energy and Force Control (DEFC), were simulated. DEFC, a novel approach to Switched Reluctance Motor control, introduces groundbreaking methods to minimize torque ripple and vibration. In direct comparison to conventional methods like direct torque control (DTC), DEFC exhibits superior motor efficiency. Through extensive simulations, DEFC achieved a noteworthy torque ripple of approximately 10%, a substantial improvement compared to the 36% observed with DTC. The dual control of force and energy in DEFC replaces traditional torque and flux control, resulting in significant enhancements to motor performance. These findings underscore the promising potential of DEFC in advancing the control of SRMs.

Introduction

This chapter revolves around the enhancement of operational efficiency in Switched Reluctance Machines (SRMs) by introducing various control methodologies, namely Direct Energy and Force Control (DEFC), Direct Force Control, Direct Energy Control, Direct Torque Control, and Current Control. The primary focus is on their application within the realm of electric vehicles (EVs). The innovative system seamlessly integrates a Photovoltaic (PV) system with a Switched Reluctance Motor (SRM), meticulously managed through the proposed control methodologies. DEFC, distinguished for simultaneously regulating energy and force dynamics within the motor, aims to mitigate torque fluctuations, reduce vibration, and enhance overall motor performance. The PV system employs Maximum Power Point Tracking (MPPT) to optimize electricity generation. Furthermore, the chapter addresses the dynamic aspects of the electric vehicle, including variables such as rolling resistance force, aerodynamic drag force, vehicle speed, and acceleration. A comprehensive exploration of these dynamics is undertaken to understand the intricate interactions between the PV-SRM system and the operational parameters of the vehicle.

IV.1. System under study

The solar-powered Switched Reluctance Motor (SRM) system comprises several integral components, with a photovoltaic generator at its core responsible for harvesting solar energy from the sun. The collected energy undergoes optimization through a boost converter, expertly controlled via Maximum Power Point Tracking (MPPT) technology. This MPPT-controlled converter precisely aligns the system's operation with its maximum power point, thereby enhancing the efficiency of energy extraction from the solar panels. Driving the system is the Switched Reluctance Motor, energized by a half-bridge converter. To govern the motor's torque output with precision, sophisticated control methods such as Direct Energy and Force Control, Direct Force Control, Direct Energy Control, Direct Torque Control, and Current Control are employed. These control strategies ensure meticulous calibration of the motor's torque output, a critical requirement for applications in electric vehicles where consistent and controlled torque levels are paramount.

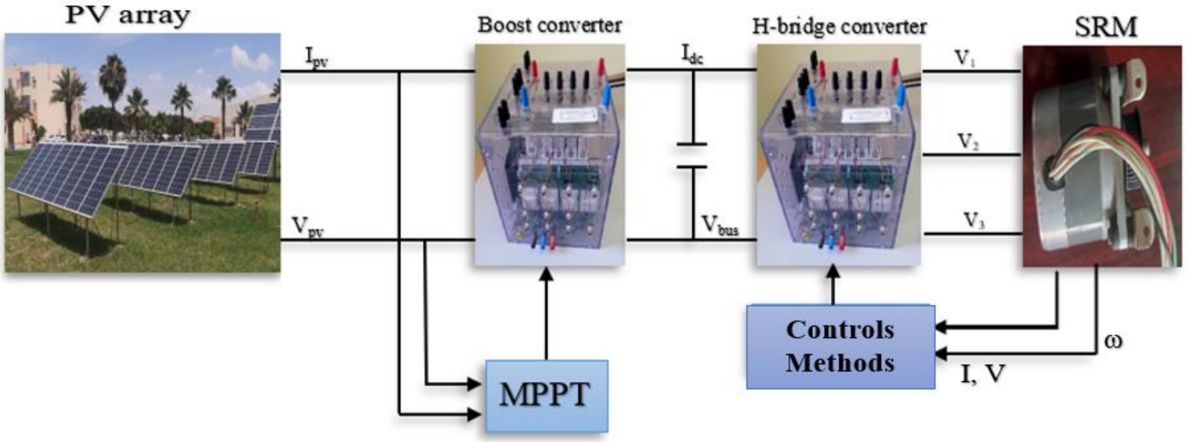

Figure IV.1. Schema of the system under study.

In our system, four distinct operational modes can be implemented to cater to a range of specific requirements. These modes encompass Mode 1, functioning without MPPT for generator photovoltaic operation; Mode 2, which incorporates MPPT technology for enhanced efficiency in generator photovoltaic utilization; Mode 3, specifically designed for battery-centric operations; and Mode 4, a hybrid mode that merges generator photovoltaic capabilities with battery functionality. Although the primary focus of this endeavor centers on Mode 2, which optimizes the use of generator photovoltaic through MPPT technology, the versatility and adaptability of our system across these various modes showcase its flexibility and effectiveness in meeting diverse energy needs.

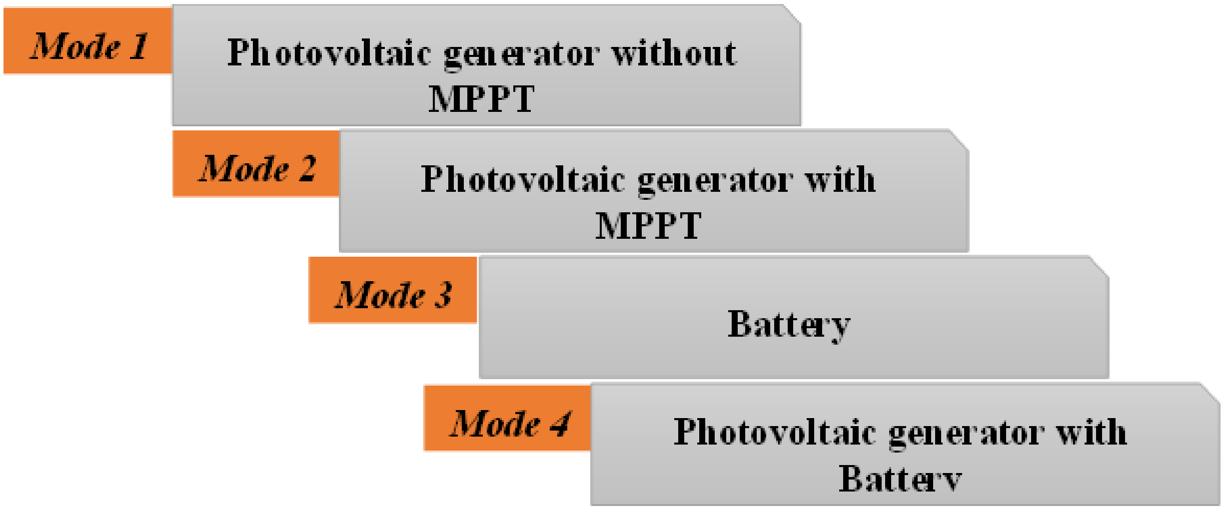

Figure IV.2. . The power management of the system .

IV.1.1. Photovoltaic system

In this study, essential meteorological data crucial for analysis was gathered using sensors that measured solar irradiance, temperature, wind speed, and atmospheric pressure (refer to Figure IV.3). The primary objective was to assess both seasonal variations and long-term climatic trends using this dataset. The focus was on understanding how these fluctuations impact the performance of solar panels and, consequently, developing a photovoltaic system capable of consistently achieving optimal efficiency. The selection for this research was the "Suntech-STP190S-24AD+" photovoltaic generator (see Table IV.1). Specifically, for the switched reluctance motor 6/4, a configuration of five photovoltaic modules in series was employed to ensure the half-bridge converter received the required voltage of 120 volts. This choice was informed by the power consumption of the SRM at 750 W, while the photovoltaic generator produced 190 W, thereby guaranteeing a well-balanced and efficient power supply for the motor.

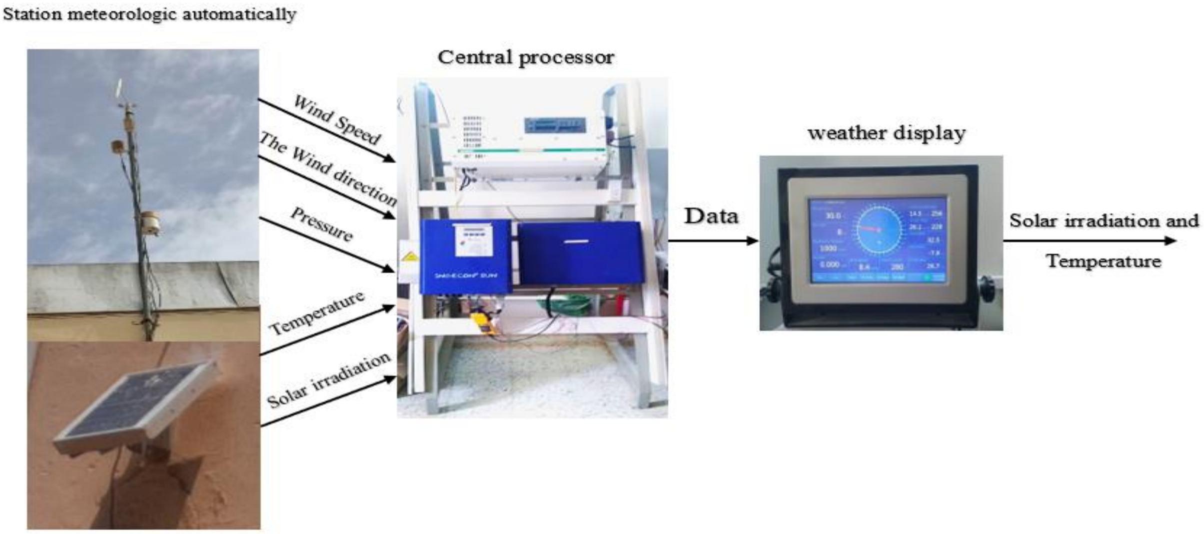

Figure IV.3. Measuring tool of the meteorological.

Pmax	**190W**
No. of solar cells	**72**
Vmax (V)	**36.6V**
Impp (A)	**5.20A**
Open circuit voltage Vop	**45.2V**

Table IV.1. The "Suntech-STP190S-24AD+" photovoltaic generator parameter.

IV.1.2. Control of the booster converter linked to the photovoltaic generator

Various Maximum Power Point Tracking (MPPT) techniques exist for evaluating the maximum power from photovoltaic (PV) sources. In this study, two specific methods were chosen, recognizing that these are not the exclusive options available but were found effective in achieving maximum power under varying radiation conditions. The first selected method is MPPT Perturb and Observe, a widely employed technique that dynamically adjusts the operating point by perturbing the operating voltage and observing the resulting change in power to find the optimum point. The second method adopted is the backstepping technique, which utilizes a systematic control approach to iteratively adjust the operating point, optimizing the PV system's power output. These chosen techniques were deemed suitable for maximizing power extraction in response to changes in radiation during the course of this investigation.

IV.1.2.1. Maximum PowerPoint Track (MPPT)

The PV Power Variation (PPV) and PV Voltage Variation (VPV) are essential input parameters utilized for computing the optimal voltage corresponding to maximum power output in photovoltaic (PV) systems. In this context, the maximum power point (MPP) is determined by implementing an incremental adjustment to the operating voltage, guided by the output of a fuzzy controller. Unlike the perturbation and observation (P&O) method, which employs a fixed perturbation for operating voltage determination and may lead to oscillations around the MPP in steady-state conditions, our proposed MPPT algorithm introduces a novel approach. This algorithm addresses the oscillation issue associated with the P&O method by integrating fuzzy logic theory. The suggested fuzzy controller dynamically adjusts the perturbation magnitude, aiming to minimize oscillations and facilitate a rapid response without undesired oscillatory behavior.

Within the scope of this research, a boost converter is utilized as a step-up converter. In the context presented, the duty cycle of the Pulse Width Modulation (PWM) switching signal is denoted by the variable 'k.' Concurrently, the output voltage of the converter is symbolized by 'Vo.'

$$Vo = \frac{Vs}{1-k} \tag{IV.1}$$

IV.1.3. Vehicle Dynamics

In the realm of electric vehicles (EVs), the Switched Reluctance Motor (SRM) serves as a pivotal component, functioning as a traction motor to supply the requisite torque for vehicle propulsion. Effective control of the SRM is imperative for achieving optimal performance and efficiency in electric vehicles. Furthermore, the integration of renewable energy sources, exemplified by a photovoltaic system, synergistically enhances the overall energy efficiency of the EV. This coupling of a Switched Reluctance Motor with a renewable energy source aligns seamlessly with the escalating interest in sustainable and eco-friendly transportation solutions, reflecting a commitment to reducing environmental impact.[81-83]

The equations utilized in this context are directly derived from fundamental principles in mechanics and aerodynamics. Specifically tailored for application in road vehicles with four wheels and rear-wheel drive configurations, these equations characterize the dynamic interplay and aerodynamic considerations intrinsic to this vehicle setup. The propulsive force in this system is engendered by the Switched Reluctance Motor, which simultaneously propels both traction wheels. This design ensures that the equations are meticulously crafted to accurately capture the nuances of the vehicle's performance, underscoring their precision and relevance in the comprehensive analysis of its dynamics.

IV.1.3.1. Rolling resistance force

The deceleration of the vehicle is influenced by the rolling resistance force, primarily arising from the friction between the vehicle's tires and the road surface. Operating in the opposite direction to the vehicle's motion, this force is characterized by a non-linear coefficient denoted $\boldsymbol{\mu}$, which is contingent on various factors including the vehicle's speed, the tire type, and the tire pressure. Notably, the rolling resistance force amplifies with increasing vehicle speed and is further heightened during manoeuvres. The mathematical expression defining this force is as follows:

$$F_{ro} = \mu_{r_0} \cdot m \cdot g \cdot \cos(\alpha) \tag{IV.14}$$

The rolling resistance coefficient, denoted as μ_{r_0}, representing the relationship between the rolling resistance force and the normal force, encapsulates a comprehensive set of interconnected physical properties and phenomena occurring between the tire and the ground. It encompasses the intricate factors influencing the resistance to rolling motion. Specifically, based on the formula proposed by Wong and applicable to radial tires found in passenger vehicles with standard inflation pressure and traversing a smooth road profile, the rolling resistance coefficient is expressed as follows: $\mu_{ro} = 0.006 + 3.10^{-6} v^2$.

IV.1.3.2. Resistant force due to penetration into the air

The motion of the automobile through the air induces an aerodynamic force opposing the relative movement between the vehicle and the surrounding air. This force is a composite of various forces and resisting moments exerted on and around the vehicle. Notably, the point of application of the resultant aerodynamic force differs from the centre of gravity, typically situated on the vehicle's bodywork. The challenge lies in the intricate task of decomposing this force and discerning the moments and reactive forces it engenders. The mathematical expression defining this aerodynamic force is as follows:

$$F_{ad} = \frac{1}{2} \rho \cdot C_w \cdot A_f (v + v_o)^2 \tag{IV.15}$$

IV.1.3.3. Resistant force due to the slope to be climbed

When the vehicle encounters an inclined slope characterized by an angle α, an additional force, denoted as Fp emerges, and it is proportionate to the mass "m" of the vehicle. This force acts in opposition to the vehicle's forward progression up the slope and is mathematically expressed as follows:

$$F_p = \pm m \cdot g \cdot \sin(\alpha) \tag{IV.16}$$

IV.1.3.4. Total tractive force

The resultant force acting on the moving system is determined by aggregating the effects of all external forces acting upon it:

$$F_w = F_{ro} + F_{ad} + F_p \tag{IV.17}$$

The propulsive force for an electric vehicle is generated by its electric motor, tasked with overcoming the various resistances encountered on the road. The equation governing the motion of the vehicle, in this context, is expressed as follows:

$$m\frac{dv}{dt} = F - F_w \tag{IV.18}$$

The force $(F - F_w)$ accelerates the vehicle (or decelerates it when F_w exceeds F).

It should be noted that when the force F_p is negative, the vehicle goes down a slope.

Under the assumption that the resultant force aligns collinearly with the direction of motion, the work performed by the body is defined as follows:

$$\vec{W} = \sum_{i=1}^{3} \vec{F_i} \cdot d\vec{x} \tag{IV.19}$$

By expressing the work over time, we derive the mechanical power:

$$P = \frac{d\vec{W}}{dt} = \vec{F}\left(\frac{d\vec{x}}{dt}\right) \Leftrightarrow P = \vec{F} \cdot v \tag{IV.20}$$

If G represents the speed ratio of the system linking the motor to the axis, and T_m denotes the motor torque, it can be asserted that:

$$T_m = F_w \cdot \frac{r}{G} \tag{IV.21}$$

By applying the aerodynamic equations detailed in this paragraph, we can construct a comprehensive model for the electric vehicle, as depicted in Figure (IV.4).

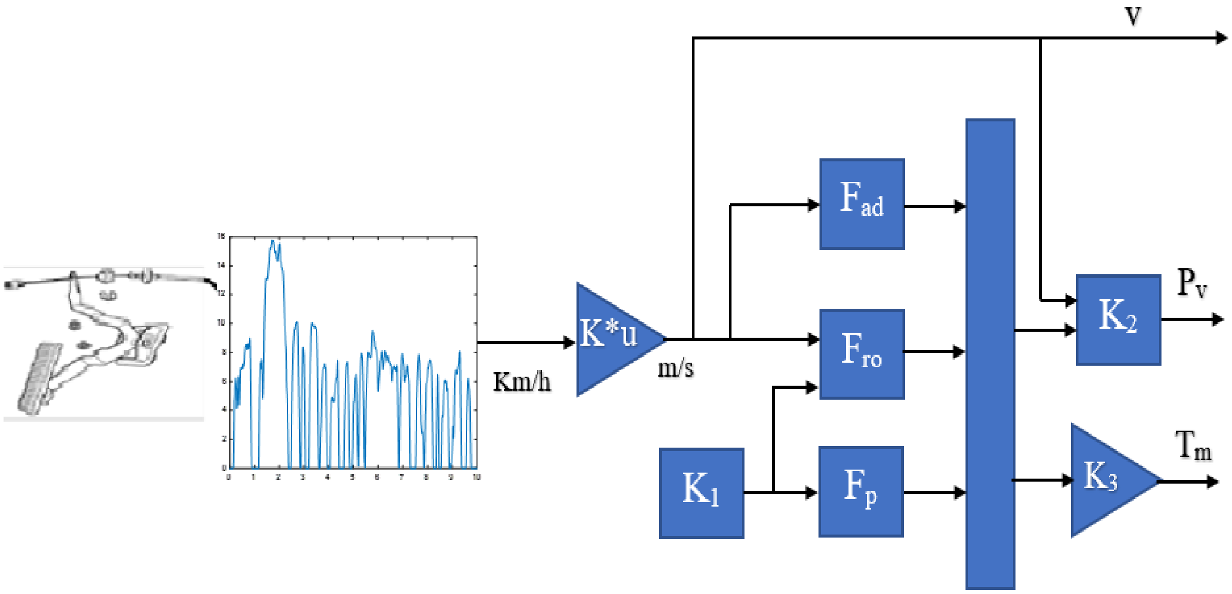

Figure IV.4. Diagram of electric vehicle dynamics.

This model serves as a representation of the aerodynamics governing the vehicle. It elucidates the primary factors and outcomes of the variables influencing the vehicle. Furthermore, it computes all dynamic forces acting upon the vehicle, reflecting the reference parameters (rotation speed, mechanical torque, and mechanical power) essential for overseeing the powertrain system.

IV.2. Simulation results

IV.2.1.MPPT without load

This section showcases the simulation results for five different control strategies: Direct Torque Control (DTC), Direct Energy Control (DEC), Direct Force Control (DFC), our novel approach, Direct Energy and Force Control (DEFC), and current control. The performance evaluation criteria include total torque, flux, and speed, with simulations carried out on the switched reluctance motor (SRM). The system was initially tested under defined conditions of 1000 W/m2 irradiation level and 25°C temperature, with variations in reference speed introduced at different time points to assess the effectiveness of each control method.

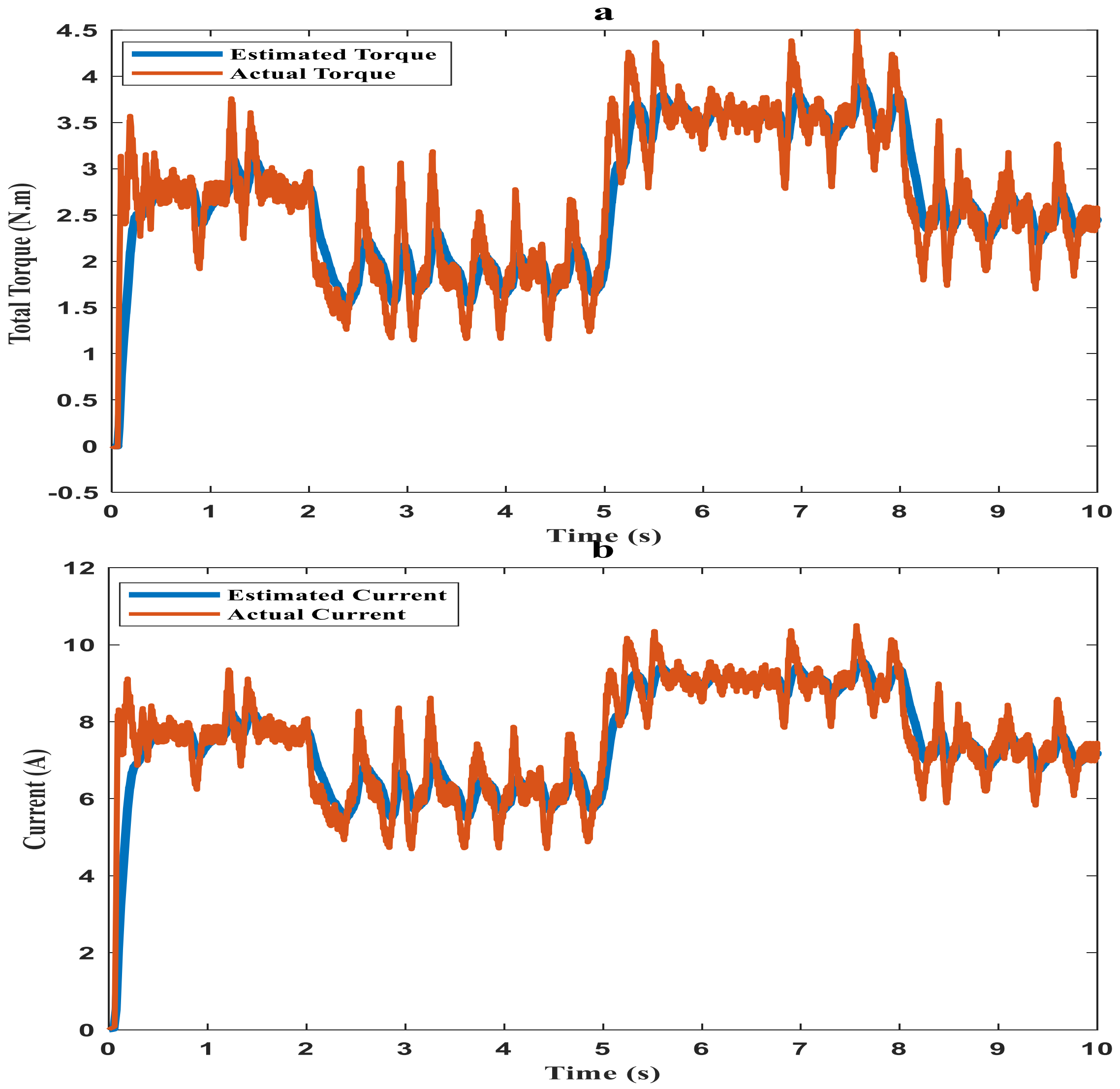

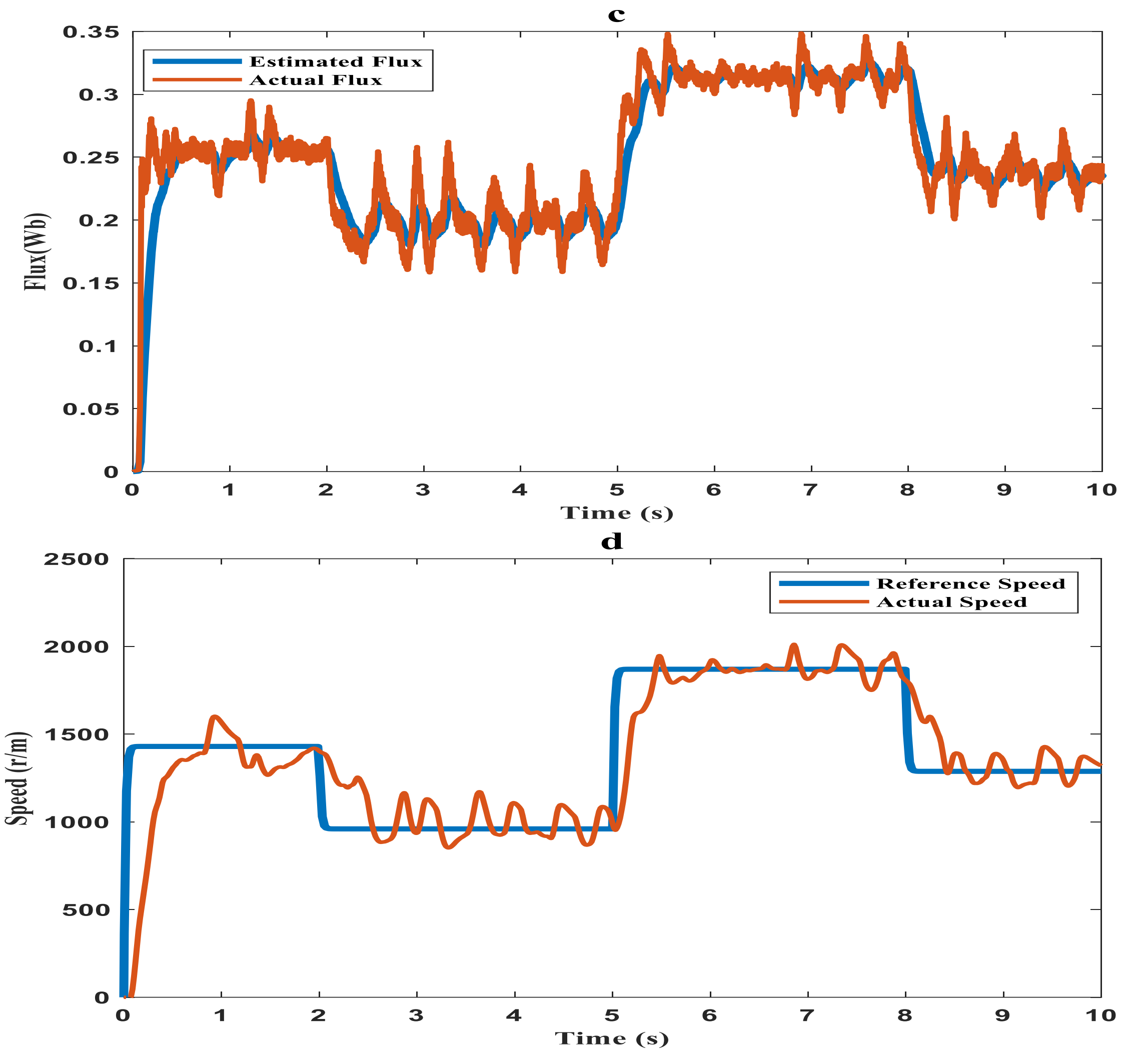

Figure IV.5. The Simulation results of direct torque control with irradiation 1000 r/m2 and 25° c (a: total torque, b: current, c: flux, d: speed).

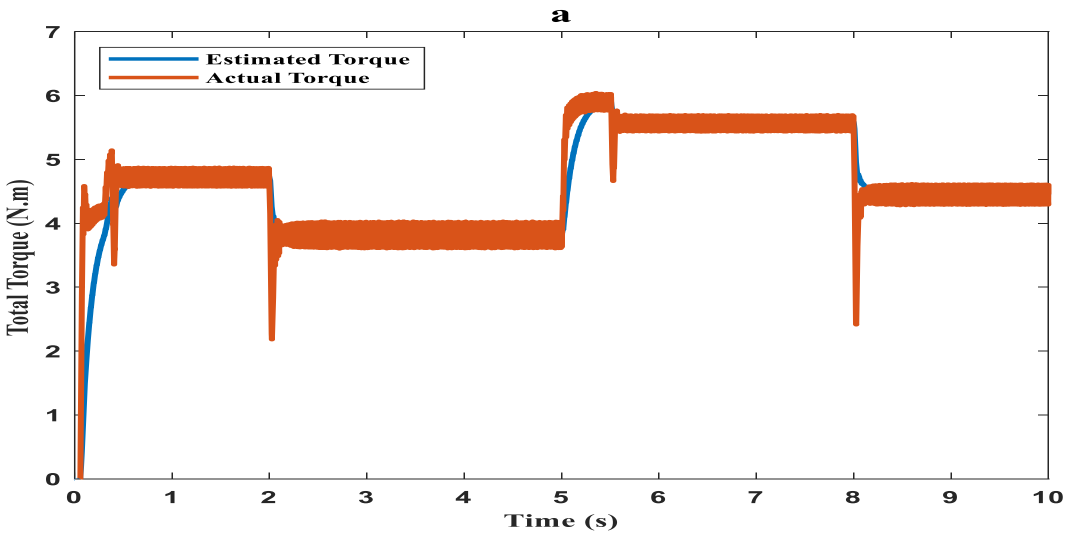

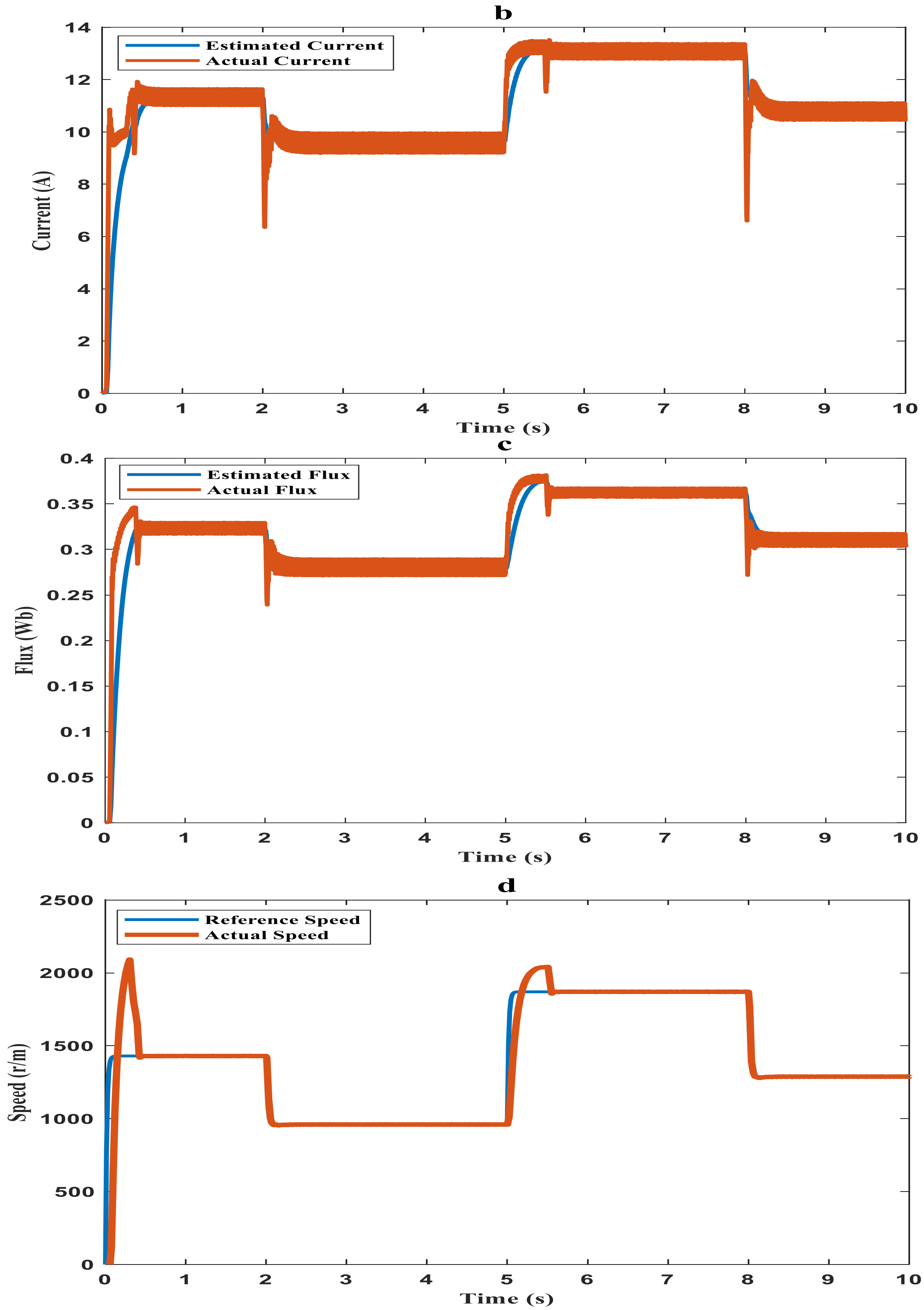

Figure IV.6. The Simulation results of direct Force control with irradiation 1000 r/m2 and 25° c (a: total torque, b: current, c: flux, d: speed).

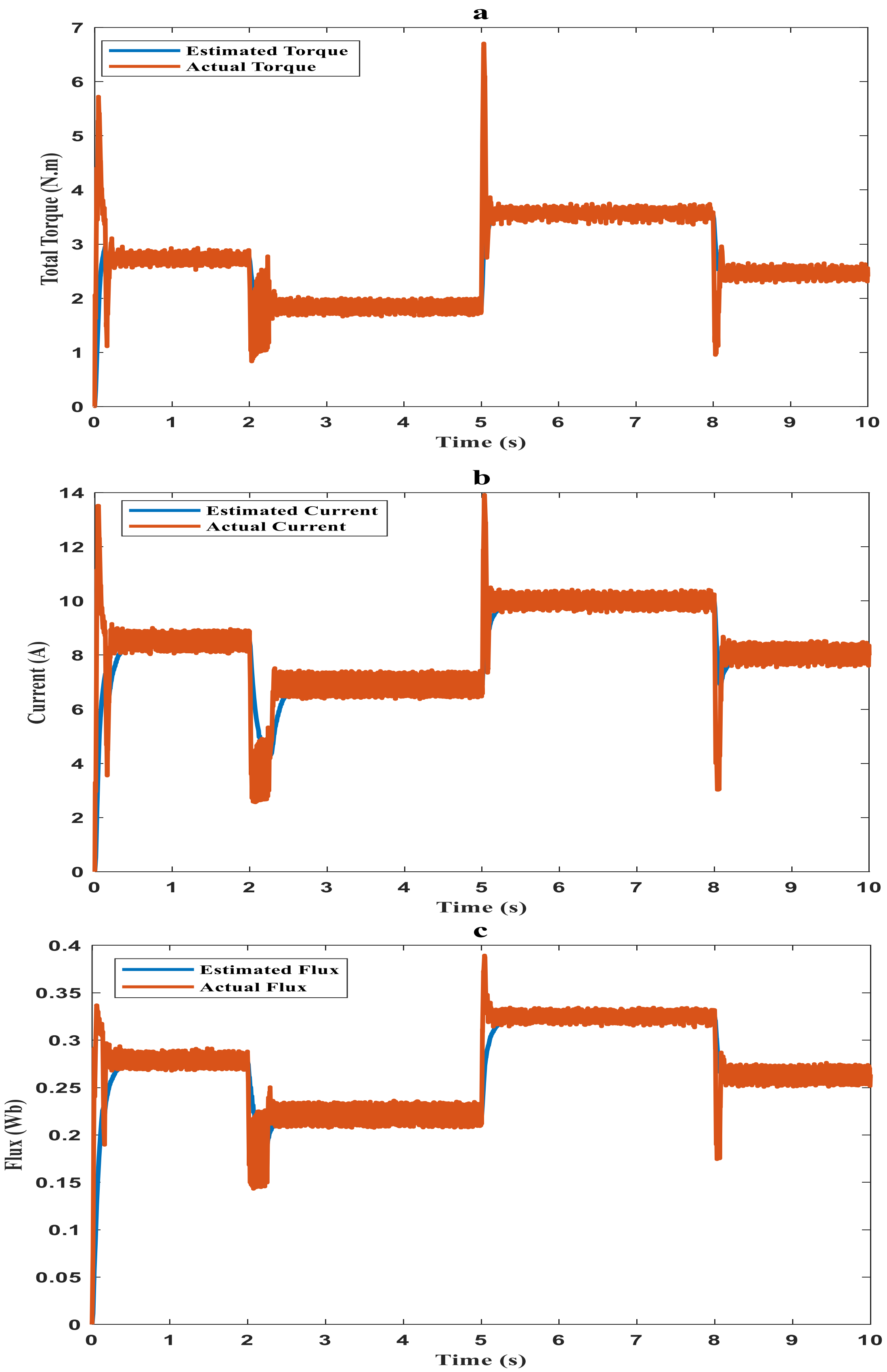
a
Estimated Torque
Actual Torque
Total Torque (N.m)
0
1
2
3
4
5
6
7
Time (s)
0
1
2
3
4
5
6
7
8
9
10
b
Estimated Current
Actual Current
Current (A)
0
2
4
6
8
10
12
14
Time (s)
0
1
2
3
4
5
6
7
8
9
10
c
Estimated Flux
Actual Flux
Flux (Wb)
0
0.05
0.1
0.15
0.2
0.25
0.3
0.35
0.4
Time (s)
0
1
2
3
4
5
6
7
8
9
10

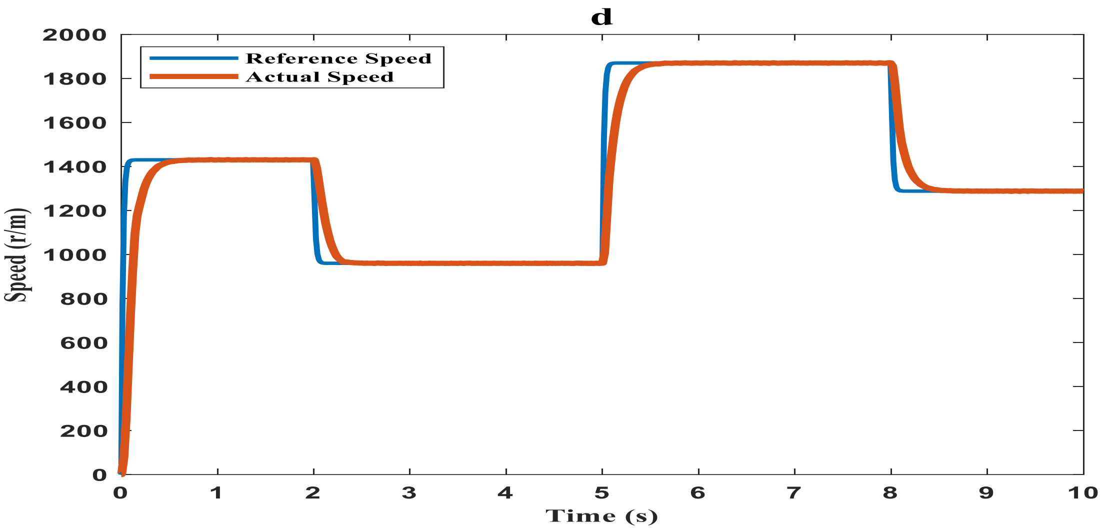

Figure IV.7. The Simulation results of direct Energy control with irradiation 1000 r/m2 and 25° c (a: total torque, b: current, c: flux, d: speed).

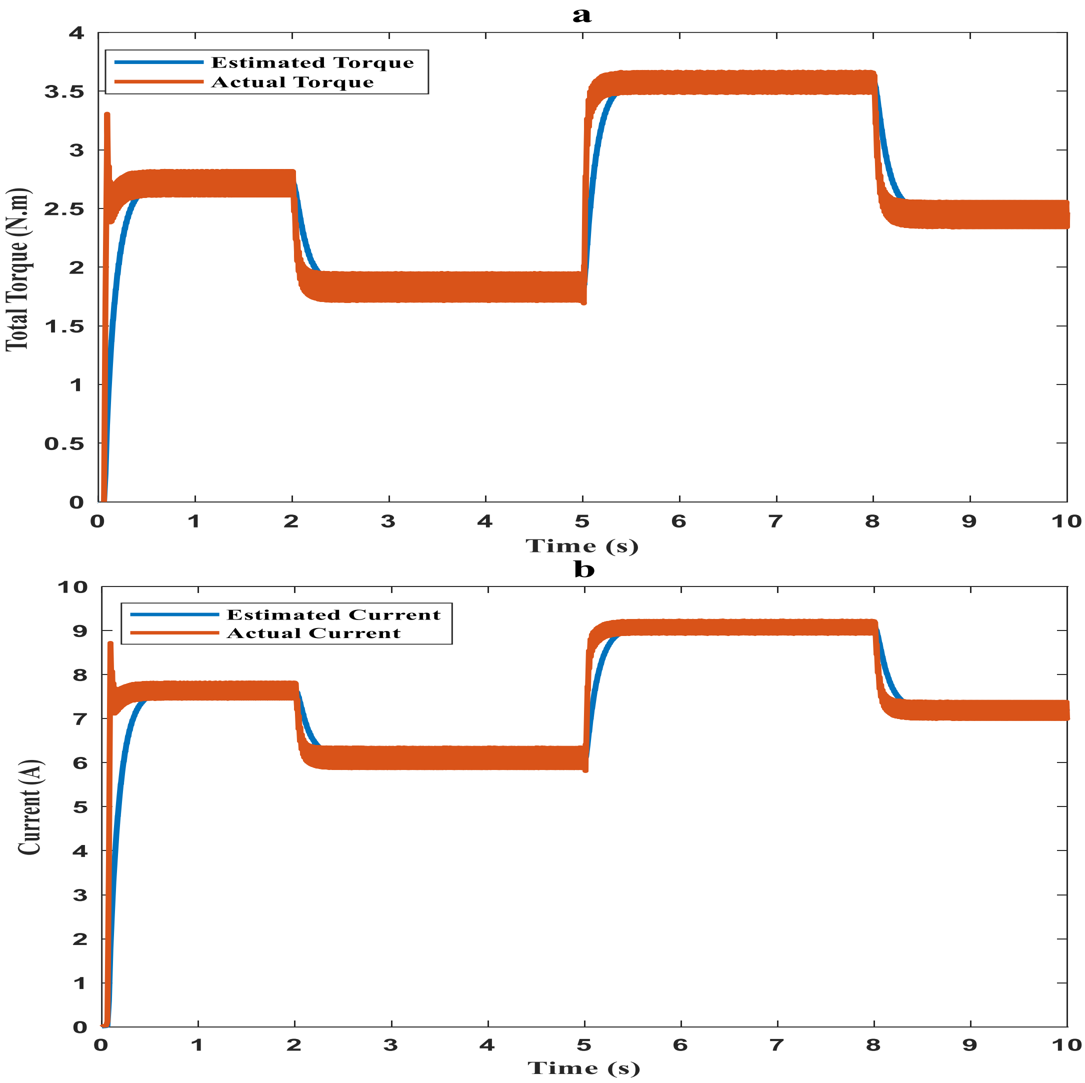

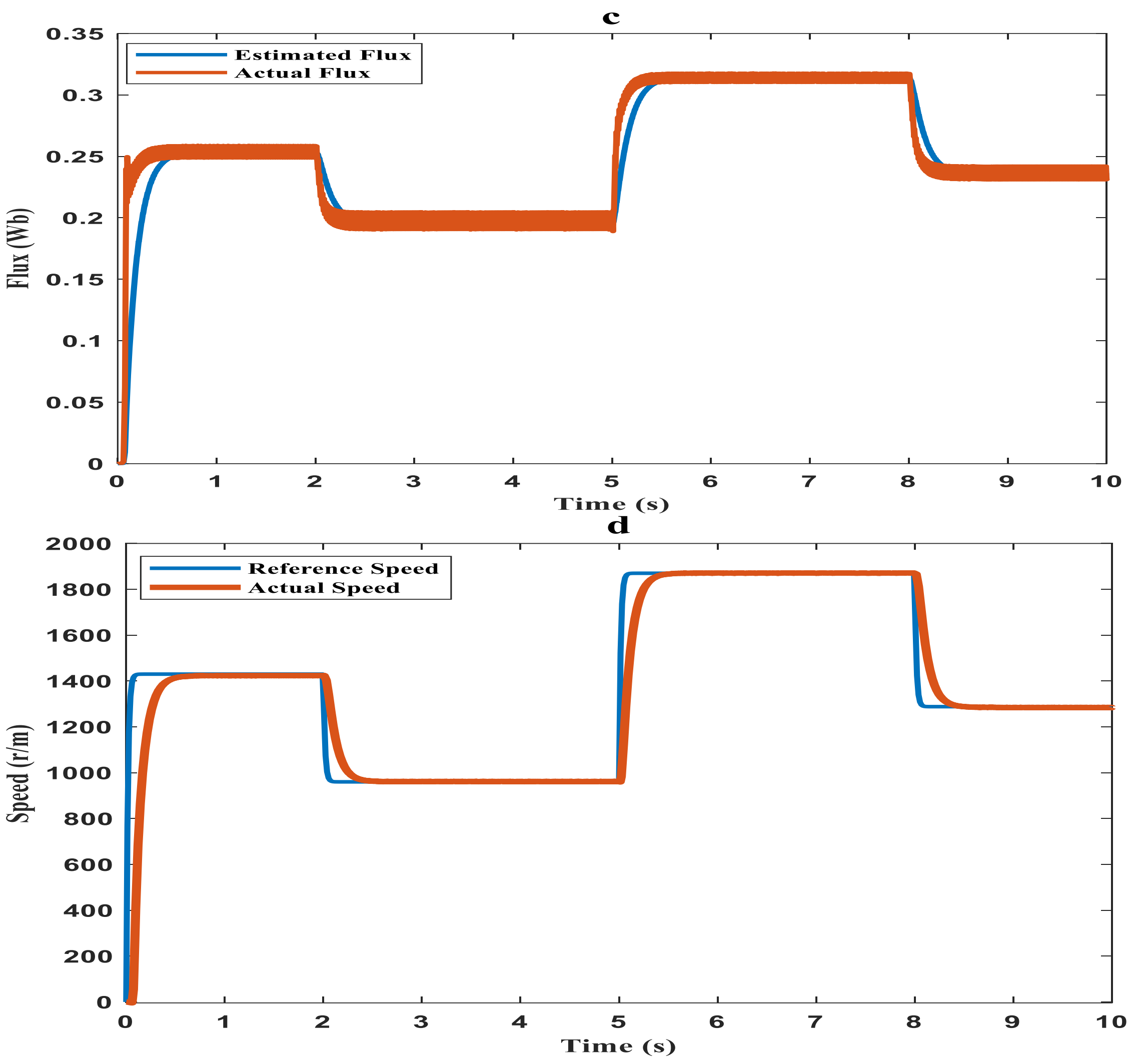

Figure IV.8. The Simulation results of direct Energy and Force control with irradiation 1000 r/m2 and 25° c (a: total torque, b: current, c: flux, d: speed).

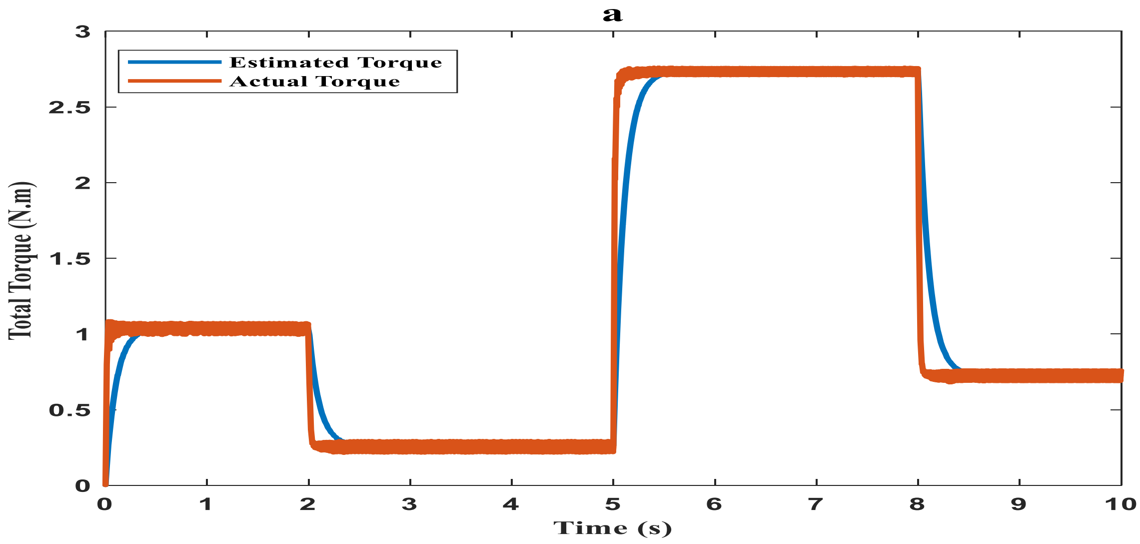

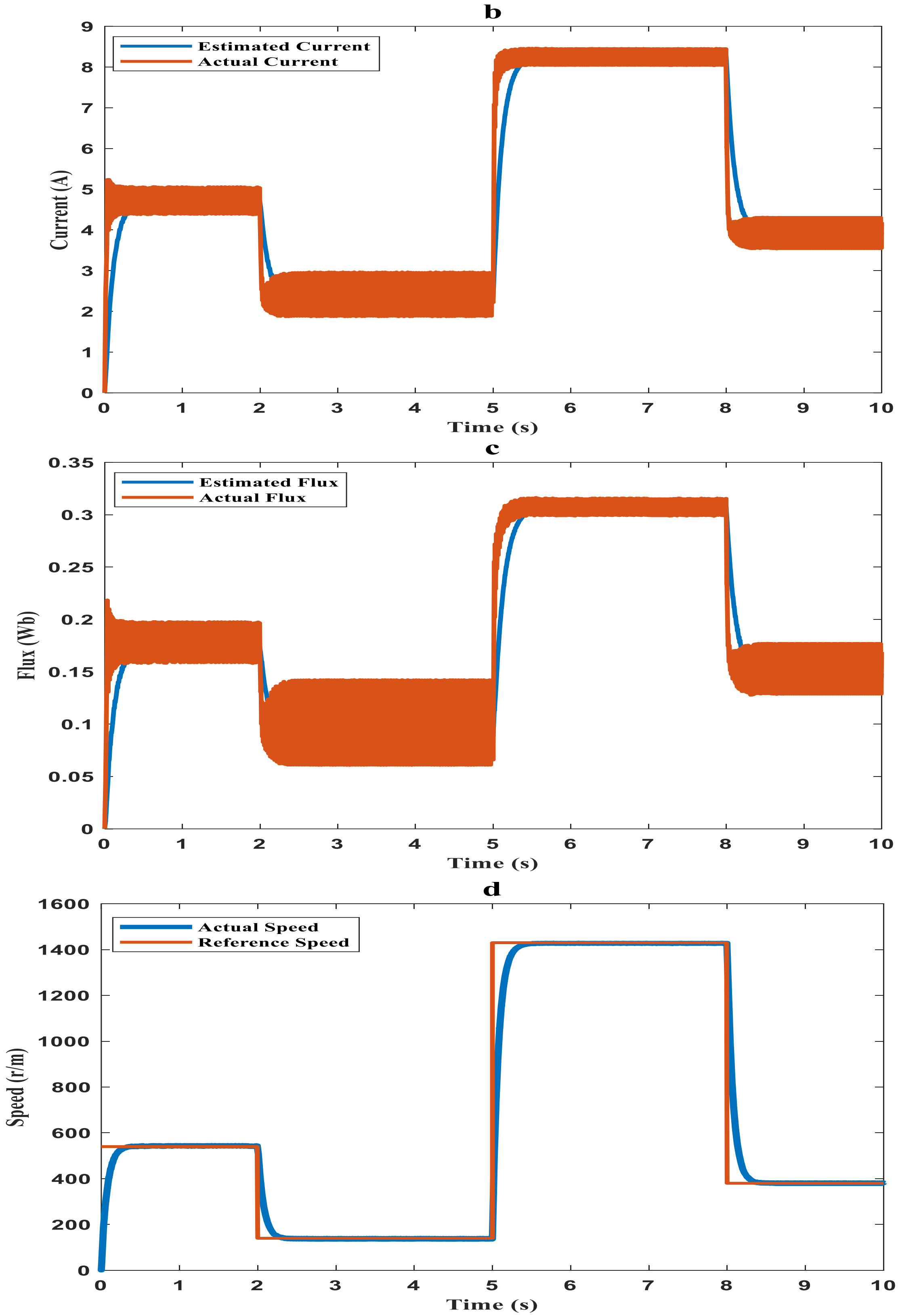

Figure IV.9. The Simulation results of Current control with irradiation 1000 r/m2 and 25° c (a: total torque, b: current, c: flux, d: speed).

In the Direct Torque Control (DTC) approach, the total torque ranged from 1.9 Nm to 3.7 Nm, with flux varying between 0.22 Wb and 0.305 Wb. While the speed closely followed the reference speed, it exhibited slower response times and noticeable torque fluctuations. Conversely, Direct Energy Control (DEC) showed quicker speed tracking with minimal torque ripple compared to DTC.

Under Direct Force Control (DFC), total torque fluctuated between 2 Nm and 3.7 Nm, with flux varying from 0.23 Wb to 0.31 Wb. Speed tracking was comparable to DTC and DEC but with a slightly faster response, albeit not the most efficient in reaching the reference speed, while maintaining a relatively low torque ripple.

In the proposed Direct Energy and Force Control (DEFC) method, total torque ranged from 2 Nm to 3.7 Nm, with flux varying between 0.25 Wb and 0.34 Wb. Notably, speed tracking was highly efficient across all conditions, exhibiting rapid response times and superior performance in reaching reference speeds compared to other methods, offering valuable insights into energy efficiency and magnetic characteristics.

Conversely, in current control, the SRM speed failed to meet reference speeds, dropping significantly to 180 r/m with a noticeable torque ripple. DEFC simulations demonstrated exceptional responsiveness with near-instantaneous response times in the microsecond range, showcasing its adaptability to changing conditions effectively.

IV.2.2.MPPT with load (EV)

In this section, we showcase the simulation results for five distinct control methods: Direct Torque Control (DTC), Direct Energy Control (DEC), Direct Force Control (DFC), our proposed method, Direct Energy and Force Control (DEFC), and current control. The performance metrics under scrutiny include total torque, flux, and speed. These simulations were carried out utilizing the switched reluctance motor (SRM) tailored for application in electric vehicles (EVs). The initial conditions imposed on the system involved an irradiation level of 1000 W/m2 and a temperature of 25°C.

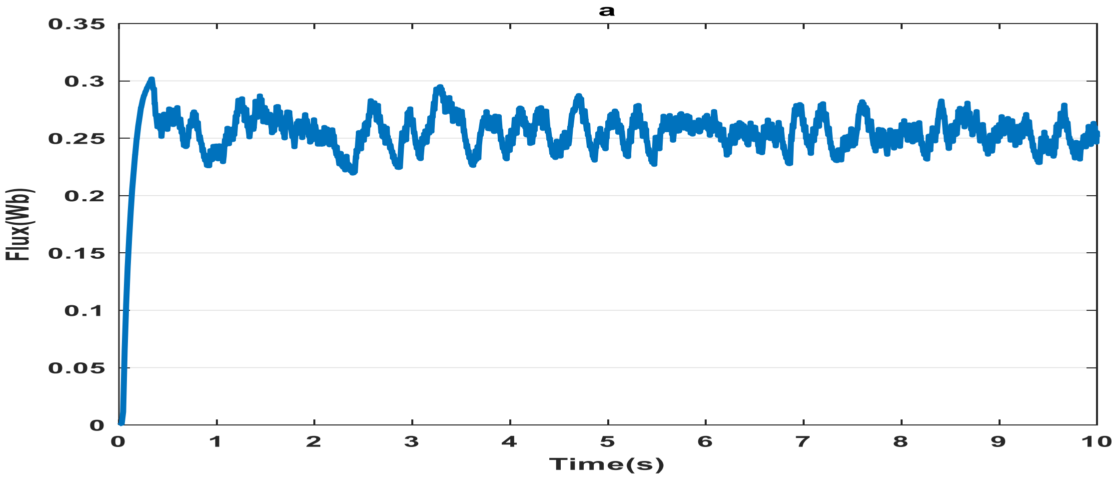

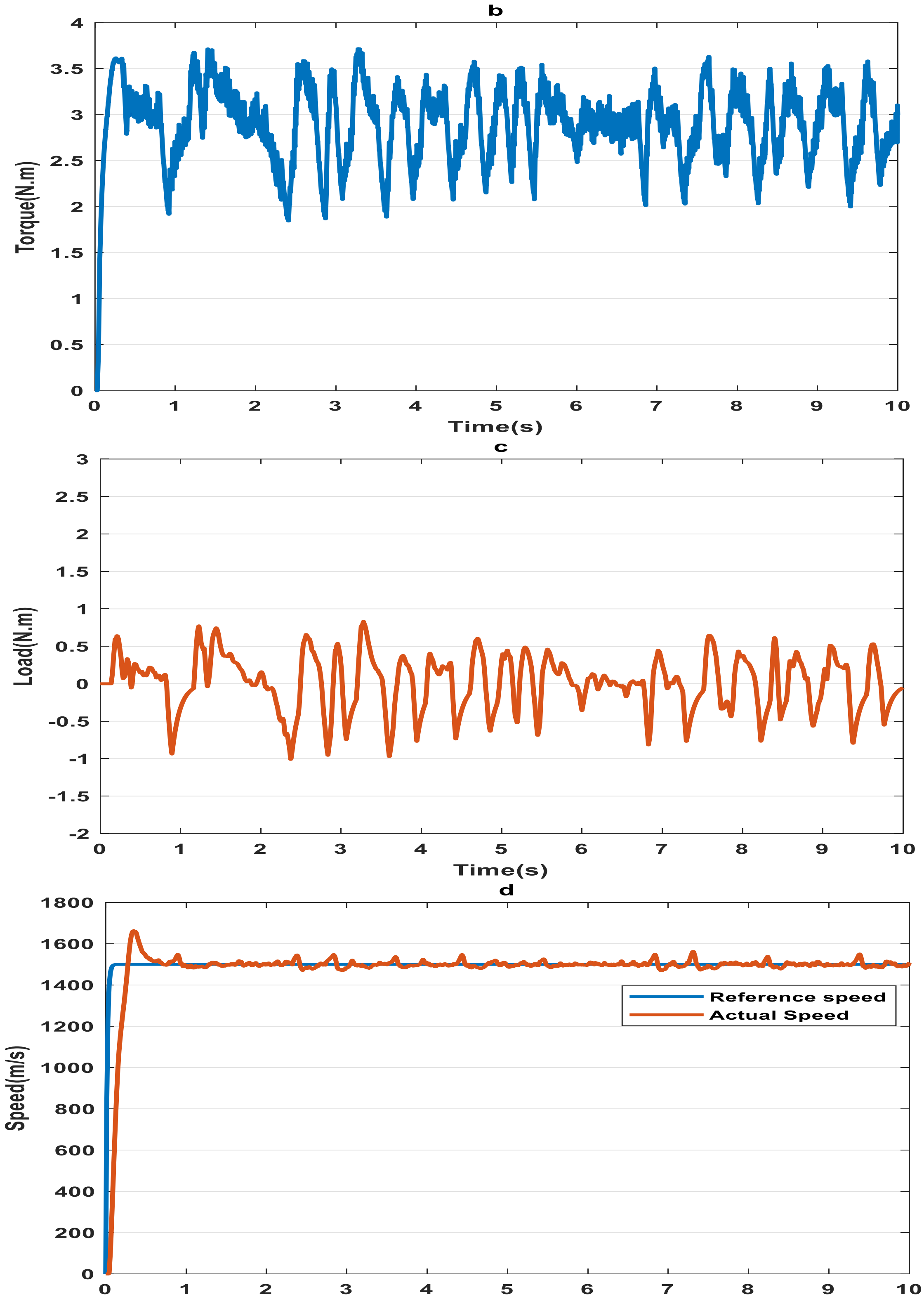

Figure IV.10. The Simulation results of direct torque control applied for Electric vehicles with 1000 w/m2 and 25° c (a: Flux, b: Torque, c: Load, d: speed).

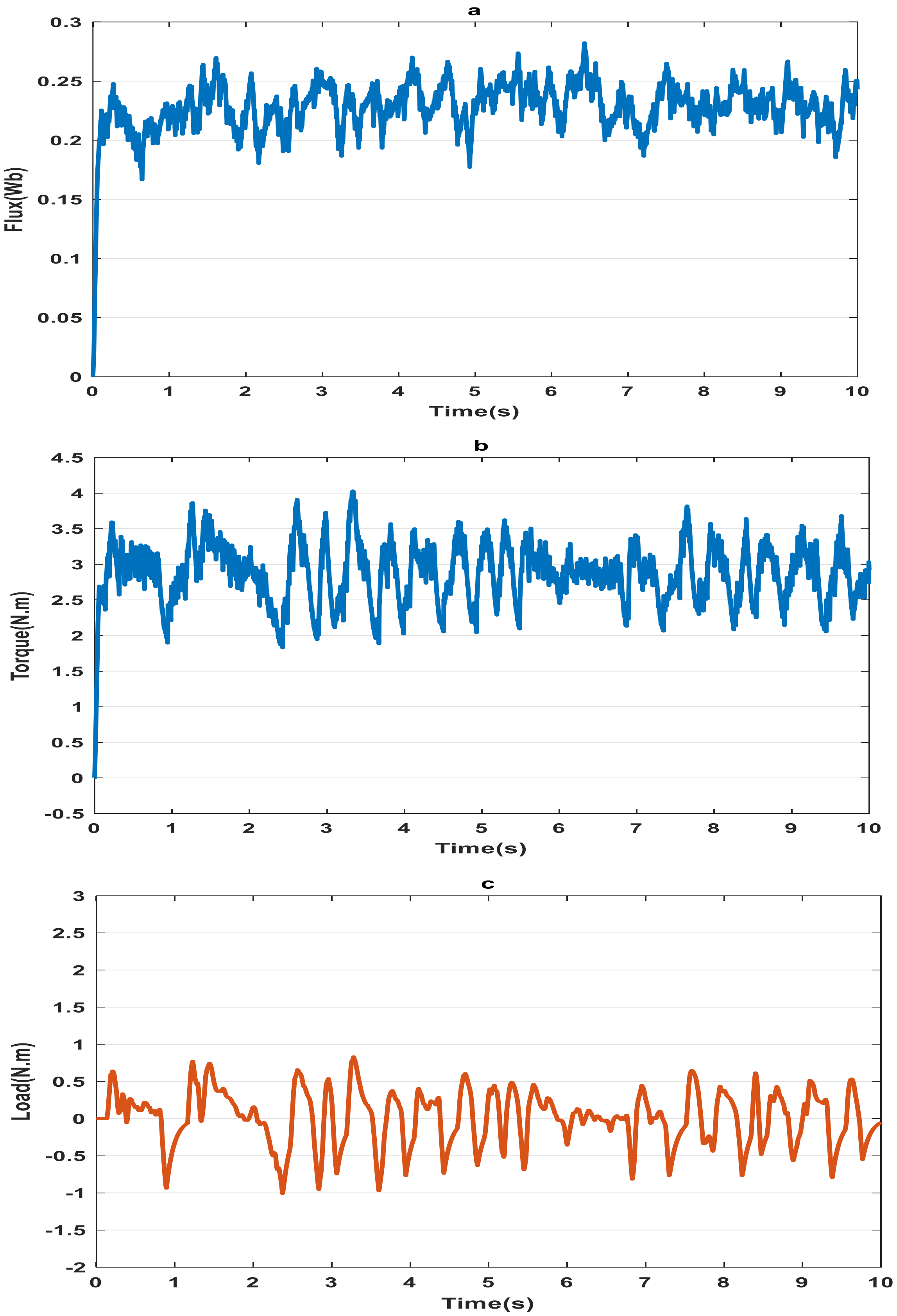
a
Flux(Wb)
0.3
0.25
0.2
0.15
0.1
0.05
0
0
1
2
3
4
5
6
7
8
9
10
Time(s)
b
Torque(N.m)
4.5
4
3.5
3
2.5
2
1.5
1
0.5
0
-0.5
0
1
2
3
4
5
6
7
8
9
10
Time(s)
c
Load(N.m)
3
2.5
2
1.5
1
0.5
0
-0.5
-1
-1.5
-2
0
1
2
3
4
5
6
7
8
9
10
Time(s)

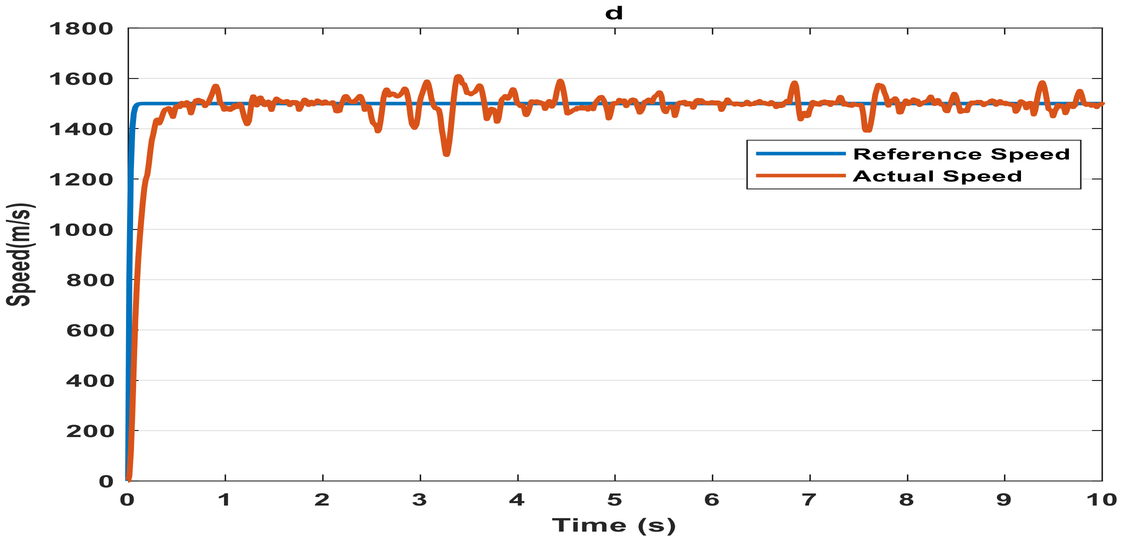

Figure IV.11. The Simulation results of direct force control applied for Electric vehicles with 1000 w/m2 and 25° c (a: Flux, b: Torque, c: Load, d: speed).

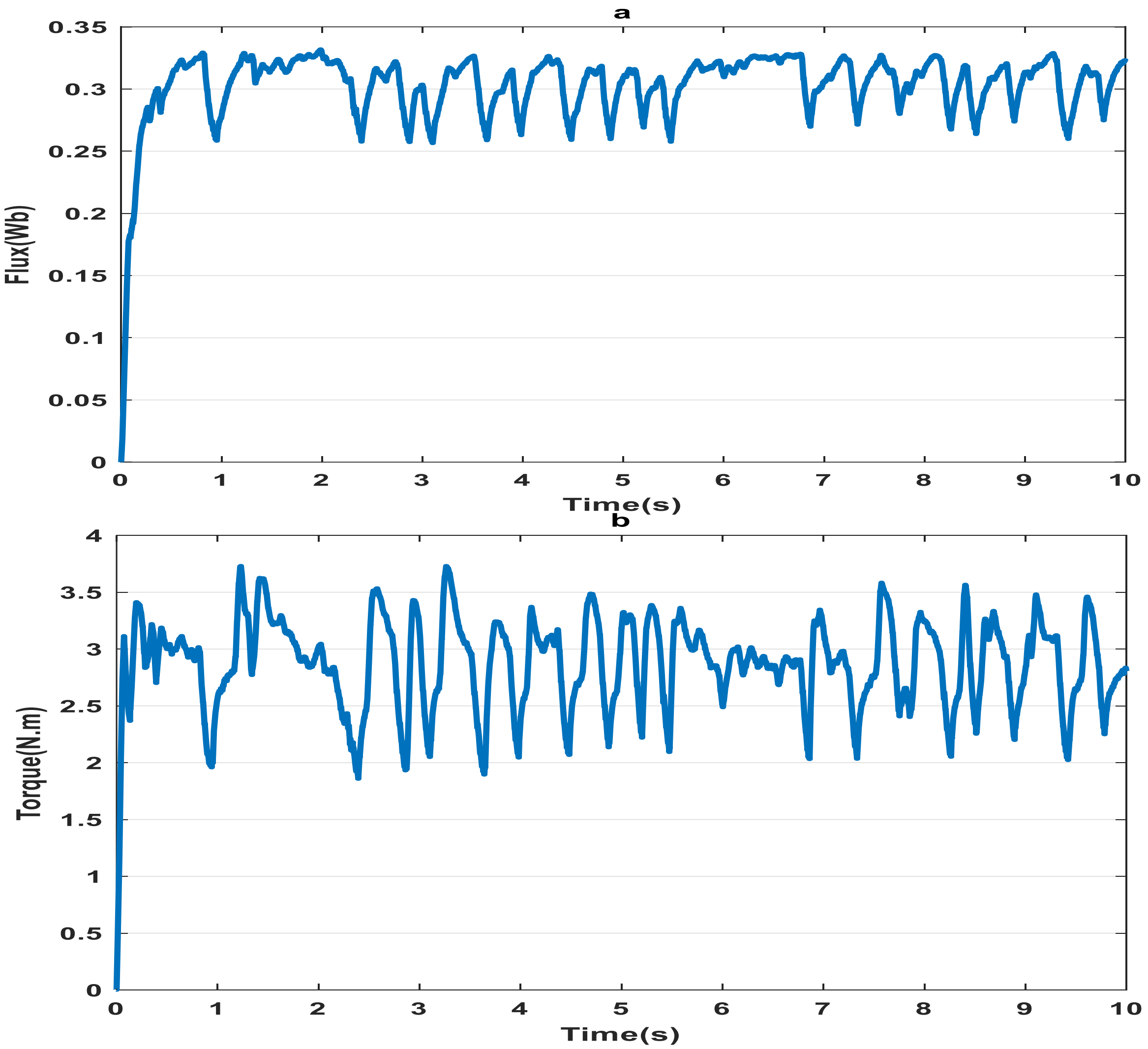

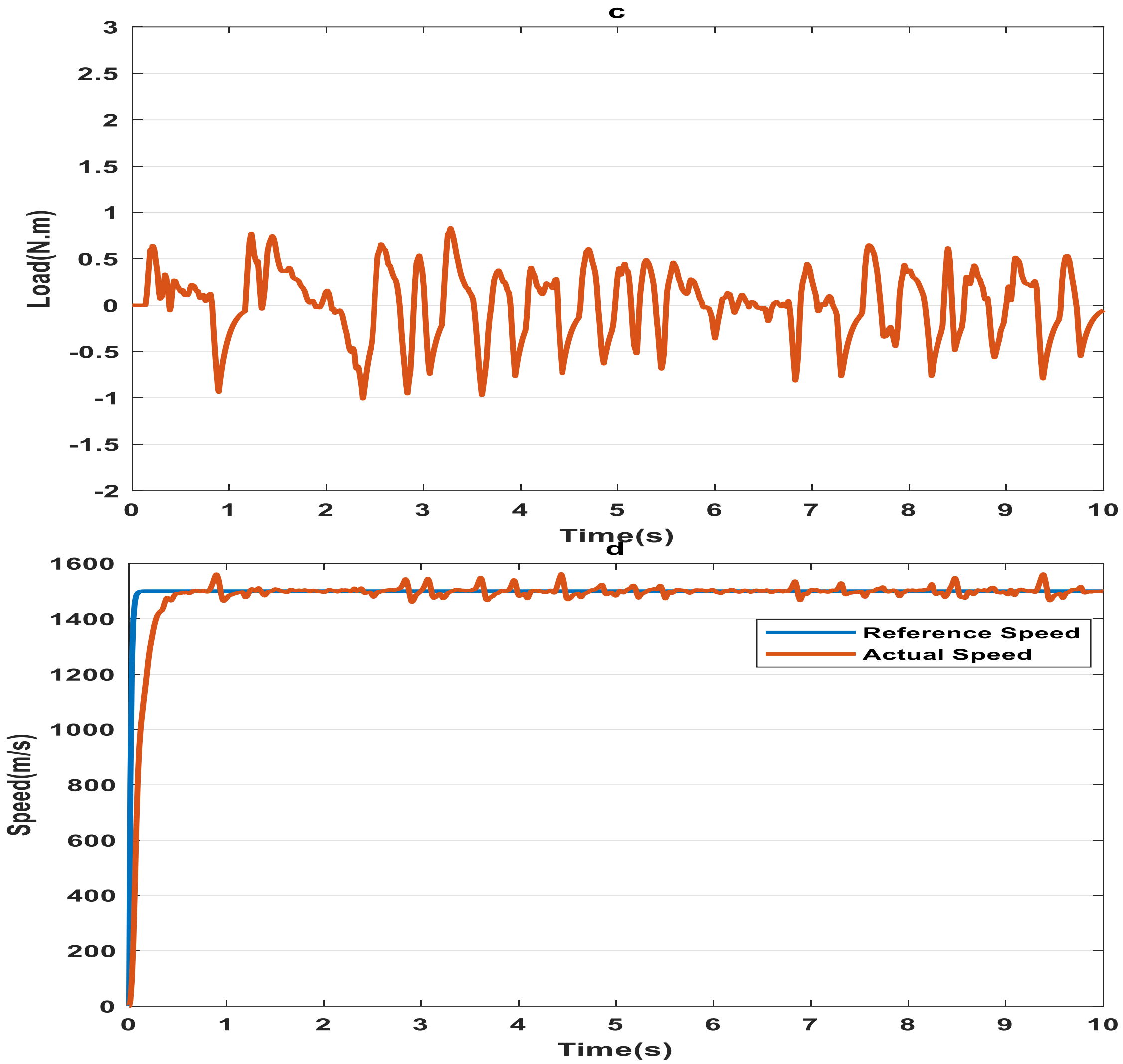

Figure IV.12. The Simulation results of direct energy control applied for Electric vehicles with 1000 w/m2 and 25° c (a: Flux, b: Torque, c: Load, d: speed).

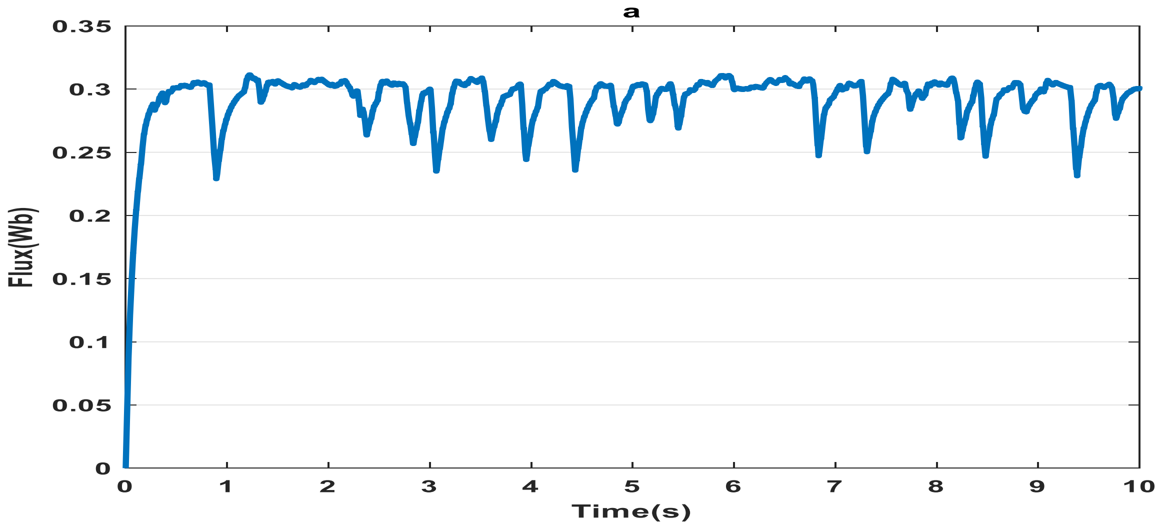

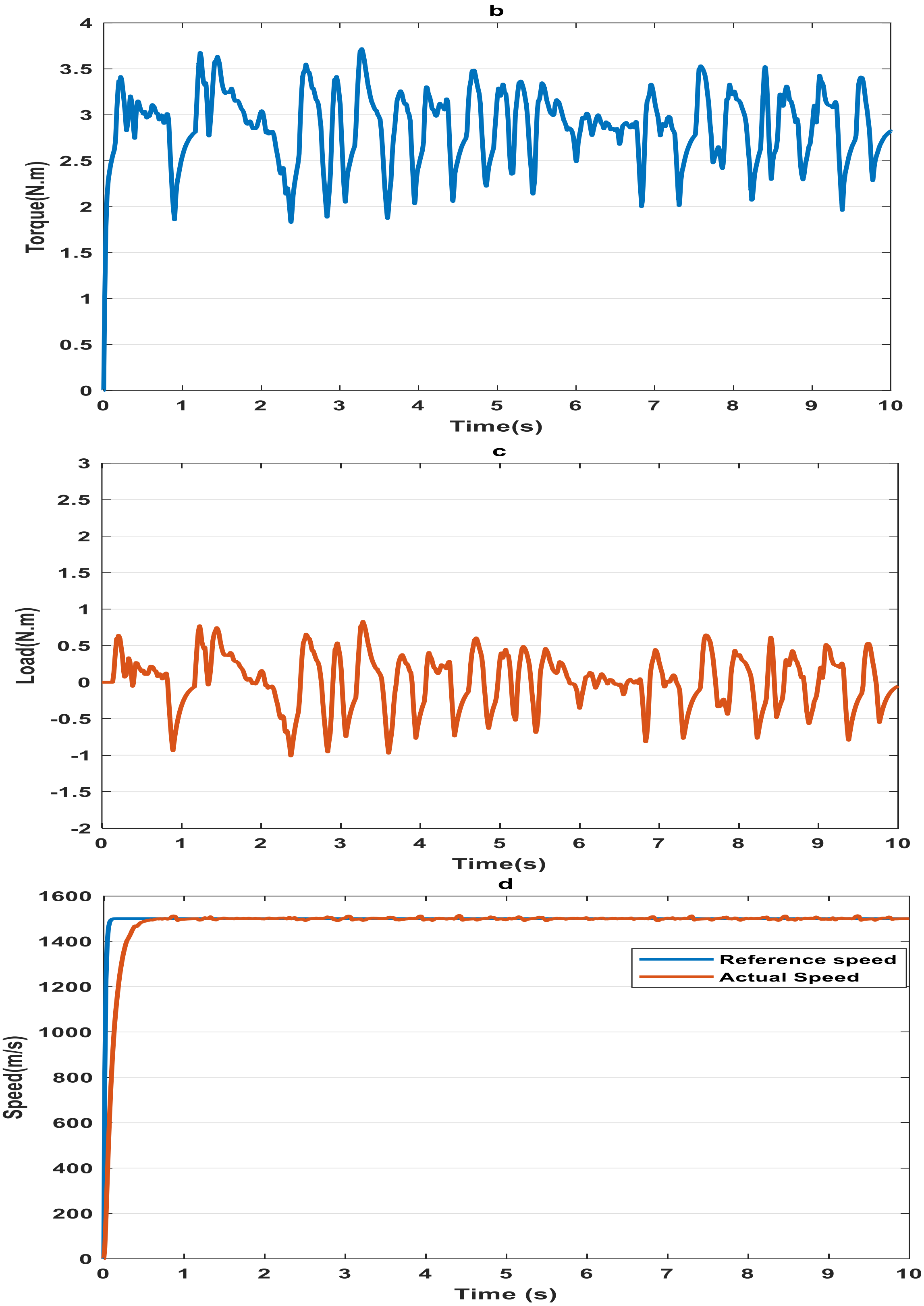

Figure IV.13. The Simulation results of direct energy and force control applied for Electric vehicles with 1000 w/m2 and 25° c (a: Flux, b: Torque, c: Load, d: speed).

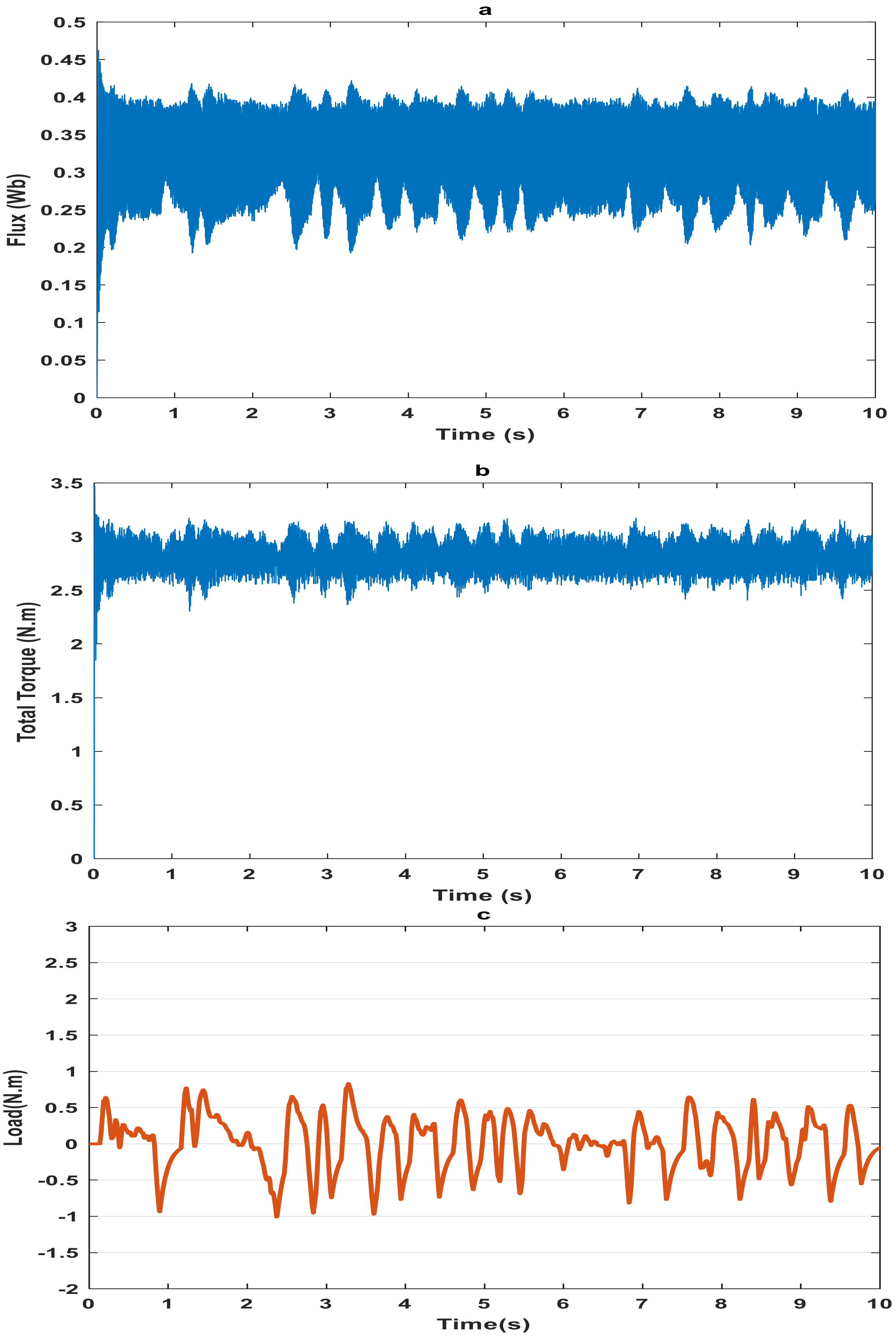
a
Flux (Wb)
0
0.05
0.1
0.15
0.2
0.25
0.3
0.35
0.4
0.45
0.5
Time (s)
0
1
2
3
4
5
6
7
8
9
10
b
Total Torque (N.m)
0
0.5
1
1.5
2
2.5
3
3.5
Time (s)
0
1
2
3
4
5
6
7
8
9
10
c
Load(N.m)
-2
-1.5
-1
-0.5
0
0.5
1
1.5
2
2.5
3
Time(s)
0
1
2
3
4
5
6
7
8
9
10

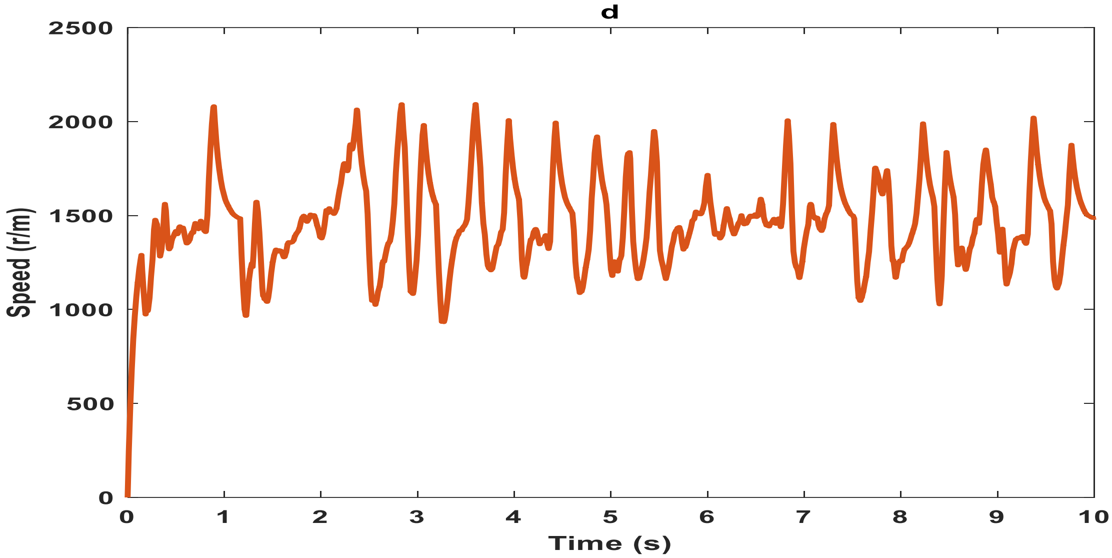

Figure IV.14. The Simulation results of current control applied for Electric vehicles with 1000 w/m2 and 25° c (a: Flux, b: Torque, c: Load, d: speed).

This section outlines the results of simulations conducted for four distinctive control methodologies: Direct Torque Control (DTC), Direct Energy Control (DEC), Direct Force Control (DFC), and our proposed approach, Direct Energy and Force Control (DEFC). The assessment includes key performance metrics such as total torque, electric vehicle load dynamics, flux, and speed. The simulations were executed using a switched reluctance motor (SRM) at a constant reference speed of 1500 r/min for each control method. Initially, the system was subjected to specific conditions, including a radiation level of 1000 W/m² and a temperature of 25°C.

Under the DTC approach, the total torque ranged between 1.9 and 3.7 Nm, with flux variations from 0.22 Wb to 0.305 Wb. The speed tracked the reference speed, albeit with a slower response and noticeable torque ripple. For the DEC method, the introduction of the electric vehicle load led to flux variations between 0.17 Wb and 0.28 Wb, resulting in a sudden shift in total torque from 1.8 Nm to 4 Nm. The speed successfully tracked the reference speed, exhibiting a quicker response compared to DTC, albeit without optimal performance in reaching the reference speed and minimal torque ripple.

In the case of DFC, the total torque varied between 2 Nm and 3.7 Nm under load conditions, and flux experienced variations between 0.23 Wb and 0.31 Wb, with speed successfully tracking the reference speed despite the load. However, its response, while somewhat quicker, was not the most efficient in reaching the reference speed. Additionally, the torque ripple for DFC was relatively small, comparable to DTC and DEC.

For the proposed method, DEFC, the total torque initially measured 2 Nm and changed to 3.7 Nm with altered load conditions. The flux exhibited variations between 0.25 Wb and 0.34 Wb. Crucially, the speed effectively tracked the reference speed under load conditions, displaying a fast response and optimal performance in reaching the reference speed compared to other methods. These parameters provide crucial insights for assessing the motor's energy efficiency and magnetic characteristics under DEFC. In the current control, ripple significantly increased in speed, with notable ripple in torque.

The DEFC simulation demonstrated exceptional responsiveness, with near-instantaneous response times in the microsecond range, enabling swift adaptation to changes in load conditions. These findings hold significant implications for the implementation of DEFC in electric vehicle (EV) systems, where its superior responsiveness and dynamic performance can contribute to enhanced driving experiences, improved energy efficiency, and superior overall system performance. By swiftly adapting to changes in torque and speed, DEFC can optimize motor performance, reduce energy consumption, and provide precise control, thereby enhancing vehicle handling and stability.

Conclusion

In conclusion, this paper has introduced the innovative Direct Force and Energy Control (DEFC) method, emphasizing its integration with photovoltaic (PV) systems in electric vehicles (EVs). The study has provided valuable insights into the understanding and potential application of DEFC within the realm of EV systems. The primary goal of DEFC is to address the challenges of torque ripple and vibration in Switched Reluctance Motors (SRMs), as these factors significantly impact the motor's efficiency and performance. In contrast to traditional Direct Torque Control (DTC), DEFC employs a dual control strategy addressing both force and energy, presenting a more effective approach to mitigating torque ripple and associated vibrations.

The simulations conducted throughout the study consistently demonstrated DEFC's capability to achieve a remarkably low torque ripple of approximately 10%. This substantial reduction underscores the robustness of DEFC in enhancing the motor's operational efficiency and mitigating vibrations. The contributions of this research extend to a deeper understanding and prospective implementation of DEFC in EV systems, ultimately benefiting the automotive industry and advancing the cause of sustainable transportation.

Introduction

Switched reluctance motors (SRMs) are increasingly recognized for their robustness and simplicity, making them suitable for a wide range of applications. This study focuses on the hysteresis control method, renowned for its straightforward implementation and effectiveness in current regulation, to enhance the performance of SRMs. This chapter delineates the experimental methods and procedures employed to investigate the application of hysteresis control in SRMs. The primary objectives are to assess performance improvements in terms of torque ripple reduction, efficiency, and dynamic response, and to validate the hypothesis that hysteresis control can significantly enhance SRM performance under varying operational conditions.

The hysteresis control method operates by continuously monitoring the output current and detecting fluctuations. When the output current deviates beyond predetermined threshold levels, a comparator directly switches the control on or off. This approach offers significant advantages, including rapid transient responses due to the direct control by the comparator and the elimination of the need for phase compensation.

V.1. System under study

This chapter details the development of an experimental platform for Switched Reluctance Motor (SRM) training, created at the Biskra Energy Systems Modelling Laboratory (LESM) (Fig. V.1). The platform comprises a 450 W SRM powered by an H-bridge converter. Rotor position is accurately measured using an encoder, while a grid-connected autotransformer supplies power. Phase currents are monitored with Hall effect current sensors. The control algorithm is implemented on the dSPACE DS1104 board, utilizing Control Desk and MATLAB Simulink software for comprehensive control and analysis.

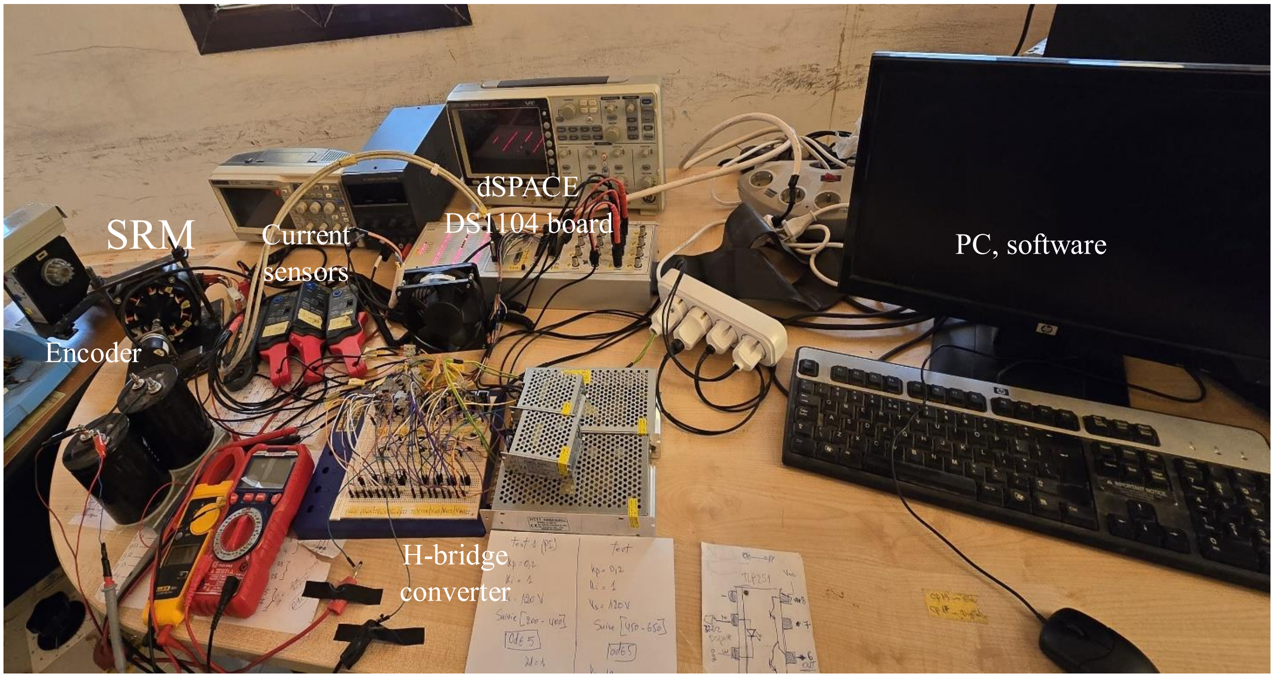

Figure V.1. SRM experimental platform.

V.2. Materials and Methods

V2.1. Switched Reluctance Motor (SRM):

The 6/8 Switched Reluctance Motor (SRM) is a specific type of SRM characterized by its configuration of eight poles on the stator and sex poles on the rotor. This particular configuration is widely adopted in various applications due to its advantageous performance characteristics. In electric vehicles, the 6/8 SRM is valued for its ability to provide high torque at low speeds, which is essential for acceleration and regenerative braking. Additionally, the motor's high efficiency across a broad range of operating conditions contributes to extended driving range and energy savings.

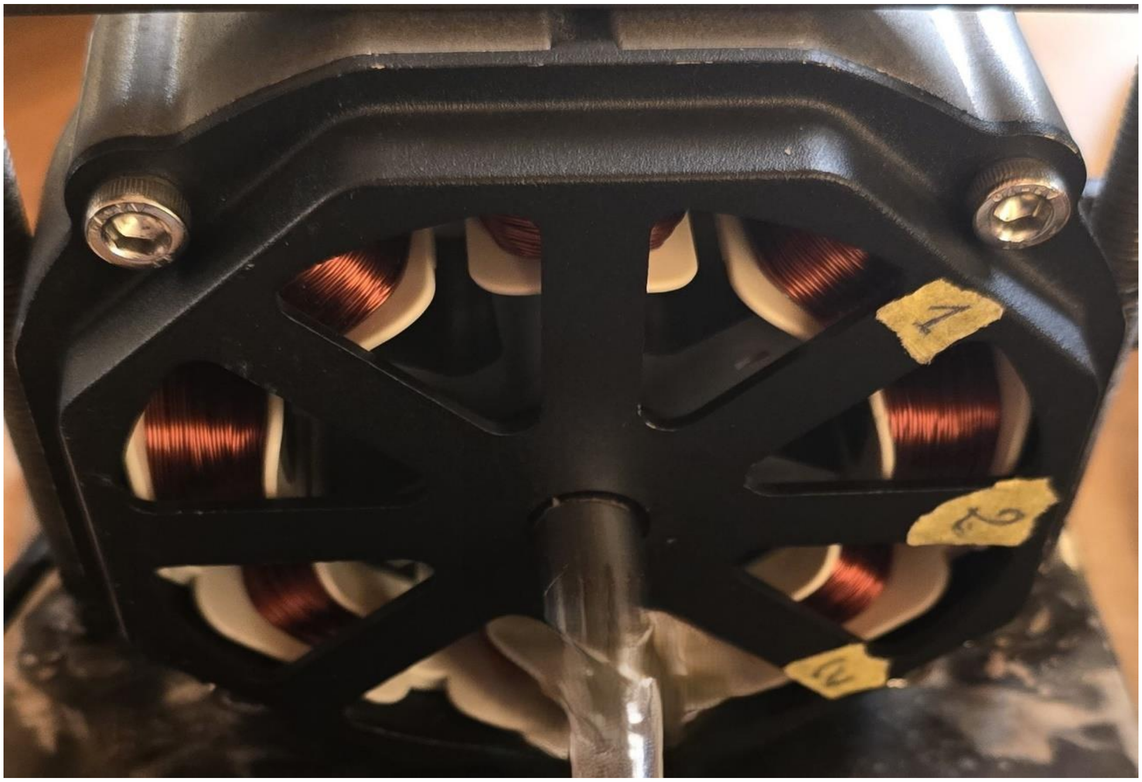

Figure V.2. Switched Reluctance Motor 6/8.

Table V.1 illustrates the dimensions data of the 6/8 switched reluctance motor.

Parameter	Measuring unit	value
Number of stator poles	/	8
Number of rotor poles	/	6
Arc pole of stator	°	18.9
Arc pole of rotor	°	23.5
External rotor radius	mm	30
Internal radius of rotor	mm	16

External radius of stator	mm	60
Internal radius of stator	mm	10
Speed	RPM	40-10500
Current rated	A	4
Torque	N.m	2

V.2.2. Power Electronics:

An H-bridge inverter is a power electronic converter designed to convert DC power (a grid-connected autotransformer) into AC power. It is widely utilized in diverse applications, such as motor drives, power supplies, and renewable energy systems. The H-bridge inverter features eight power electronic switches, typically MOSFETs or IGBTs, arranged in a bridge configuration. This setup enables the inverter to generate a high-frequency AC output, offering precise control over the output voltage and current, which is essential for optimizing performance and efficiency in various electronic systems.

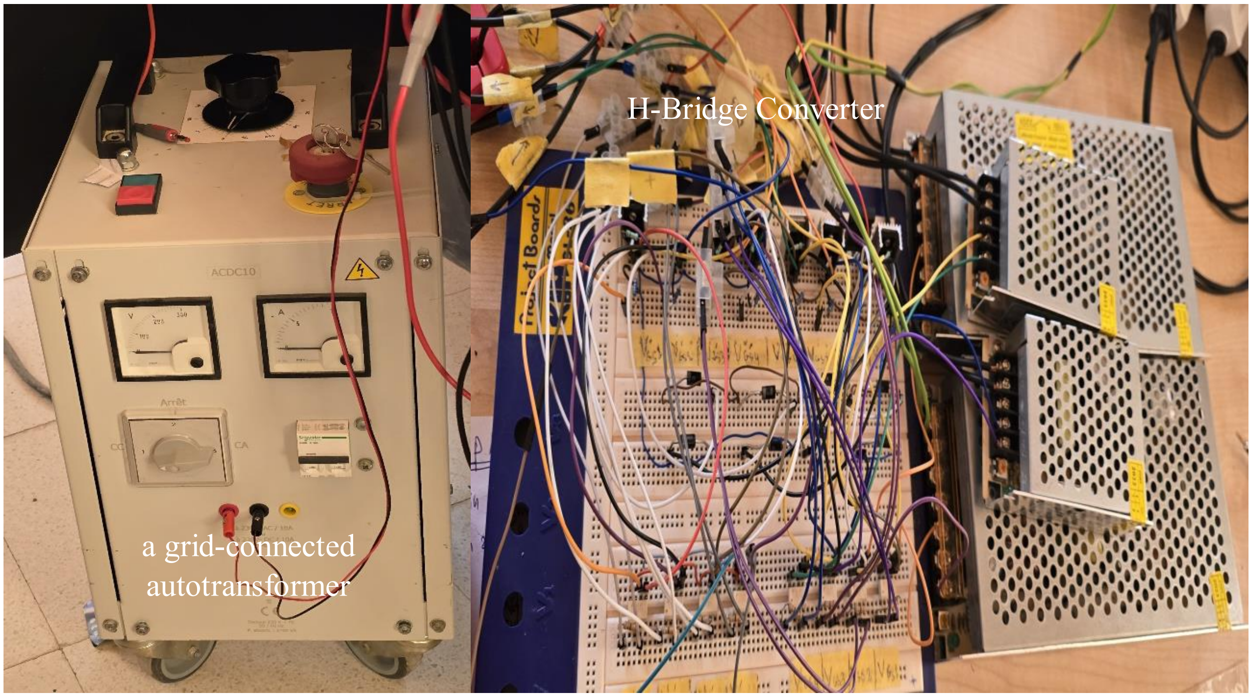

Figure V.3. The power supply powered the H-bridge converter.

V.2.3. Control Hardware:

The DS1104 R&D Controller Board is a powerful and versatile tool designed for controller development and rapid control prototyping. With its comprehensive set of I/O interfaces, high-performance processing capabilities, and user-friendly design, it is an ideal solution for controlling the switched reluctance motor (SRM).

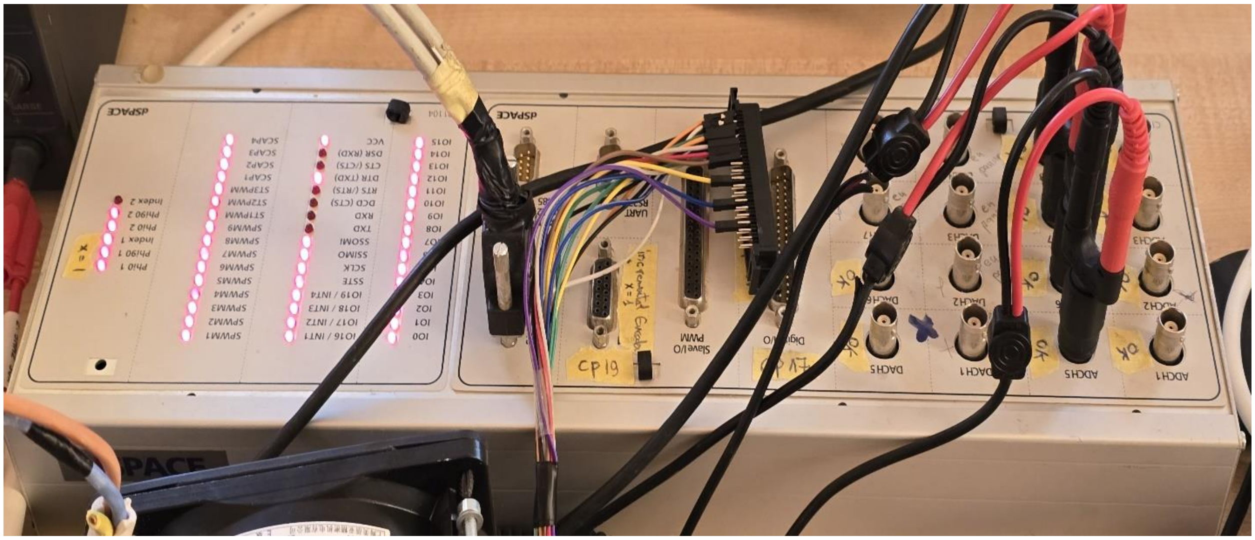

Figure V.4. the dSPACE DS1104 board.

Sensors:

effect current sensors, specifically the LANGLOIS DCA60 model, were employed for precise measurement of phase currents. Additionally, optical encoders from LIKA were utilized for accurate position sensing of the switched reluctance motor.

Figure V.5.The optical encoders from LIKA and Current sensors specifically the LANGLOIS DCA60 model.

V.3. Experimental results

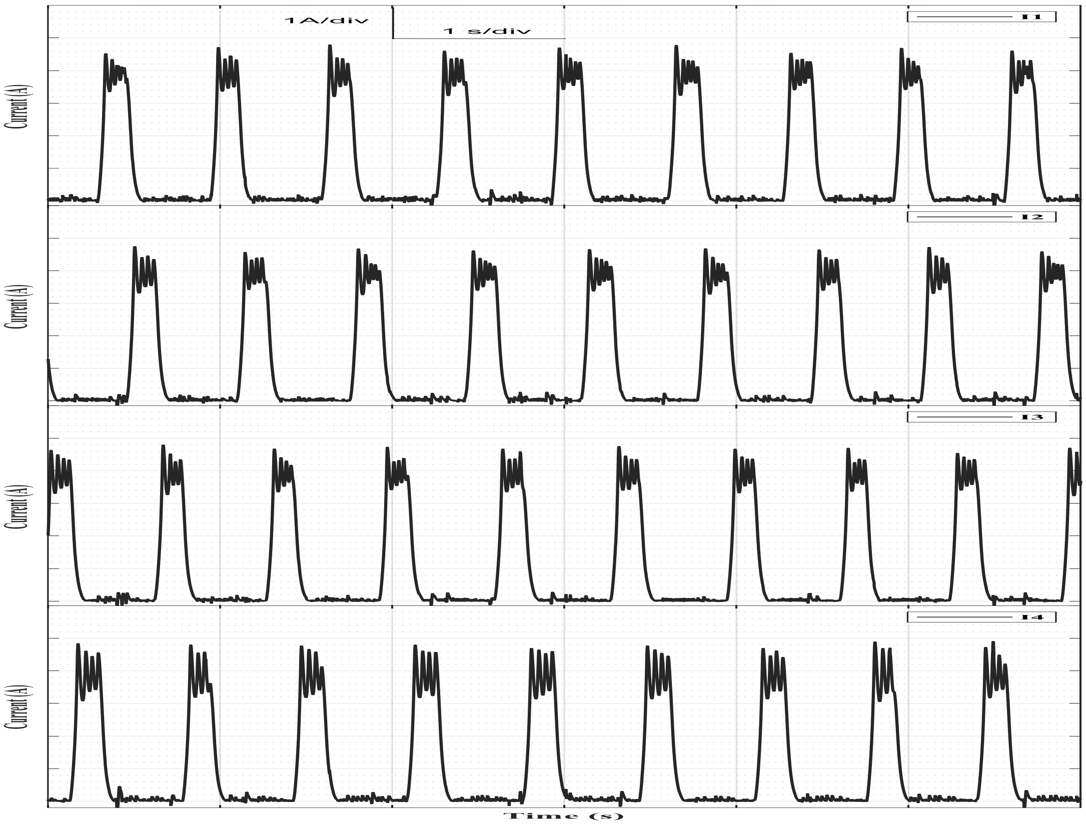
1A/div
1 s/div
I1
I2
I3
I4
Current (A)
Current (A)
Current (A)
Current (A)
Time (s)

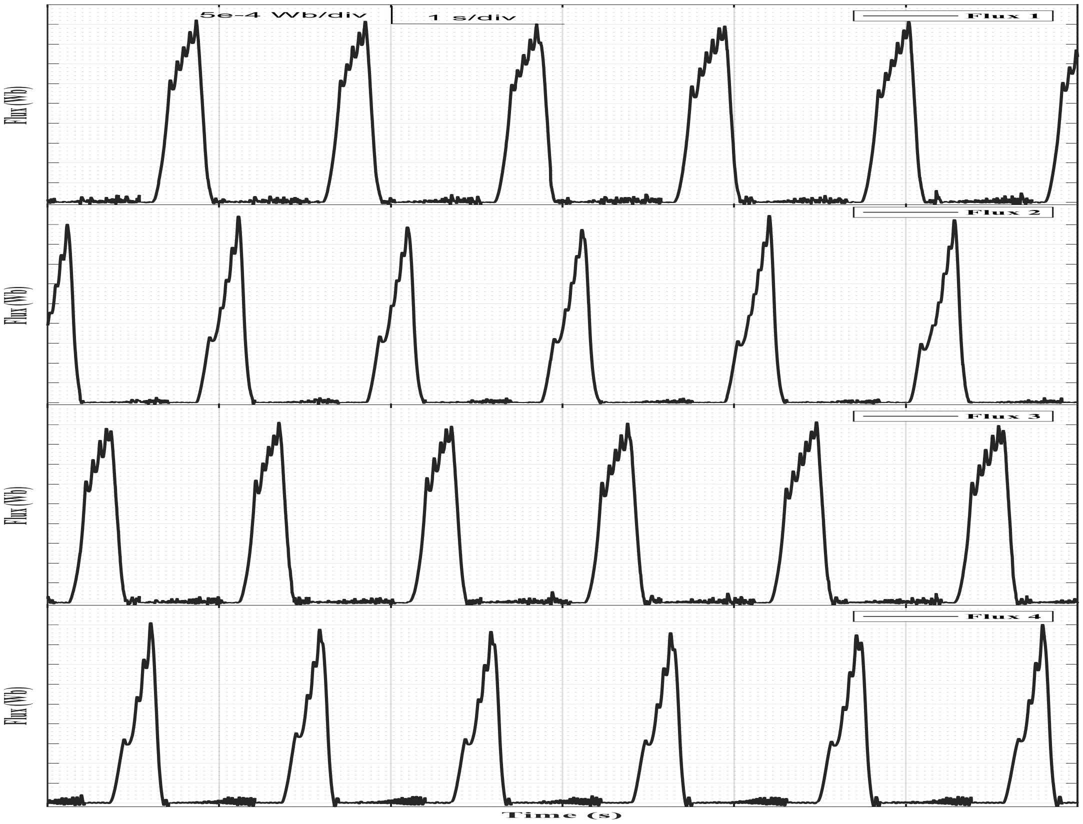
5e-4 Wb/div
1 s/div
Flux 1
Flux 2
Flux 3
Flux 4
Flux (Wb)
Flux (Wb)
Flux (Wb)
Flux (Wb)
Time (s)

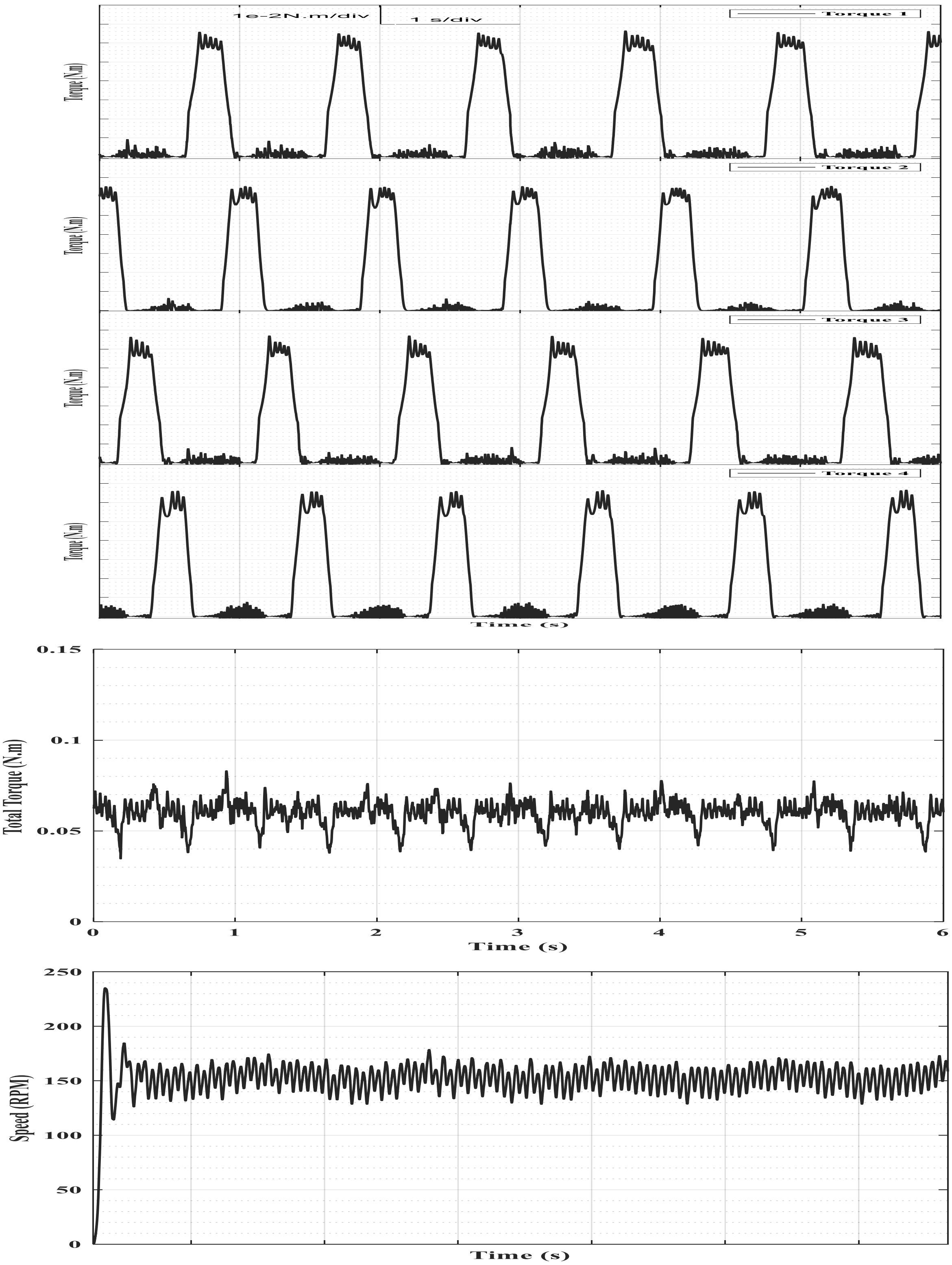

Figure V.6.current , flux , torque , total torque and speed for Iref=2 A

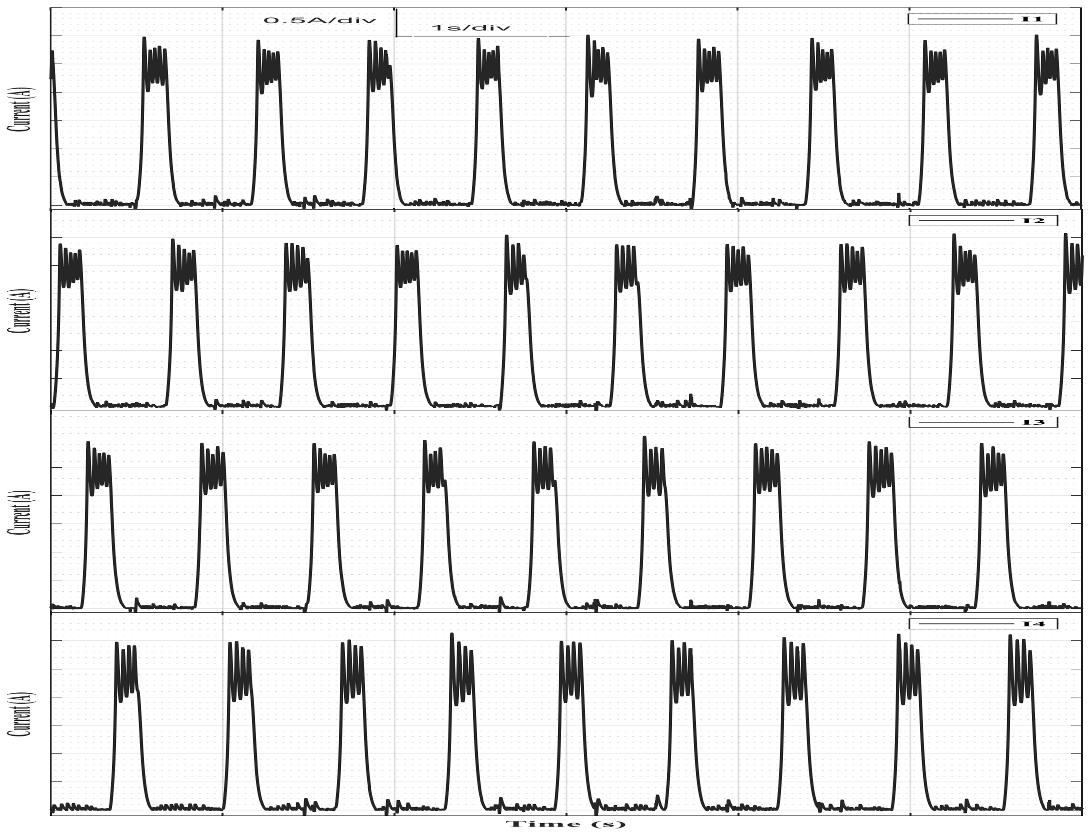
0.5A/div
1s/div
I1
I2
I3
I4
Current (A)
Current (A)
Current (A)
Current (A)
Time (s)

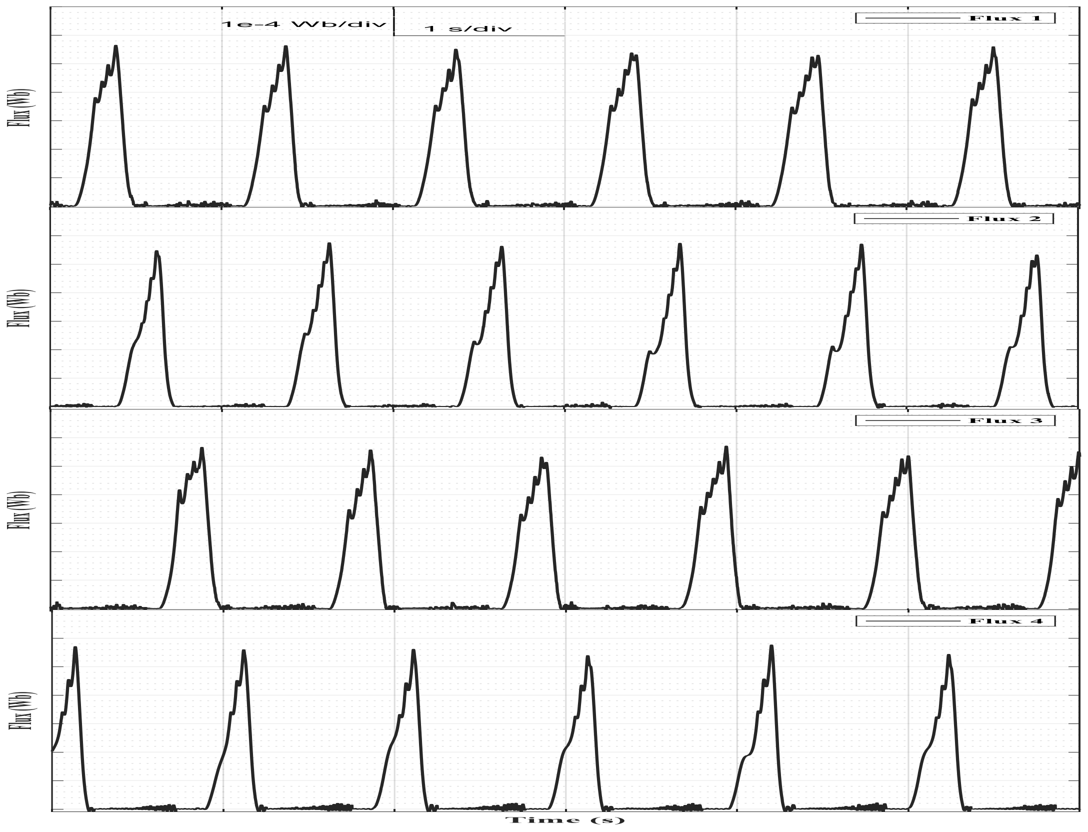
1e-4 Wb/div
1 s/div
Flux 1
Flux 2
Flux 3
Flux 4
Flux (Wb)
Flux (Wb)
Flux (Wb)
Flux (Wb)
Time (s)

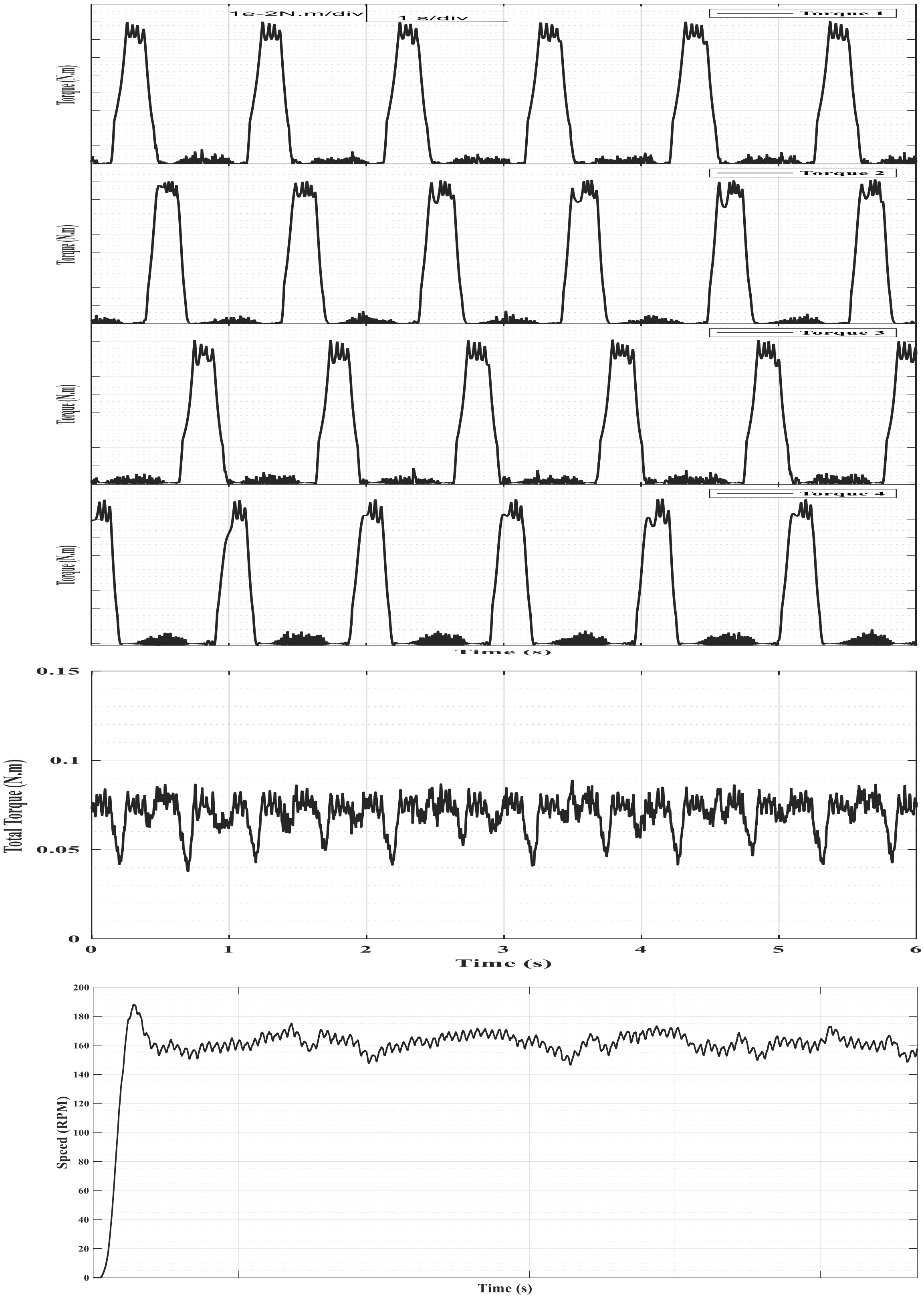

Figure V.6. V.6.current , flux , torque , total torque and speed for Iref=2 .5A

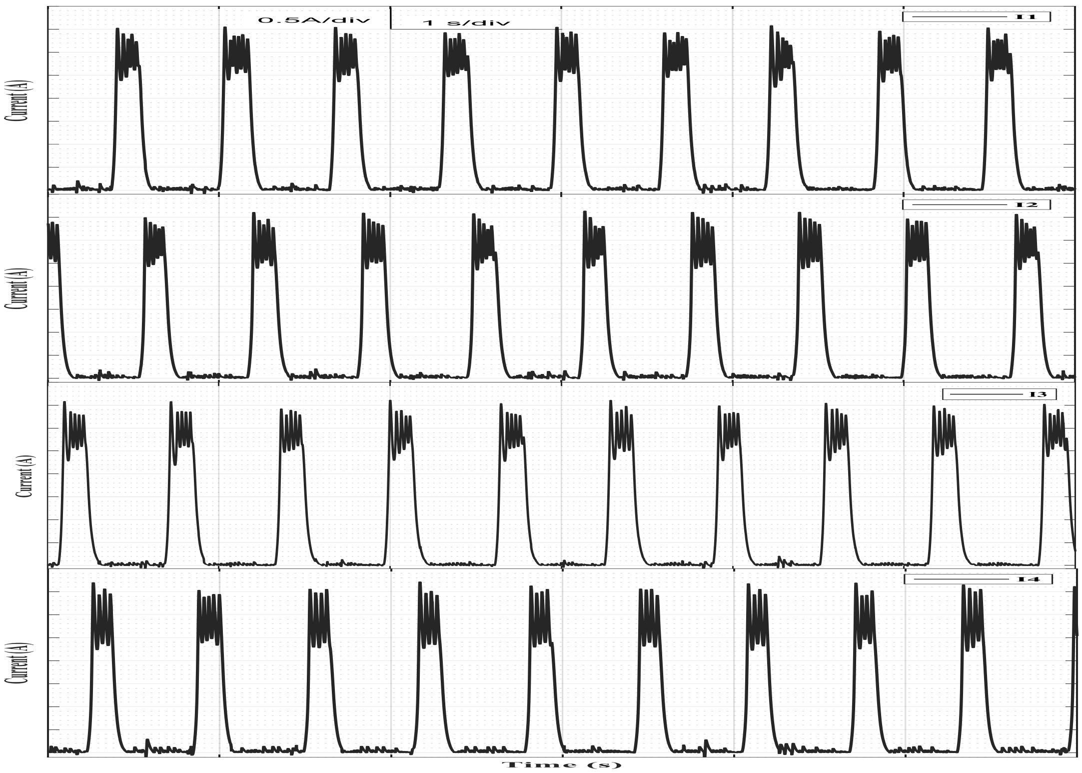
0.5A/div
1 s/div
I1
I2
I3
I4
Current (A)
Current (A)
Current (A)
Current (A)
Time (s)

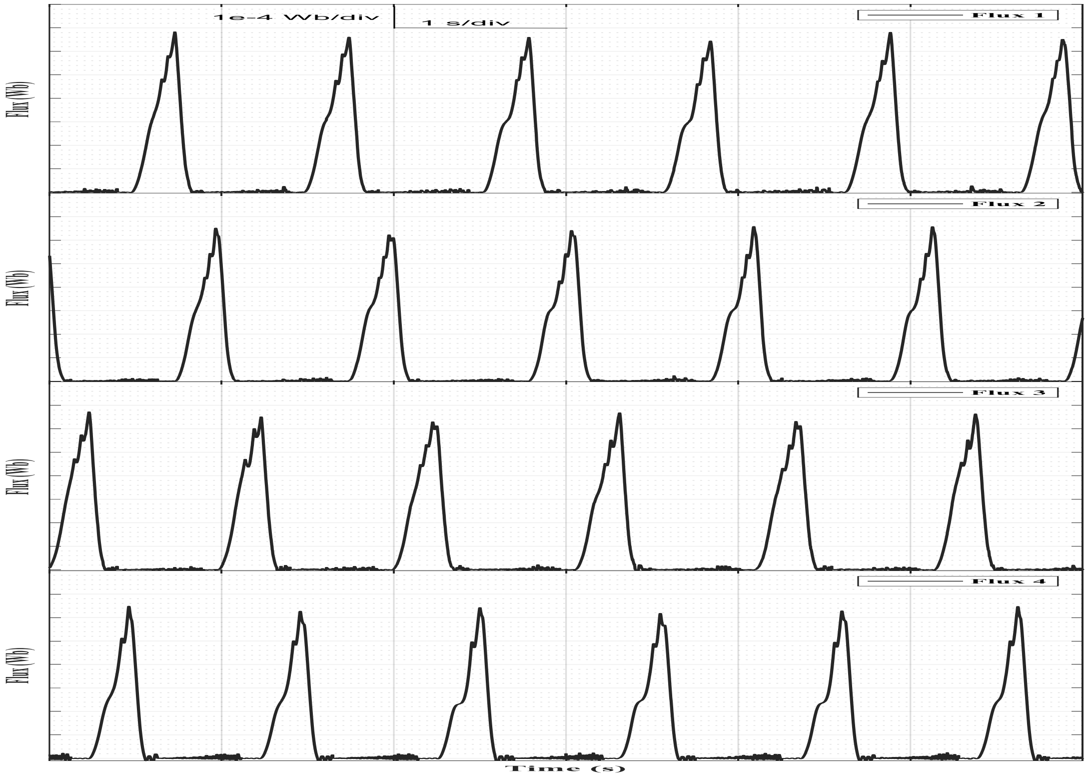
1e-4 Wb/div
1 s/div
Flux 1
Flux 2
Flux 3
Flux 4
Flux (Wb)
Flux (Wb)
Flux (Wb)
Flux (Wb)
Time (s)

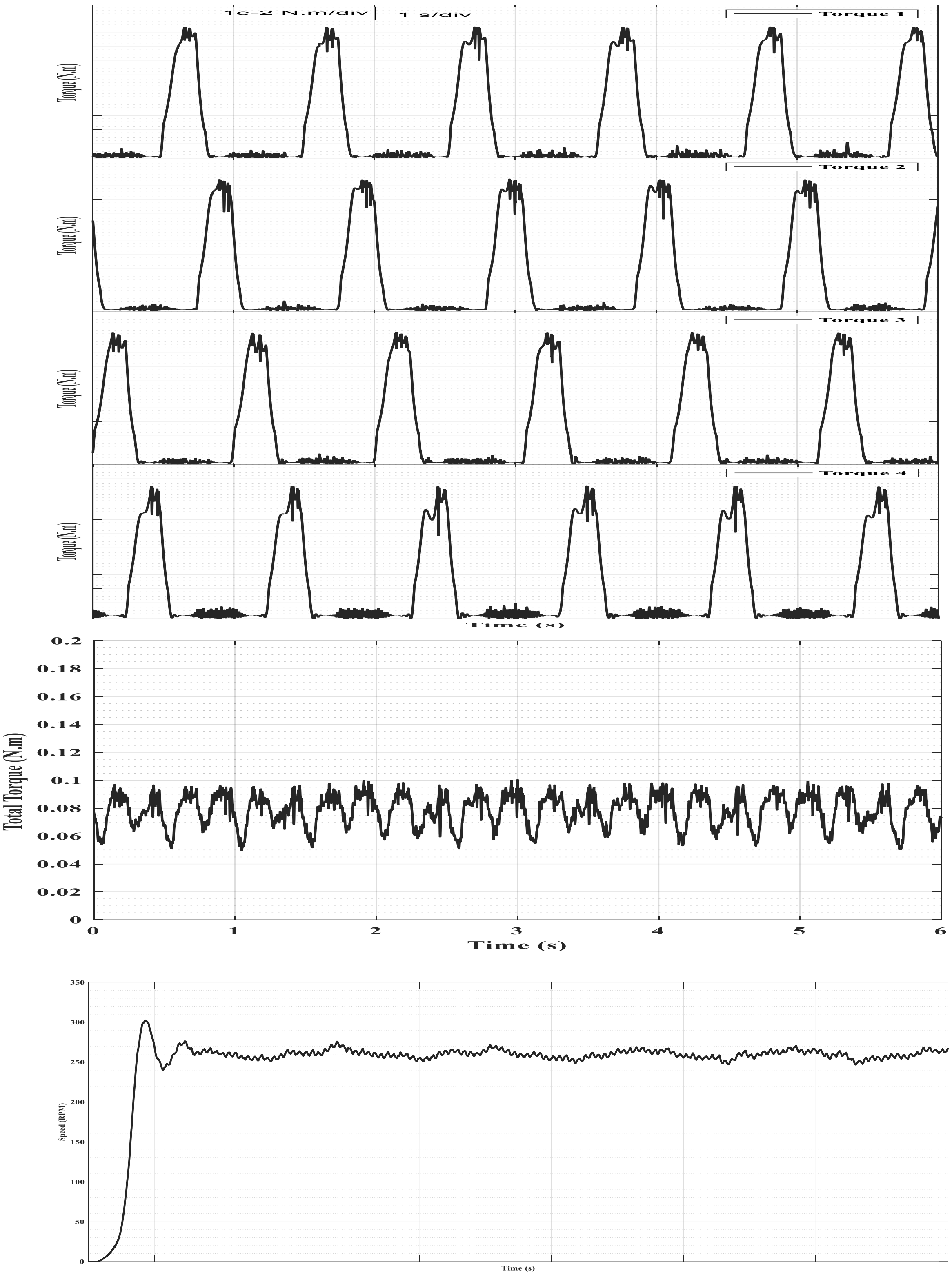

Figure V.7. current , flux , torque , total torque and speed for Iref=3 A

V.3.1 Overview

This section provides a detailed discussion on the experimental application of the hysteresis control algorithm to the 6/8 Switched Reluctance Motor (SRM), tested under varying current reference levels of 2 A, 2.5 A, and 3 A. Real-time measurements of current, flux, torque, and speed were conducted, with each test repeated three times to ensure consistency and repeatability. The key performance metrics evaluated included torque ripple reduction, efficiency enhancement, and dynamic response across different operational conditions. The findings underscore the efficacy of hysteresis control in improving SRM performance.

V.3.1.1 Performance Metrics Evaluation

Current Reference of 2 A:

- Current Tracking: The hysteresis control algorithm successfully maintained the current at the 2 A reference level, demonstrating its ability to accurately follow the desired current profile.
- Flux: The flux reached 0.0045 Wb.
- Torque: The torque achieved was 0.065 N·m.
- Speed: The speed attained was 150 RPM.
- Torque Ripple Reduction: Torque ripple was reduced by approximately 41.66%. This significant reduction highlights the control's capability to maintain stable operation and minimize torque fluctuations even at lower current settings, contributing to smoother motor performance and reduced mechanical stress.

Current Reference of 2.5 A:

- Current Tracking: The control algorithm effectively tracked the 2.5 A reference current, demonstrating consistent current regulation across a moderate power level.
- Flux: The flux reached 0.0058 Wb.
- Torque: The torque achieved was 0.08 N·m.
- Speed: The speed attained was 160 RPM.
- Torque Ripple Reduction: Torque ripple was reduced by approximately 38.46%. This indicates that hysteresis control maintained its efficacy in reducing torque variations at intermediate current levels, thereby enhancing the motor's operational stability and performance.

Current Reference of 3 A:

- Current Tracking: The control algorithm accurately followed the 3 A reference current, showcasing its robustness in managing higher current levels.
- Flux: The flux reached 0.007 Wb.
- Torque: The torque achieved was 0.095 N·m.

- Speed: The speed attained was 250 RPM.
- Torque Ripple Reduction: Torque ripple reduction was observed to be 28.57%. Although the percentage reduction was slightly lower compared to lower current settings, the absolute reduction in torque ripple at higher currents reflects the improved utilization of the SRM's torque-producing capabilities, indicating that hysteresis control effectively enhances performance under high-power conditions.

Conclusion

The experimental analysis of the hysteresis control algorithm on the 6/8 Switched Reluctance Motor (SRM) has provided substantial evidence of its performance advantages across various current reference levels (2 A, 2.5 A, and 3 A). Through detailed measurements of current tracking, flux, torque, speed, and torque ripple reduction under diverse operational conditions, the efficacy of the hysteresis control algorithm was rigorously assessed.

Key findings indicate that the hysteresis control algorithm markedly enhances the performance of the 6/8 SRM. It achieves precise current regulation, effectively reduces torque ripple, and improves both operational stability and efficiency across the tested current ranges. These improvements underscore the algorithm's potential as a robust and effective solution for optimizing SRM performance.

Future research should seek to expand these promising results by exploring a wider range of current settings and different motor configurations. Additionally, integrating advanced control strategies could further amplify the benefits of hysteresis control, offering a broader scope for its application in various high-performance SRM systems.

General conclusion

Before exploring the simulation and experimental analysis outcomes presented in this dissertation, it was crucial to provide a preliminary discussion on the switched reluctance motor (SRM). Although the operational principles of SRMs have long been understood, progress in their development has been hindered by their inherent nonlinearities. However, advancements in modern computational tools now facilitate rapid motor sizing, leading to a proliferation of diverse applications. This dissertation primarily focuses on the systematic modeling and regulation of SRMs through various control methodologies, aiming to establish a control paradigm that optimizes SRM efficiency. The key motivation is to enhance SRM power delivery and mitigate torque ripples through the careful selection of appropriate control techniques. Additionally, this work investigates the feasibility of integrating a photovoltaic (PV) system with an SRM, employing various control strategies for application in electric vehicles (EVs). The dissertation also includes an experimental analysis of the hysteresis control algorithm on a 6/8 SRM.

In the inaugural chapter, a comprehensive overview of the Switched Reluctance Motor (SRM) was provided, elucidating its operational principles, various typologies, and power supply considerations. Additionally, the discussion extended to the photovoltaic (PV) system, covering its control principles.

The succeeding chapter focused on the simulation aspect, utilizing the Finite Element Method Magnetics (FEMM) software with the LUA programming language. Detailed specifications of the SRM, including dimensions, material properties, and boundary conditions, were presented. Key electromagnetic characteristics such as torque, flux, and inductance were analyzed, yielding commendable results that form a pivotal foundation for enhancing the simulation of SRM in conjunction with its power supply, thereby aligning with the second objective. This chapter also addressed the modeling and simulation of the PV system.

Chapter three leveraged the electromagnetic data obtained previously to simulate the SRM and its power supply using MATLAB/SIMULINK. The primary objective was to select an appropriate control method for minimizing torque ripple, evaluating five distinct strategies, both traditional and novel. The proposed Direct Force and Energy Control (DEFC) method, introduced in this chapter, revolutionizes the control paradigm for SRMs. By significantly reducing torque ripple and vibration, DEFC surpasses conventional methods such as Direct Torque Control (DTC) and Direct Force Control, achieving superior efficiency. Rigorous simulations demonstrated DEFC's effectiveness, achieving a torque ripple reduction to approximately 10%, compared to 36% with DTC. DEFC enhances motor performance by simultaneously managing force and energy, rather than torque and flux.

Chapter four validated the integration of a PV system with an SRM, controlled by various methods for Electric Vehicles (EVs). Integration with Maximum Power Point Tracking (MPPT) provided substantial benefits, including reduced torque ripple, increased motor efficiency, and overall system performance enhancement. The study examined the impact of radiation on system operation, confirming the proposed PV system's resilience under low radiation conditions. Comparative analysis highlighted DEFC's superior stability across varying radiation levels, underscoring its efficacy in improving overall system performance and ensuring operational steadiness. This investigation significantly contributes to the understanding and implementation of DEFC in EV systems, promoting advancements in sustainable transportation within the automotive industry.

Chapter five presents the experimental analysis of the hysteresis control algorithm on a 6/8 SRM, providing substantial evidence of its performance advantages across various current reference levels. Through detailed measurements of current tracking, flux, torque, speed, and torque ripple reduction under diverse operational conditions, the efficacy of the hysteresis control algorithm was rigorously assessed.

References

[1] *Abdel-Salam, Mazen, El-Mohandes, Mohamed Tharwat et Goda, Mohamed. (2018). An improved perturb-and-observe based MPPT method for PV systems under varying irradiation levels. Solar Energy, 171(July), 547-561. https://doi.org/10.1016/j.solener.2018.06.080*

[2] *Abdel, Christine, Modélisation, Nour et Nour, Christine Abdel. (2020). Modélisation d ' une installation photovoltaïque avec réflecteurs en vue de l ' intégration dans un réseau intelligent.*

[3] *Abedi, Arash, Rezaie, Behrooz, Khosravi, Alireza et Shahabi, Majid. (2020). DC-bus Voltage Control based on Direct Lyapunov Method for a Converter-based Stand-alone DC Micro-grid. Electric Power Systems Research, 187(June), 106451. https://doi.org/10.1016/j.epsr.2020.106451*

[4] *Abraham, Rijo et Ashok, S. (2020). Data-driven optimization of torque distribution function for torque ripple minimization of switched reluctance motor. 2020 International Conference for Emerging Technology, INCET 2020, 1-6. https://doi.org/10.1109/INCET49848.2020.9154044*

[5] *Ahn, Jin Woo et Lukman, Grace Firsta. (2019). Switched reluctance motor drives. Modeling, Simulation and Control of Electrical Drives, 275-374. https://doi.org/10.1201/9781420028157-23*

[6] *Aljaism, W. A. (2007). Switched reluctance motor: Design, simulation and control. researchdirect.uws.edu.au/islandora/object/uws:3650/datastream/PDF/view, 1-193.*

[7] *Alvarez, Juan Paez, Paez, Juan, Dc-dc, Alvarez, David, Juan et Alvarez, Paez. (2021). DC-DC converter for the interconnection of HVDC grids To cite this version : HAL Id : tel-03132552 Convertisseurs DC-DC pour l ' interconnexion des réseaux HVDC DC-DC converters for the interconnection of HVDC grids.*

[8] *Annet Sheen, P. M. et Shahin, M. (2021). Battery integrated SPV powered SRM Driven Water Pump. Dans Asia-Pacific Power and Energy Engineering Conference, APPEEC (vol. 2021-November). IEEE Computer Society. https://doi.org/10.1109/APPEEC50844.2021.9687803*

[9] *Aouchiche, Nedjma. (2020). Conception d ' une commande MPPT optimale à base d ' intelligence artificielle d ' un système photovoltaïque . Nedjma Aouchiche To cite this version : HAL Id : tel-02902953.*

[10] *Arif, Ali, Guettaf, Abderrazak, Megherbi, Ahmed Chaouki, Benramache, Said et Benchabane, Fateh. (2014). Electromagnetic modeling and control of switched reluctance motor using finite elements. Frontiers in Energy, 8(3), 355-363. https://doi.org/10.1007/s11708-014-0319-5*

[11] *Arif, Ali, Guettaf, Abderrazak, Sbaa, Salim et Benramache, Said. (2017). Electromagnetic characteristics correlated with the excitation current and the rotor* *position in the SRM. International Journal of System Assurance Engineering and Management, 8(s1), 180-187. https://doi.org/10.1007/s13198-015-0366-2*

[12] *Ayang, Albert. (2020). Diagnostic d'un système photovoltaïque à stockage par estimation paramétrique et commandes ADRC, intégré à une centrale autonome de cogénération d'énergie, 235.*

[13] *Bakan, A Faruk, Aksoy, İ et Altinta, Nihan. (2012). Loss Analysis of Half Bridge DC-DC Converters in High-Current and Low-Voltage Applications, 6(3), 201-205.*

[14] *Borni, A., Abdelkrim, T., Bouarroudj, N., Bouchakour, A., Zaghba, L., Lakhdari, A. et Zarour, L. (2017). Optimized MPPT Controllers Using GA for Grid Connected Photovoltaic Systems, Comparative study. Energy Procedia, 119, 278-296. https://doi.org/10.1016/j.egypro.2017.07.084*

[15] *Chakir, Mohamed, Des, Faculte et Et, Sciences. (2010). CONCEPTION ET OPTIMISATION DE LA PERFORMANCE D ' UNE GÉNÉRATRICE À Résumé.*

[16] *Chankaya, Mukul, Naqvi, Syed Bilal Qaiser, Hussain, Ikhlaq, Singh, Bhim et Ahmad, Aijaz. (2024). Power quality enhancement and improved dynamics of a grid tied PV system using equilibrium optimization control based regulation of DC bus voltage. Electric Power Systems Research, 226(October 2023), 109911. https://doi.org/10.1016/j.epsr.2023.109911*

[17] *Dankadai, N. K., Elgendy, M. A., McDonald, S. P., Atkinson, D. J. et Atkinson, G. (2019). Investigation of Reliability and Complexity of Torque Control for Switched Reluctance Drives. IEEE Conference on Power Electronics and Renewable Energy, CPERE 2019, 485-490. https://doi.org/10.1109/CPERE45374.2019.8980219*

[18] *Deng, Xu. (2017). A drive system for six-phase switched reluctance motors. http://theses.ncl.ac.uk/jspui/handle/10443/3921*

[19] *Deng, Xu et Mecrow, Barrie. (2020). A Piecewise Direct Instantaneous Energy Control Strategy for DC-link Capacitor and Torque Ripple Reduction in Multi-phase Switched Reluctance Motor Drive Systems. 23rd International Conference on Electrical Machines and Systems, ICEMS 2020, 956-960. https://doi.org/10.23919/ICEMS50442.2020.9291041*

[20] *Ecole, Paris-sud. (2018). Amélioration de la sûreté de fonctionnement d'un actionneur électrique à réluctance variable.*

[21] *Fadhel, Mme Siwar. (2019). Efficacité énergétique et surveillance d ' un microgrid à courant continu alimenté par des panneaux photovoltaïques.*

[22] *Fan, Li ping, Chen, Qi peng et Guo, Zhi qiang. (2022). An Fuzzy improved perturb and observe (P&O) maximum power point tracking (MPPT) algorithm for Microbial Fuel Cells. International Journal of Electrochemical Science, 17(11), 221157. https://doi.org/10.20964/2022.11.49*

[23] *Fang, Gaoliang, Pinarello Scalcon, Filipe, Xiao, Dianxun, Vieira, Rodrigo, Grundling, Hilton et Emadi, Ali. (2021). Advanced Control of Switched Reluctance Motors (SRMs): A Review on Current Regulation, Torque Control and Vibration Suppression. IEEE Open Journal of the Industrial Electronics Society, 2(May), 280-301. https://doi.org/10.1109/OJIES.2021.3076807*

[24] *Feng, Liyun, Sun, Xiaodong, Tian, Xiang et Diao, Kaikai. (2022). Direct Torque Control with Variable Flux for an SRM Based on Hybrid Optimization Algorithm. IEEE Transactions on Power Electronics, 37(6), 6688-6697. https://doi.org/10.1109/TPEL.2022.3145873*

[25] *Feng, Yang, Zhao, Chunfa, Bai, Zhan, Tong, Laisheng et Shu, Yao. (2023). A modified electromagnetic force calculation method has high accuracy and applicability for EMS maglev vehicle dynamics simulation. ISA Transactions, 137, 186-198. https://doi.org/10.1016/j.isatra.2023.01.019*

[26] *Ferková, Želmíra, Suchý, Ľuboš et Bober, Peter. (2020). Comparison of 6/4 and 12/8 switched reluctance motor models using direct torque control with torque lookup table. Electrical Engineering, 102(1), 75-83. https://doi.org/10.1007/s00202-019-00775-z*

[27] *Foray, Etienne. (2021). Design of an integrated high-voltage low-power isolated DC / DC converter for automotive applications To cite this version : HAL Id : tel-03405711 Design of an integrated high-voltage low-power isolated DC / DC converter for automotive applications.*

[28] *Griffin, L., Fleming, F. et Edrington, C. S. (2014). A particle swarm optimization based maximum torque per ampere control for a switched reluctance motor. IECON Proceedings (Industrial Electronics Conference), 343-348. https://doi.org/10.1109/IECON.2014.7048522*

[29] *Guettaf, Abderrazak, Chabane, Foued, Arif, Ali et Benramache, Said. (s. d.). Journal of Power Technologies 93 (3) (2013) 149-153 Dynamic Modeling in a Switched Reluctance Motor SRM using Finite Elements.*

[30] *Han, Lele, Xu, Aide, Zhu, Jingwei et Zhang, Wen. (2019). Torque Observer of SRM Based on BP Neural Network Optimized by Bat Algorithm. 2019 22nd International Conference on Electrical Machines and Systems, ICEMS 2019. https://doi.org/10.1109/ICEMS.2019.8921967*

[31] *Han, Shouyi, Diao, Kaikai et Sun, Xiaodong. (2021). Overview of multi-phase switched reluctance motor drives for electric vehicles. Advances in Mechanical Engineering, 13(9), 1-18. https://doi.org/10.1177/16878140211045195*

[32] *Hoang, Emmanuel. (1995). Étude, Modélisation Et Mesure Des Pertes Magnétiques Dans Les Moteurs À Réluctance Variable À Double Saillance. https://tel.archives-ouvertes.fr/tel-00533015/*

[33] *Hofmann, A. et De Doncker, R. W. (2014). Hysteresis-based DIFC in SRM: Eliminating switching harmonics while improving inverter efficiency. 7th IET International Conference on Power Electronics, Machines and Drives, PEMD 2014.*

[34] *Hypolite, Amèdedjihunde et Hounnou, Jordâo. (2020). Dimensionnement optimal d ' un système hybride hydroélectrique-photovoltaïque-stockage pour une alimentation rurale isolée Amèdedjihunde Hypolite Jordâo Hounnou To cite this version : HAL Id : tel-02967644 Dimensionnement optimal d ' un système hybride hy.*

[35] *Ilea, Dan. (2011). Conception optimale des moteurs à réluctance variable à commutation électronique pour la traction des véhicules électriques légers, 1-161.*

[36] *İnci, Mustafa. (2021). A flexible perturb & observe MPPT method to prevent surplus energy for grid-failure conditions of fuel cells. International Journal of Hydrogen Energy, 46(79), 39483-39498. https://doi.org/10.1016/j.ijhydene.2021.09.185*

[37] *Inthamoussou, Fernando A. et Valenciaga, Fernando. (2021). A fast and robust closed-loop photovoltaic MPPT approach based on sliding mode techniques. Sustainable Energy Technologies and Assessments, 47. https://doi.org/10.1016/j.seta.2021.101499*

[38] *Introduction, I I. (s. d.). Modélisation du système véhicule électrique, 18-42.*

[39] *Jendoubi, Abdessattar, Tlili, Faouzi et Bacha, Faouzi. (2020). Sliding mode control for a grid connected PV-system using interpolation polynomial MPPT approach. Mathematics and Computers in Simulation, 167, 202-218. https://doi.org/10.1016/j.matcom.2019.09.007*

[40] *Jieb, Yaman Abou et Hossain, Eklas. (2021). Photovoltaic Systems: Fundamentals and Applications. Photovoltaic Systems: Fundamentals and Applications. https://doi.org/10.1007/978-3-030-89780-2*

[41] *Kamran Khan, Muhammad, Hamza Zafar, Muhammad, Riaz, Talha, Mansoor, Majad et Akhtar, Naureen. (2024). Enhancing efficient solar energy harvesting: A process-in-loop investigation of MPPT control with a novel stochastic algorithm. Energy Conversion and Management: X, 21(December 2023), 100509. https://doi.org/10.1016/j.ecmx.2023.100509*

[42] *Kamran, Muhammad, Mudassar, Muhammad, Fazal, Muhammad Rayyan, Asghar, Muhammad Usman, Bilal, Muhammad et Asghar, Rohail. (2020). Implementation of improved Perturb & Observe MPPT technique with confined search space for standalone photovoltaic system. Journal of King Saud University - Engineering Sciences, 32(7), 432-441. https://doi.org/10.1016/j.jksues.2018.04.006*

[43] *Kim, Insu et Xu, Shuo. (2019). Bus voltage control and optimization strategies for power flow analyses using Petri net approach. International Journal of Electrical Power and Energy Systems, 112(August 2018), 353-361. https://doi.org/10.1016/j.ijepes.2019.05.009*

[44] *Klein-Hessling, Annegret, Hofmann, Andreas et De Doncker, Rik W. (2017). Direct instantaneous torque and force control: A control approach for switched reluctance machines. IET Electric Power Applications, 11(5), 935-943. https://doi.org/10.1049/iet-epa.2016.0515*

[45] *Kongphet, Vorachack, Migan-dubois, Anne, Delpha, Claude et Diallo, Demba. (2022). Contribution to fault detection of PV modules using I-V curves. Thesis.*

[46] *Kotb, Hossam, Yakout, Ahmed H., Attia, Mahmoud A., Turky, Rania A. et AboRas, Kareem M. (2022). Speed control and torque ripple minimization of SRM using local unimodal sampling and spotted hyena algorithms based cascaded PID controller. Ain Shams Engineering Journal, 13(4), 101719. https://doi.org/10.1016/j.asej.2022.101719*

[47] *Kumar, Vivek et Bindal, Ranjit Kumar. (2022). MPPT technique used with perturb and observe to enhance the efficiency of a photovoltaic system. Materials Today: Proceedings, 69(2022), A6-A11. https://doi.org/10.1016/j.matpr.2023.01.002*

[48] *Labak, Anas. (2010). New design of switched reluctance motor using finite element analysis for hybrid electric vehicle applications.*

[49] *Li, Wei, Cui, Zhiwei, Ding, Shichuan, Chen, Fan et Guo, Yiyang. (2022). Model Predictive Direct Torque Control of Switched Reluctance Motors for Low-Speed Operation. IEEE Transactions on Energy Conversion, 37(2), 1406-1415. https://doi.org/10.1109/TEC.2021.3131870*

[50] *Li, Yafang. (2019). A DC-DC power converter study for High Voltage Direct Current (HVDC) grid : Model and control of the DC-DC Modular Multilevel Converter (M2DC) Yafang Li To cite this version : HAL Id : tel-02384233.*

[51] *Mambrini, Thomas. (2015). Caractérisation de panneaux solaires photovoltaïques en conditions réelles d ' implantation et en fonction des différentes technologies To cite this version : HAL Id : tel-01164783 par Caractérisation de panneaux solaires photovoltaïques en conditions rée, 1-194.*

[52] *Manikandan, R., Raja Singh, R., Edison, G. et Gnanaraj, S. Darius. (2022). Hardware-in-Loop-Based Reliability Improvement of Power Converter for Critical Electrical Drive Applications. https://doi.org/10.1007/978-981-16-4388-0_14*

[53] *Mark, E. (2013). Simulating and testing a DC-DC half-bridge SLR converter NAVAL POSTGRADUATE.*

[54] *Martos, Olivier et Montpellier, D E L Université D E. (2023). Étude d ' un convertisseur DC / DC isolé de forte puissance , destiné à l ' alimentation de bord de navires civils et militaires To cite this version : HAL Id : tel-04137657 Étude d ' un convertisseur DC / DC isolé de forte puissance , destiné à l ' alime.*

[55] *Mendi, Balaji, Pattnaik, Monalisa et Srungavarapu, Gopalakrishna. (2024). A single current sensor based adaptive step size MPPT control of a small scale variable speed wind energy conversion system. Applied Energy, 357(December 2023), 122492. https://doi.org/10.1016/j.apenergy.2023.122492*

[56] *Modeling, Yassine Chaibi, System, Photovoltaic, Ahmed, A L Mars et Abdelwahed, Echchatbi. (2020). Modeling and Optimization of a Standalone Photovoltaic System supplying an alternative Load Yassine Chaibi To cite this version : HAL Id : tel-02535080 Université Moulay Ismail Ecole Nationale Supérieure d ' Arts et Métiers , Meknès Centre d ' études doct.*

[57] *Mohammadinodoushan, Mohammad, Abbassi, Rabeh, Jerbi, Houssem, Waly Ahmed, Faraedoon, Abdalqadir kh ahmed, Halkawt et Rezvani, Alireza. (2021). A new MPPT design using variable step size perturb and observe method for PV system under partially shaded conditions by modified shuffled frog leaping algorithm- SMC controller. Sustainable Energy Technologies and Assessments, 45(February), 101056. https://doi.org/10.1016/j.seta.2021.101056*

[58] *Mousa, Hossam H.H., Youssef, Abdel Raheem et Mohamed, Essam E.M. (2021). State of the art perturb and observe MPPT algorithms based wind energy conversion systems: A technology review. International Journal of Electrical Power and Energy Systems, 126(PA), 106598. https://doi.org/10.1016/j.ijepes.2020.106598*

[59] *Nagari, Angelo, Allard, Bruno et Chesneau, David. (2018). A contribution to synchronization of the sliding-mode control-based integrated step-down DC / DC converter Benoît Labbe To cite this version : HAL Id : tel-01927902 Benoˆ ıt Labbe.*

[60] *Pan, Yingjiu, Fang, Wenpeng, Ge, Zhenzhen, Li, Cheng, Wang, Caifeng et Guo, Baochang. (2024). A hybrid on-line approach for predicting the energy consumption of electric buses based on vehicle dynamics and system identification. Energy, 290(December 2023), 130205. https://doi.org/10.1016/j.energy.2023.130205*

[61] *Polanco, Erik Chumacero. (2015). Velocity sensorless control switched reluctance motors Université Paris-Sud Erik CHUMACERO-POLANCO switched reluctance motors.*

[62] *Poulek, Vladislav, Safrankova, Jana, Cerna, Ladislava, Libra, Martin, Beranek, Vaclav, Finsterle, Tomas et Hrzina, Pavel. (2021). PV Panel and PV Inverter Damages Caused by Combination of Edge Delamination, Water Penetration, and High String Voltage in Moderate Climate. IEEE Journal of Photovoltaics, 11(2), 561-565. https://doi.org/10.1109/JPHOTOV.2021.3050984*

[63] *Rahimi, Mostafa, Candeo, Stefano, Da Lio, Mauro, Biral, Francesco, Wahlström, Jens et Bortoluzzi, Daniele. (2023). A novel approach for brake emission estimation based on traffic microsimulation, vehicle system dynamics, and machine learning modeling. Atmospheric Pollution Research, 14(10). https://doi.org/10.1016/j.apr.2023.101872*

[64] *Ribeiro, Kelly et Santos, De Faria. (2021). Design of a bidirectional on-board charger and a DC-DC converter for low voltage battery in Electric Vehicles To cite this version : Design of a Bidirectional on-board charger and a DC-DC converter for Low Voltage Battery in Electric Vehicles.*

[65] *Saadi, Yakoub. (2019). Stratégies de contrôle et analyse des défauts d ’une machine à réluctance variable pour une chaîne de traction électrique, 207.*

[66] *Stitou, Mohamed. (2021). Contribution à la commande non linéaire des systèmes photovoltaïques Mohamed Stitou To cite this version : HAL Id : tel-03240084.*

[67] *Sun, Xiaodong, Feng, Liyun, Zhu, Zhen, Lei, Gang, Diao, Kaikai, Guo, Youguang et Zhu, Jianguo. (2022). Optimal Design of Terminal Sliding Mode Controller for Direct Torque Control of SRMs. IEEE Transactions on Transportation Electrification, 8(1), 1445-1453. https://doi.org/10.1109/TTE.2021.3111889*

[68] *Tian, Jiale, Chen, Gang et Luo, Longzhou. (2020). Sliding mode MPPT control based on fuzzy exponential approach rate for PV cells. Dans 2020 IEEE 4th Conference on Energy Internet and Energy System Integration: Connecting the Grids Towards a Low-Carbon High-Efficiency Energy System, EI2 2020 (p. 623-626). Institute of Electrical and Electronics Engineers Inc. https://doi.org/10.1109/EI250167.2020.9347000*

[69] *Vieira, Romênia G., de Araújo, Fábio M.U., Dhimish, Mahmoud et Guerra, Maria I.S. (2020). A comprehensive review on bypass diode application on photovoltaic modules. Energies, 13(10), 1-21. https://doi.org/10.3390/en13102472*

[70] *Wichert, Torsten. (2008). Design and construction modifications of switched reluctance machines, 161.*

[71] *Winder, Steve. (2008). Boost Converters. Power Supplies for LED Drivers, 61-98. https://doi.org/10.1016/b978-0-7506-8341-8.00006-2*

[72] *Wu, Jiangling, Sun, Xiaodong et Zhu, Jianguo. (2020). Accurate torque modeling with PSO-based recursive robust LSSVR for a segmented-rotor switched reluctance motor. CES Transactions on Electrical Machines and Systems, 4(2), 96-104. https://doi.org/10.30941/cestems.2020.00014*

[73] *Xu, Aide, Shang, Chaoyi, Chen, Jiagui, Zhu, Jingwei et Han, Lele. (2019). A New Control Method Based on DTC and MPC to Reduce Torque Ripple in SRM. IEEE Access, 7, 68584-68593. https://doi.org/10.1109/ACCESS.2019.2917317*

[74] *Xu, Zhenyao, Li, Tao, Zhang, Fengge, Zhang, Yue, Lee, Dong Hee et Ahn, Jin Woo. (2022). A Review on Segmented Switched Reluctance Motors. Energies, 15(23). https://doi.org/10.3390/en15239212*

[75] *Yang, Gang. (2015). Design of a High Efficiency High Power Density DC / DC Converter for Low Voltage Power Supply in Electric and Hybrid Vehicles Gang Yang Conception d ' un Convertisseur à Haut Rendement et Très Forte Puissance.*

[76] *Youghourta, Kassimi, Abderrazak, Guettaf et Arif, Ali. (2021). 6/4 SRM electromagnetic modeling and control by using Finite element method. 3rd International Conference on Electrical, Communication and Computer Engineering, ICECCE 2021, (June), 12-13. https://doi.org/10.1109/ICECCE52056.2021.9514120*

[77] *Youghourta, Kassimi, Ali, Arif et Abderrazak, Guettaf. (2023). Feasibility Assessment of Correlation and Artificial Neural Network in Direct Torque Control for Photovoltaic (PV) System Integration with Switched Reluctance Motor (SRM), 21(7), 151-162. https://doi.org/10.48047/nq.2023.21.7.nq23016*

[78] *Zaharia, Mihai Valentin. (2018). Contributions to the study of Switched reluctance machine for automotive integrated starter-alternator application.*

[79] *Zhang, Man. (2018). Modeling of Multiphysics Electromagnetic & Mechanical Coupling and Vibration Controls Applied to Switched Reluctance Machine.*

[80] *Zhang, Man, Bahri, Imen, Mininger, Xavier, Vlad, Cristina et Berthelot, Eric. (2019). Vibration reduction control of switched reluctance machine. IEEE Transactions on Energy Conversion, 34(3), 1380-1390. https://doi.org/10.1109/TEC.2019.2908458*

[81] *Zhang, Wenping, Wang, Yiming, Xu, Po, Li, Donghui et Liu, Baosong. (2023). DC-bus voltage balancing control for 3-level DC/DC converters in renewable generation systems. Energy Reports, 9, 210-217. https://doi.org/10.1016/j.egyr.2023.05.174*

[82] *Zhu, Yueying. (2022). The Key Technologies for Powertrain System of Intelligent Vehicles Based on Switched Reluctance Motors.*

[83] *Zhuo, Shengrong. (2022). Control of interleaved DC-DC converter with switch fault consideration for fuel cell application Shengrong Zhuo To cite this version : HAL Id : tel-03894942 Control of Interleaved DC-DC Converter with Switch Fault.*

ملخص

تقدم هذه الأطروحة دراسة شاملة حول تعزيز استراتيجيات التحكم التشغيلية لآلات الممانعة التبديلية (SRMs) من خلال نهج متعدد الأوجه. وتتمثل المساهمة الأساسية في تطوير منهجية مبتكرة تهدف إلى تخفيف تموج عزم الدوران، وهي مشكلة سائدة في تطبيقات SRM ، مع تحسين الأداء العام للماكينة في نفس الوقت .

يتضمن التركيز الثانوي لهذا العمل دمج النظام الكهروضوئي (PV) مع SRM ، مما يؤدي إلى إنشاء وحدة متماسكة ومتآزرة. تم تصميم هذا التكامل ليس فقط لتشغيل SRM ولكن أيضًا لتحسين كفاءتها التشغيلية من خلال الاستفادة من الطاقة الشمسية، وبالتالي المساهمة في حل أكثر استدامة وكفاءة في استخدام الطاقة .

بالإضافة إلى تحسين المكونات الفردية، يستكشف البحث تطبيق نظام محرك الممانعة الكهروضوئية (PV-SRM) في المركبات الكهربائية (EVs). ويمثل هذا مبادرة رائدة لدمج مصادر الطاقة المستدامة في النقل الكهربائي، ودفع المجال نحو حلول أكثر خضرة .

علاوة على ذلك، تتضمن الأطروحة تقييمًا تجريبيًا لخوارزمية التحكم في التباطؤ على SRM8/6 ، مما يوفر دليلًا تجريبيًا على فوائد أدائها. توضح النتائج فعالية الخوارزمية في تعزيز دقة التحكم والكفاءة التشغيلية لـ SRM.

بشكل عام، تقدم هذه الأطروحة تطورات كبيرة في منهجيات التحكم في SRM، والتكامل الكهروضوئي، والتطبيق العملي لأنظمة PV-SRM في المركبات الكهربائية، مما يؤكد إمكانية الابتكارات المستدامة في أنظمة الدفع الكهربائي.

Résume

Cette thèse présente une étude complète sur l'amélioration des stratégies de contrôle opérationnel pour les machines à réluctance commutée (SRM) grâce à une approche multidimensionnelle. La principale contribution est le développement d'une méthodologie innovante visant à atténuer l'ondulation du couple, un problème répandu dans les applications SRM, tout en optimisant simultanément les performances globales de la machine.

Un objectif secondaire de ce travail implique l'intégration d'un système photovoltaïque (PV) avec le SRM, créant ainsi une unité cohérente et synergique. Cette intégration est conçue non seulement pour alimenter le SRM, mais également pour améliorer son efficacité opérationnelle en tirant parti de l'énergie solaire, contribuant ainsi à une solution plus durable et plus économe en énergie.

En plus d'optimiser les composants individuels, la recherche explore l'application du système de moteur à réluctance à commutation photovoltaïque (PV-SRM) dans les véhicules électriques (VE). Il s'agit d'une initiative pionnière visant à intégrer des sources d'énergie durables dans le transport électrique, faisant ainsi progresser le domaine vers des solutions plus vertes.

De plus, la thèse comprend une évaluation expérimentale de l'algorithme de contrôle de l'hystérésis sur un SRM 6/8, fournissant des preuves empiriques de ses avantages en termes de performances. Les résultats démontrent l'efficacité de l'algorithme pour améliorer la précision du contrôle et l'efficacité opérationnelle du SRM.

Dans l'ensemble, cette thèse offre des avancées significatives dans les méthodologies de contrôle SRM, l'intégration photovoltaïque et l'application pratique des systèmes PV-SRM dans

les véhicules électriques, soulignant le potentiel d'innovations durables dans les systèmes de propulsion électrique.

Abstract

This thesis presents a comprehensive study on enhancing operational control strategies for Switched Reluctance Machines (SRMs) through a multi-faceted approach. The primary contribution is the development of an innovative methodology aimed at mitigating torque ripple, a prevalent issue in SRM applications, while simultaneously optimizing overall machine performance.

A secondary focus of this work involves the integration of a photovoltaic (PV) system with the SRM, creating a cohesive and synergistic unit. This integration is designed to not only power the SRM but also to improve its operational efficiency by leveraging solar energy, thereby contributing to a more sustainable and energy-efficient solution.

In addition to optimizing individual components, the research explores the application of the Photovoltaic-Switched Reluctance Motor (PV-SRM) system in Electric Vehicles (EVs). This represents a pioneering initiative to incorporate sustainable energy sources into electric transportation, advancing the field towards greener solutions.

Furthermore, the thesis includes an experimental evaluation of the hysteresis control algorithm on a 6/8 SRM, providing empirical evidence of its performance benefits. The findings demonstrate the algorithm's efficacy in enhancing the control precision and operational efficiency of the SRM.

Overall, this thesis offers significant advancements in SRM control methodologies, PV integration, and the practical application of PV-SRM systems in EVs, underscoring the potential for sustainable innovations in electric propulsion systems.